RÉPUBLIQUE FRANÇAISE
Liberté Égalité Fraternité

Université de Toulouse

Doctorat de l'Université de Toulouse

préparé à l'ISAE-SUPAERO

Navigation autonome par Imagerie Radar Cohérente

Thèse présentée et soutenue, le 28 mai 2026 par

Titouan TYACK

École doctorale
EDMITT - Ecole Doctorale Mathématiques, Informatique et Télécommunications de Toulouse

Spécialité
Mathématiques et Applications

Unité de recherche
ISAE-ONERA SCANR Signal communication Antennes Navigation Radar

Thèse dirigée par
Damien VIVET et Laurent FERRO-FAMIL

Composition du jury
Mme Atika RIVENQ, Présidente, Université Polytechnique Hauts-de-France
M. Stéphane MÉRIC, Rapporteur, INSA Rennes
M. Roland LENAIN, Rapporteur, INRAE Clermont - Auvergne-Rhône-Alpes
M. Damien VIVET, Directeur de thèse, ISAE-SUPAERO
M. Laurent FERRO-FAMIL, Co-directeur de thèse, ISAE-SUPAERO

Membres invités
M. Frédéric MONGE, DGA Maîtrise de l'information

Acknowledgments

Je tiens à remercier l'ensemble des personnes qui m'ont accompagné en amont et tout au long de cette thèse. Merci à ma famille qui a grandement contribué à construire un environnement favorisant la curiosité, le doute, la sérénité, l'épanouissement par le travail et ses retombées et autres ingrédients particulièrement propices à la poursuite de longues études. Pour tout cela, un grand merci à mes parents, mon frère et ma sœur, mes grands-parents, oncles et tantes, cousins et cousines. À Asnate, merci, ou plutôt devrais-je dire paldies, pour tout. Nous avons commencé en même temps nos thèses mais avec des conditions de départ bien différentes et je serai éternellement admiratif de ton parcours.

Un très grand merci à mes directeurs de thèse Damien VIVET et Laurent FERRO-FAMIL qui, d'abord, m'ont proposé de faire cette thèse au carrefour de deux communautés, puis m'ont accompagné avec bienveillance et sérieux. Merci d'avoir su parfaitement doser entre liberté et orientation.

Merci à toutes les personnes qui facilitent grandement la vie des doctorants du DEOS, dans mon cas, je pense à Gilles, Myriam, Frédérique et Maryse. Merci aux précieux ingénieurs Louis et Benoît sans qui j'aurais eu beaucoup plus de mal à faire mes nombreuses expérimentations avec le robot. Merci à Paul Checchin et Thomas Oberlin, qui ont formé mon comité de suivi individuel et m'ont suivi et encouragé tout au long de cette thèse. Un grand merci à Caroline, Corentin, Charles, Christophe, Baptiste et Matthieu qui m'ont introduit au monde de la robotique mobile et de la recherche dans une atmosphère de travail chaleureuse.

Merci à tous mes amis qui m'ont accompagné durant ces années: Justin, Nathan, Paul, Victor, Augustin, Gwendo, Sofiane, Ines, Elio.

Un grand merci à tous les doctorants et stagiaires que j'ai pu rencontrer durant ces années, sans qui l'ambiance au DEOS aurait été bien différente : Aubin, Alex, Antoine, Louise, Martin, Pierre, Valentin, Younes, Javier, Thomas, Nadia, Sarah, Joanna, Gaston, Thibault. Plus particulièrement ceux de l'équipe NAVIRRES: Yi, Justin, Mengda, Ruizheng, Suchetan, Allen, Léa, Esteban, Anaïs, Filipo, Shreyank avec une mention spéciale pour César, Maximilian et Florent mes work-wifes.

Enfin, j'ai une pensée émue pour ma grand-mère, Luc et Gérard, qui nous ont quittés pendant ces années et avec qui j'aurais grandement aimé partager cet accomplissement.

Merci à toutes et tous.

Contents

List of Figures **ix**

List of Tables **xi**

1 Introduction **1**
1.1 Autonomous Mobile Robotics: Context . . . 1
1.2 Motivations of Radar Mapping and Localisation . . . 2
1.3 Thesis Contributions and Outlines . . . 3

2 Radar principles and operations **5**
2.1 History . . . 5
2.2 Radar in robotics . . . 6
2.3 Comparison with traditional exteroceptive sensors in robotics . . . 8
2.4 Radar Operations . . . 10
2.5 Radar Signal Processing . . . 14
2.5.1 Range Measurement . . . 15
2.5.2 Radial Velocity Measurement . . . 16
2.5.3 Angle of Arrival Measurement . . . 17
2.6 Radar In Practice . . . 20
2.6.1 Constant False Alarm Rate Detector . . . 20
2.6.2 Point Cloud Generation . . . 21
2.7 Conclusion And Discussion . . . 22

3 Radar Localisation **25**
3.1 State Of The Art . . . 26
3.1.1 State Of The Art on Point Cloud based Radar Localisation . . . 26
3.1.2 State Of The Art on Raw Data based Radar Localisation . . . 28
3.1.3 Discussion . . . 29
3.2 Single-scan state estimation . . . 29
3.2.1 Ego-Velocity Measurement Model . . . 30
3.2.2 Tightly-Coupled 2D Odometry . . . 31
3.2.3 Validation on Simulation . . . 32
3.2.4 Radar Calibration . . . 33
3.2.5 Validation of Calibration and Odometry on Real Data . . . 40
3.2.6 Conclusion . . . 41
3.3 Scan-to-Scan estimation . . . 43
3.3.1 Scan Formation . . . 43
3.3.2 Results with Real data . . . 47
3.4 Conclusion And Perspectives . . . 48

4 Radar Mapping **51**
4.1 Map representations . . . 51
4.1.1 Sparse Landmark Map . . . 52
4.1.2 Grid Map . . . 53
4.2 Synthetic Aperture Radar . . . 55
4.2.1 Motivations And Principle . . . 55
4.2.2 Geometry . . . 58
4.2.3 State Of The Art . . . 60
4.2.4 Time Domain Back Projection . . . 64
4.2.5 Performing SAR Imagery . . . 65
4.3 Validation Steps . . . 71
4.3.1 Rectilinear Trajectory . . . 71
4.3.2 Non-Linear Trajectory . . . 72
4.3.3 Processed Angular Aperture . . . 76
4.3.4 SAR Vs Lidar . . . 79
4.4 Conclusion . . . 81

5 Tracker **87**
5.1 Radar ambiguity . . . 87
5.2 State of the Art . . . 89
5.3 Tracking approach . . . 90
5.4 Validation of the Multi-Object Tracker . . . 92
5.4.1 Validation via Simulation . . . 93
5.4.2 Validation via Experiments . . . 94
5.5 Conclusion And Perspectives . . . 96

6 Conclusion And Perspectives **99**
6.1 Conclusion . . . 99
6.2 Perspectives . . . 100

A Radar Processing Details **103**
A.1 Compensation of Phase Errors in TDM MIMO Radar . . . 103
A.2 Data Acquisition . . . 104

B Radar Platforms **109**

C Open Source Code **111**

Bibliography **113**

List of Figures

1.1 AMRs in the industry and services: a) Automated mining control center. b) Military autonomous surface vehicle c) Street cleaning robot 1
1.2 See-think-act cycle diagram from [Siegwart 2004] 2

2.1 (a) Hülsmeyer and his Telemobiloskop. (b) In white : Chain Home array coverage 6
2.2 (a) Pluton system, first radar to detect Mercury (1962). (b) PAVE PAWS radar, first solid-state antenna array (1980) 7
2.3 Radars (a) Denso, (b) K2PI (Cemagref), (c) NavTech and (d) Texas Instruments 7
2.4 Attenuation due to air (black), rain (blue) and fog(red) at various frequencies. In purple, common FMCW carrier frequencies used in automotive and robotics. In green and orange, lidar and camera frequency domains respectively. Adapted from [Brooker 2001] 9
2.5 FMCW Radar Synopsis. Blue and red parts denote Low Frequency and RF elements respectively 10
2.6 (a) FMCW chirp signal (b) Real part of the temporal baseband ramp signal 12
2.7 Contributions from several scatterers in RF and IF domains Adapted from [Iovescu 2017] 12
2.8 Sequence of emitted signals and impact on the phase of the received signal considering a moving scatterer 13
2.9 Difference of distance travelled by the backscattered signal to two receiving elements resulting in an inter-antenna phase difference . . . 14
2.10 Radar Data Cube formation and processing associated to each dimensions. Adapted from [Richards 2010b] 14
2.11 Range profile or backscattered signal spectrogram taken from a moving radar looking at a static scene 16
2.12 Range Doppler Map from a front facing moving radar, all the scatterers in its field of view are approaching the sensor 17
2.13 Multiple-Input Multiple-Output antenna array 19
2.14 Real and Virtual arrays of elements for two different radars, AWR1843 and TinyRad. In red, blue and green are respectively emitters, receivers and virtual antennas. On the left, since an emitter is shifted vertically, the virtual array fills two vertical position. On the right, the array is linear and we can notice that the pair Tx0-Rx3 and Tx1-Rx0 give virtual elements located at the same position. 20
2.15 1D CFAR principle 21
2.16 Pointcloud formation via a 3D DFT and one CFAR 22
2.17 Pointcloud formation via successive DFTs and CFARs 22

3.1 Frame convention - in black robot frame, in red sensor frame 30
3.2 Matlab Driving Scenario simulator. Left: environment definition. Right: Simulated radar measurements 33
3.3 EKF estimation and ground truth - Single radar case 33
3.4 EKF estimation and ground truth - Multi-radar case 33
3.5 Position estimation of two radars - 100 runs 36
3.6 Mounting poses indexing 37
3.7 Values of $|\mathcal{I}|$ are depicted on y-axis of plot (a) and with color on others. x-axis represents poses of sensor 1 (S_1). On plots (b),(c) and (d) poses of sensor 2 (S_2) are on y-axis. Plots (a) and (b) corresponds to velocity estimation for mono- and multi-radar. Plots (c) and (d) represents respectively the observability of orientation and lever-arm estimation 38
3.8 Minimums of observability by element-wise multiplication 39
3.9 Optimal sensor placements poses pair 39
3.10 Instrumented rover used for single-scan odometry 40
3.11 Estimated extrinsic angles 41
3.12 Estimated extrinsic positions 41
3.13 Results of the IEKF based single-scan odometry obtained with 2 radars 42
3.14 RA map a) in polar coordinates and b) transformed in Cartesian coordinates 44
3.15 Two consecutive RA map and correspondences pairs between detected features 46
3.16 a) Estimated trajectory from range-azimuth scan-matching and DAR. b) Histograms of number of associated features to a landmark using KLT feature tracking (left) and feature matching (right) 48
3.17 a) Estimated trajectory from KISS-ICP and DAR b) Pointcloud based kept trajectory estimation solution 48

4.1 Mapping strategies: a) Landmark based, b) Grid based 52
4.2 Sparse mapping from concatenated pointcloud, color denotes height. Using our radar, a) Top-Down view and b) Superimposition on satellite optical image. c) Pointcloud map using high-resolution radar (48 Vx) [Zhang 2024] 54
4.3 Array synthesis from front-looking and side-looking radars 55
4.4 RAR vs SAR angular resolution depending on the viewing angle (relatively to direction of motion) for a a) front-looking radar b) side-looking radar 56
4.5 Range focused signal spread over an aperture 56

4.6 Sketch of side-looking wide beam-width mono-antenna RAR and SAR imaging principles. Along the trajectory, the radar-scatterer measured range (dots) is projected perpendicularly to the direction of motion. RAR: Solid lines represent the evolution of projected range. SAR: Measured range is spread over an aperture creating arcs. Summation of those arcs leads to an intensity grid map 57
4.7 Resulting SAR image. Scatterer's position has been interpolated as if it was measured by an antenna located between T_0 and T_1. Hatched part of the drawing correspond to overlapping FOV 57
4.8 Geometry of Synthetic Aperture Radar imagery 58
4.9 Equivalent aperture of SAR imagery depending on the trajectory and orientation of the radar: circular trajectory and $\pm 90°$ radar orientation case. The blue aperture result from a radar looking at a scatterer on the outer side of the circular radar's trajectory. The red aperture is from a scatterer located in the inner side. The greater the angular diversity from which a scatterer is observed, the larger the aperture from an equivalent radar following a rectilinear trajectory 60
4.10 At the center, Miranda-300 SAR imaging, on the bottom left, optical image of the scene [Stanko 2016] 61
4.11 Instrumented platforms of a) Ulm University, equipped with a radar network of 6 triggered sensors, and b) Politecnico di Milano with several IMUs, GNSS sensors and a wheel encoder 62
4.12 Pipeline of the SAR processor class. Each color depicts a thread fashion. Yellow and red boxes are running independently from the blue one. Yellow operations are done sequentially (mono-threaded) while the TDBP is multi-threaded. Blue part is called by the SLAM when a radar frame is sent to the SAR Processor. The interface between the SAR processor are done via the shared data queue (input) and displayable SAR map (output) 66
4.13 Extraction of the local grid map (blue) from the global grid map (white). In yellow are the pixels of the global map that have been seen in the past. In green, the past trajectory of the side looking radar (with a past sensor frame). In purple, the trajectory of the sensor during the sub-aperture used to synthesise the local SAR image 67
4.14 Backscatter signal spectrograms a) before and b) after leakage removal 68
4.15 TX-RX leakage path compared to useful sent and received signal . . 69
4.16 Rasterization of the SAR aperture on the local image. The pixels currently seen are in red and in orange the ones that are seen within the same sub-aperture 70
4.17 Amplitude in dB of Raw Global SAR image and its projection on optical satellite image using Google Earth 71
4.18 GT velocity compared to estimated velocity using a LSQ approach with or without RANSAC outlier rejection 72

4.19 Normalized backscatter in dB (log-amplitude) of SAR images using a side-looking 24 GHz sensor relying on a) GT positioning and b) integrated estimated velocity 73
4.20 SAR image superimposed on an optical satellite image of the measured scene 73
4.21 Normalized backscatter in dB (log-amplitude) of : a) SAR image from a non-straight trajectory using a 24 GHz radar b) SAR image after opening morphological operation and cutting at 0 dB 74
4.22 Point diffuser imaging and associated object 74
4.23 24 GHz SAR image synthesised from behind the bushes 75
4.24 Normalized backscatter in dB (log-amplitude) of : a) SAR image from a non-straight trajectory using a 77 GHz radar b) SAR image after opening morphological operation and cutting at 0 dB 76
4.25 Normalized backscatter in dB (log-amplitude) super-imposed on optical satellite image from Google Earth with a) 24 GHz and b) 77 GHz sensors' SAR images after opening morphological operation and cutting at 0 dB 77
4.26 Link between scatterers in SAR image and associated objects in image from embedded fish-eye camera. Dotted rectangles are related to approximation of viewed scenes from each images. Digits and rectangles are related to cars. Green circles are related to point scatterers such as poles and pillars. Dotted magenta lines are related to sidewalks 78
4.27 Amplitude in dB of SAR image using a) estimated and b) GT trajectory using a 77 GHz sensor. c) Orange : estimated trajectory after Umeyama alignment on GT (blue) 79
4.28 SAR images with $\theta_{a,proc} =$ a) $5°$, b) $10°$ and c) $20°$ 83
4.29 SAR image ($\theta_{a,proc} = 2.5°$) super-imposed at a fixed altitude on Google Earth 3D map 84
4.30 Accumulated pointcloud of the imaged scene and computed normals from points falling in radar FOV. Red square correspond to neighbourhood of the used radar FOV 84
4.31 Lidar product corresponding to Orientation Amplitude Grid Map. Color corresponds to mean value of dot product between radar orientation and oriented surfaces 85
4.32 SAR and Lidar image in Field scenario $N°1$. a) SAR image b) Normalized Lidar product. c) Used rover with mounted sensors 85
4.33 SAR and Lidar image in Field scenario $N°2$. a) SAR image b) Normalized Lidar product 86
4.34 a) Superposition of Lidar product on optical satellite image for context. b) Picture from the field, in the middle, the traversed path. . . 86

5.1 Radar measurement and its actual state in a classic scenario 88
5.2 CA-CFAR on replicated range-Doppler maps 92
5.3 Detection results. Input is the upper left map 92

5.4 Simulated scenario with the ground-truth and estimated trajectories 93
5.5 Tracked targets - 2 Agilex Scout from ONERA/DTIS Toulouse . . . 94
5.6 Range ambiguity resolution 95
5.7 Azimuth ambiguity resolution 95
5.8 Estimated 2D and 3D trajectories of tracks having at least exceeded a probability of existence of 0.90. Red tracks in the XY plane are the ground truth. Other tracks match their colors with the one in Fig. 5.9. 95
5.9 Probability of existence of each track at each iteration. Tracks that are not crossing a probability level of 0.5 are generally due to false detections. Only two tracks, the ones corresponding to the rovers, maintain a high level of probability of existence. 96

A.1 TDM MIMO emitting scheme with 3 Tx 104
A.2 Raw Data Cube a) with and b) without interlaced zero-padding in chirp dimension for TDM motion compensation . The colours denotes the signals associated to different sub-arrays 105
A.3 Polar and Cartesian Range Azimuth Maps without (left) and with (right) TDM phase errors compensation. The green dots on the Cartesian maps are CFAR detections from phases compensated signal. Boxes are showing some salient features in the radar FOV like metallic stairs and pole 105
A.4 Real and Complex Radar Acquisition Architecture 106
A.5 Signal spectrums associated to real and complex acquisition architecture 107

B.1 Radar used during this thesis 109

C.1 Github repository of the library. 111

List of Tables

2.1 Comparison of common exteroceptive sensors in robotics 8
2.2 CFAR detectors performances and computational time 21

4.1 SAR related cited algorithm comparison 63

B.1 Specifications of radar platforms used in this thesis 110

Chapter 1

Introduction

Contents

1.1 Autonomous Mobile Robotics: Context 1
1.2 Motivations of Radar Mapping and Localisation 2
1.3 Thesis Contributions and Outlines 3

1.1 Autonomous Mobile Robotics: Context

Autonomous Mobile Robots (AMRs) are becoming widely used in a variety of industries, including mining, the military, logistics, healthcare, and agriculture (see Figures 1.1a and 1.1b), as well as in service applications, such as delivery, cleaning, and transportation (see Figure 1.1c).



(a) (b) (c)

Figure 1.1: AMRs in the industry and services: a) Automated mining control center. b) Military autonomous surface vehicle c) Street cleaning robot

Autonomous mobile robotics encompasses any artificial object equipped with perception capabilities that enable it to model its environment, localize itself within it, and then move around and interact with it, based on cognitive planning intended to fulfil mission commands. This rule is abbreviated to the "see-think-act" cycle illustrated in Figure 1.2 detailing the role of the main concepts associated to this discipline. This thesis focuses on the perception and localization aspects of the field especially in the context of outdoor, global positioning denied, and unknown environment. AMRs tend to be used in increasingly diverse scenarios requiring not only a robust, redundant and precise localisation but also an accurate modelling of its environment. To address these aspects, it is important to rely on several different sensors providing fail-safe and diversity of information. In this context, the radar

is a key component of a redundant sensor suite that allows increased perception capabilities to a robot.

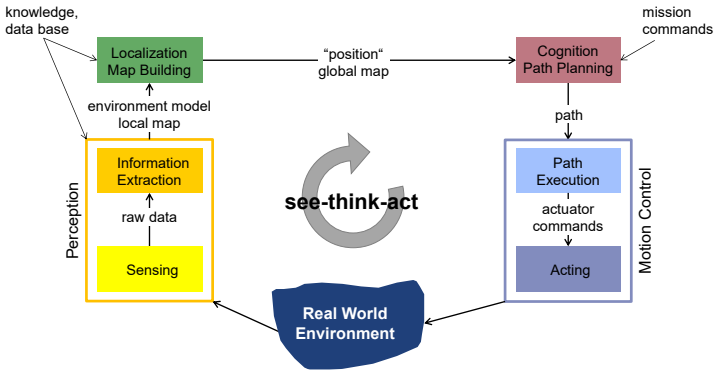

Figure 1.2: See-think-act cycle diagram from [Siegwart 2004]

1.2 Motivations of Radar Mapping and Localisation

Reliable and accurate state estimation is a mandatory requirement for any autonomous robot. The most traditional sensors such as Global Navigation Satellite System (GNSS) receivers, Inertial Measurement Unit (IMU), LiDAR or cameras are commonly used individually or combined to overcome their respective weaknesses. For instance, GNSS can be affected under challenging navigation context such as urban canyons or under the canopy due to multi-path errors or important number of non-line of sight satellites [Feriol 2020, von Arnim 2025]. Even if visual- and lidar-inertial-odometry solutions have shown excellent performances [Geneva 2020, Campos 2021, Debeunne 2024, Shan 2020, Vizzo 2023] they still admit strong limitations. Cameras are very sensitive to poor and changing lighting conditions and both cameras and LiDARs are impacted by harsh weather conditions, such as heavy rain, snow or fog and also smoke. To avoid such inconvenience the use of millimeter wave radar sensors is becoming more and more significant. Indeed, radar perception is almost insensitive to the aforementioned conditions. Moreover, this sensor admits one of the widest diversity of information since it can not only estimate objects' 3D position via range and angle measurement but also its relative radial velocity and reflectivity. For these reasons, radar-based odometry (RO) and mapping are more and more studied [Zhou 2022].

Radar in robotics has been first studied using rotating radars [Brooker 2001, Dissanayake 2001], we choose to focus on single-chip Multiple-Input Multiple-Output (MIMO) radar sensors. Beyond their cost-effectiveness, size, and weight, such sensors offer a critical advantage when processing raw data: phase coherence over time, which enables a wider range of signal processing techniques. Indeed, we will see that one of the main issue of such sensors for navigation is the poor quality of the spatial information that generates sparse, low resolution and noisy mapping.

To leverage this issue, we intend to use Synthetic Aperture Radar (SAR) techniques to get dense and well resolved cartography of the environment by the synthesis of a long array of virtual antennas along the robot trajectory.

We will see that it is mainly within the radar community that raw data based processing, especially for mapping via SAR, is performed while the robotics community tend to focus mainly on localisation aspects by using pre-processed point-cloud given at the output of most modern automotive radars. Nevertheless, both communities tend to borrow methods from each other (e.g. the recent use of Simultaneous Localisation And Mapping, SLAM, within the radar community). On the one hand, radar point clouds have the advantage of being easy to use, admit straightforward visualisation and allow for low computational cost localisation, particularly with Doppler-based velocimetry. On the other hand, the information is sparse and difficult to accurately associate from scan to scan because it is noisy, not highly repeatable in the case of large objects (walls, roads) and with an accuracy depending on the SNR and the angle of arrival. Raw data allows for denser Field Of View (FOV) mapping making the scan-to-scan estimation easier via feature matching using descriptors or via correlation. Also, via multi-scan coherent processing, it is possible to finely estimate trajectory errors. Unfortunately, these processing methods are less straightforward and more costly in terms of computation. These observations led to the motivation, since the sensor allows it, to use both types of data simultaneously. The scope of the thesis is to study the contribution of coherent radar in exteroceptive sensors based navigation. In particular, SAR imaging mapping is of interest for enabling dense, high-resolution mapping. To balance the computational load, we propose to use pre-processed point clouds for odometry. A calibration solution is presented since we use a multi-radar setup with front- and side-looking sensors. We will detail the constraints associated with the use of radar in real and synthetic aperture modes for localisation and mapping, respectively.

1.3 Thesis Contributions and Outlines

This manuscript is divided into four chapters.

- **Chapter 2 Radar Principles and Operations**, will present the radar and the basic processing tools on which this thesis is built.
- **Chapter 3 Radar Localisation**, will focus on radar-based state estimation. It includes studies carried out on radar calibration and radar odometry.
- **Chapter 4 Radar Mapping**, will present an extension to cartography, especially with SAR based mapping in the context of ground based robotics.
- **Chapter 5 Radar Tracking**, covers the proposed radar-based multi-object tracker considering measurement ambiguities.

This thesis was funded by the Defence Innovation Agency (AID) on behalf of the French Ministry of Defence, as part of the CORIBAN project under grant number 2022 65 0082.

Chapter 2

Radar principles and operations

Contents

2.1 History **5**
2.2 Radar in robotics **6**
2.3 Comparison with traditional exteroceptive sensors in robotics **8**
2.4 Radar Operations **10**
2.5 Radar Signal Processing **14**
2.5.1 Range Measurement 15
2.5.2 Radial Velocity Measurement 16
2.5.3 Angle of Arrival Measurement 17
2.6 Radar In Practice **20**
2.6.1 Constant False Alarm Rate Detector 20
2.6.2 Point Cloud Generation 21
2.7 Conclusion And Discussion **22**

2.1 History

RAdio Detection And Ranging (Radar) is a system operating by transmitting and receiving radio-frequency (RF) waves to detect and measure the reflectivity, position and relative velocity of objects in its field of view. The origins of this system lie in Heinrich Hertz's 1886 proof of the existence of electromagnetic waves based on Maxwell's equations, inspiring the first experiments in remote sensing.

The history of radar began in the early 20th century, with the aim of improving maritime safety by detecting potential obstacles in conditions of low visibility, such as fog. Christian Hülsmeyer is often credited with the 1904 invention of the "Telemobiloskop" (see figure 2.1a), capable of detecting the presence of ships, but without providing an accurate distance measurement. It was in the 1930s that significant advances were made simultaneously in Europe, the USA, the Soviet Union and Japan. In France, it was thanks in particular to Henri Gutton and Maurice Ponte, whose work resulted in the first patent for an HF radio detection device. Their system was designed to detect ships and icebergs. In the UK in 1937, motivated by the effectiveness of Zeppelin bombers during the First World War, the first antenna array for distance detection and measurement was created under the

code name *Chain Home* (see figure 2.1b). Placed on the British coast and with a range of 190km, it was widely used and played a key role in the Second World War.



(a) (b)

Figure 2.1: (a) Hülsmeyer and his Telemobiloskop.
(b) In white : Chain Home array coverage

During this period, the development of radar systems intensified, not only for aircraft and ship detection, but also for on-board radio-navigation. At the same time, jamming systems developed, giving rise to what came to be known as the battle of the beams. It was mainly after the war that the use of radar diversified into other fields, such as astronomy, thanks to advances in phased-array technology (see figure 2.2a), and Earth imaging, with the invention of synthetic aperture radar in the early 1950s. Progress continued to be driven by the Cold War, which together with advances in computer technology led to increasingly populated phased arrays capable of both very long range detection and high positioning accuracy (cf. figure 2.2b). Radar is also used in the aerospace industry, for example, for rendezvous and docking phases of US (Gemini, LEM) and Soviet (Soyuz, Progress, Mir) vehicles, right up to the ISS [Rozas 1972, Goodman 2011]. Since the late 1980s, it has been possible to have radar systems that, taking advantage of the miniaturization of electronics, correspond to on-board systems incorporating both analog functions (oscillator, antennas, mixer, etc.) and digital functions (signal processor, FPGA), opening up new fields of application for this sensor.

2.2 Radar in robotics

Radar first appeared in robotics-like applications in the early 1990s, notably in mining, port, coastal and agricultural applications [Adams 2012]. This coincided with its arrival in the automotive sector, for Advanced Driving Assistance Systems (ADAS) such as lane tracking, collision avoidance and automatic distance control.

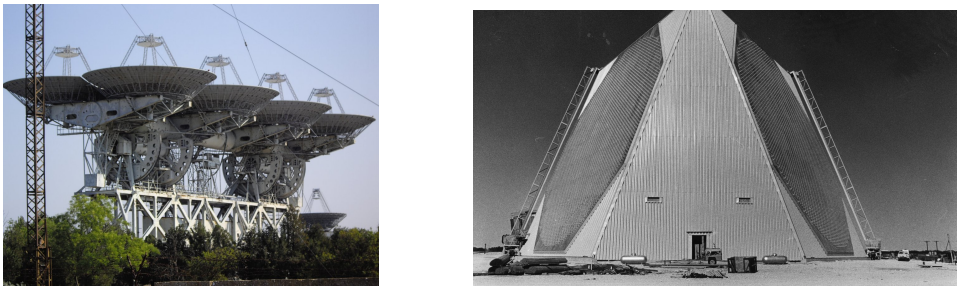

(a) (b)

Figure 2.2: (a) Pluton system, first radar to detect Mercury (1962).
(b) PAVE PAWS radar, first solid-state antenna array (1980)

In the 1990s and 2000s, although the automotive industry presented work using fixed antenna arrays (Fig. 2.3a), research applications were dominated by rotary radar (Fig. 2.3b). With systems such as those marketed by NavTech (Fig. 2.3c), the robotics community has been able to share and experiment with common grounds. The same effect has occurred since the mid-2010s, with the widespread introduction of automotive radars with integrated processing (Fig. 2.3d). These systems, incorporating antennas, oscillator, converter and digital processor, can directly provide point clouds corresponding to detected objects, making this type of sensor easier to use. Although this sensor remains less exploited than cameras and lidar within the robotics community, by harmonizing the type of data used, radar in robotics has gained in popularity over the last decade. Today, the performance and algorithms used meet the standards of other types of traditional exteroceptive sensors. Ongoing improvements in hardware, particularly in terms of angle-of-arrival estimation, suggest that the trend towards robotic radar is likely to continue.



(a) (b) (c) (d)

Figure 2.3: Radars (a) Denso, (b) K2PI (Cemagref), (c) NavTech and (d) Texas Instruments

2.3 Comparison with traditional exteroceptive sensors in robotics

In this section, since radar is not a sensor as conventional as lidar and cameras, we propose a general comparison with other common exteroceptive sensors. The table 2.1, compiles average capabilities of robotics devices and compares it in several categories. First, we will detail the non obvious categories. A high **Range** value stands for one to five hundreds meters while low correspond to the zero to five meters near field. The **Sparsity** represents how the field of view of the sensor is sampled. Dense mean that is it continuously representable while a sparse mapping admit empty spaces within the Field Of View (FOV). **Semantic information** knowledge is the machine coding of human concepts, such as the type of an item or a room [Liu 2019]. In a robotic context, we will basically say that the level of semantic information that sensor data admit follows the easiness of classification of human concepts (a pedestrian, a car, an object). **Robustness** to fog, rain, darkness and illumination variation are global tendencies, meaning does this sensor will be able to perform common tasks, like object detection or mapping, as desired or not.

Sensor	Data Type	Range	Resolution/ Accuracy	Sparsity	Semantic Information	Inform- -ation	Robustness to Fog/Rain/ Darkness/ Light Variation
Monocular Camera	2D Image (RGB/BW)	N/A	1-2 Mpx	Dense	High	Angle	Low/Low/ Low/Low
RGBD Camera	Depth Map	Low	0.9 Mpx Range:1-20mm	High	High	Range Angle	Low/Low/ Mid/Mid(1)
Lidar	3D PCL	High	0.1 cm, 5M points	Dense	Mid	Range Angle	Low/Low/ High/High
Rotating Radar	2D 360° Polar Range Map	High	17cm, Az:1°	Dense	Low	Range Angle Doppler	High/Mid(2) / High/High
MIMO Radar	3D PCL ADC Data	High High	Range 0.1m,(3) Az:1-10°,El:5-20°	Sparse Dense(4)	Low Low-Mid(4)	Range Angle Velocity	High/Mid(2) / High/High

Table 2.1: Comparison of common exteroceptive sensors in robotics

(1) RGBD camera robustness to Darkness and Illumination variation depends on the technology used, i.e. passive or active, using IR or visible light.
(2) As shown in figure 2.4, the radar robustness to rain depends both on the carrier frequency and on rain rate. For a drizzle, both 24 Ghz and 77 GHz radars are less prone to fail than other sensors, but with strong rains it is mainly the 24 GHz which will perform better than other sensors.
(3) Has seen before, MIMO radars admit many parameters which will have a strong influence on the resulting accuracies and resolutions (bandwidth, sampling frequency, PRF, number of antennas,...).
(4) Using ADC Data allows to perform many different processing. Using beamformers or SAR we can perform dense mapping in comparison to pointcloud based sparse mapping. Also, micro-Doppler and SAR can be used as a source of semantic information.

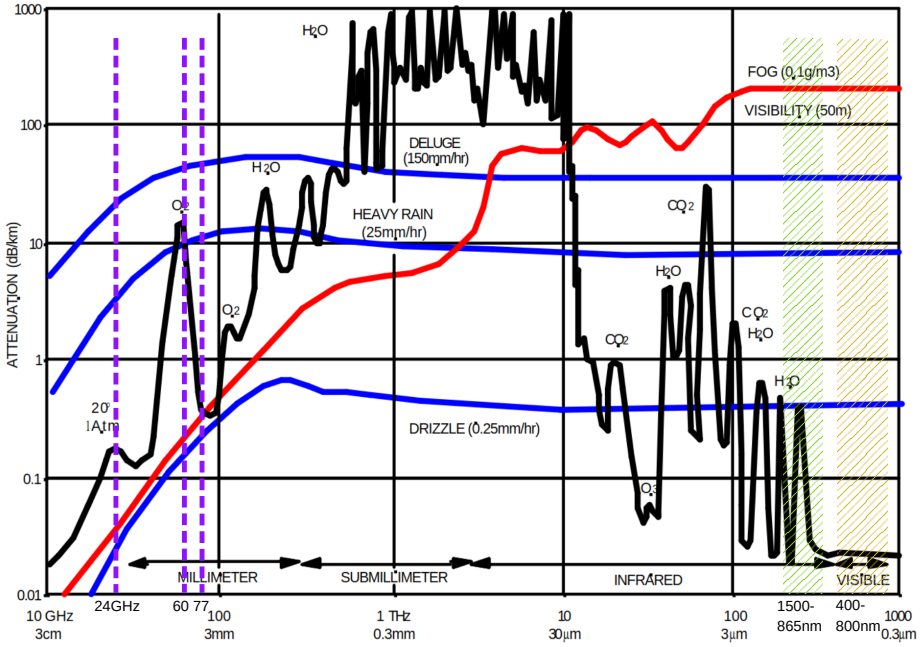

Figure 2.4: Attenuation due to air (black), rain (blue) and fog(red) at various frequencies. In purple, common FMCW carrier frequencies used in automotive and robotics. In green and orange, lidar and camera frequency domains respectively. Adapted from [Brooker 2001]

We could have added that radars can see fully or partially through some thin low reflectivity materials (leafs, thin drywalls). Also, robustness to fog, generally encompasses resilience to smoke dust and pollen etc. [Brooker 2001]. Finally, to summarize, using radar for robotics is less straightforward than other common sensors, whether due to processing on ADC Data that can be heavy and difficult, or since pre-processed pointclouds tend to be noisy and sparse. Nevertheless, this sensor is able to operate under extreme conditions and has the specificity to measure the radial velocity in addition to being a range and bearing sensor. The diversity of its parameters and processing possibilities allows adaptability to various scenarios.

2.4 Radar Operations

Most of the the radars used in robotics use frequency-modulated continuous waves (FMCW). The operating principle of an FMCW radar is illustrated in figure 2.5 and summarized by the following processing:

- Synthesis of a linear frequency modulated continuous waveform (LFMCW) called a frequency ramp
- Emission of this ramp through a transmitting antenna
- Reception by a receiving antenna of the backscattered signal corresponding to a sum of responses originating from the different scatterers in the scene, and consisting of the delayed and attenuated replicas of the transmitted signal.
- Combination of the emitted and received signal via a mixer to obtain an intermediate frequency (IF) signal
- Digitization of the IF signal via an Analog Digital Converter (ADC)

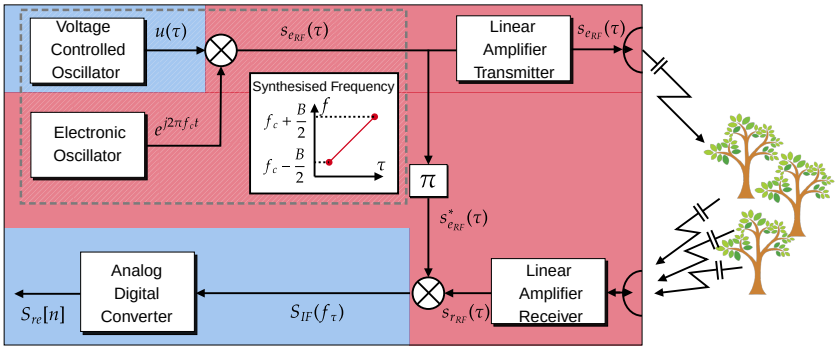

Figure 2.5: FMCW Radar Synopsis. Blue and red parts denote Low Frequency and RF elements respectively

We will now explicit and explain those steps. First, a voltage controlled oscillator (VCO) will create a baseband complex signal $u(\tau)$, typically a linear-frequency chirp signal which covers a bandwidth B during a period T_c, which can be written as :

$$u(\tau) = \begin{cases} e^{j\pi\gamma\tau^2}, & 0 < \tau < T_c, \\ 0 & otherwise, \end{cases} \tag{2.1}$$

with $\gamma = B/T_c$ the frequency slope in Hz/s and $f_\tau = \gamma\tau$ the instantaneous frequency at time τ. This signal is transposed via a mixer to the radio-frequency domain, f_c being the carrier frequency, yielding the RF chirp signal $s_{e_{RF}}(\tau)$ (illustrated in figure 2.6) having the following expression:

$$s_{e_{RF}}(\tau) = e^{j(\pi\gamma\tau^2 + 2\pi f_c \tau)}. \tag{2.2}$$

Then, this signal is amplified and sent as an electromagnetic wave via one of the transmitting antenna (Tx). This wave then impacts the different scatterers (objects) in the radar's field of view, giving rise to a backscattered signal $s_{r_{RF}}(\tau)$ measured

by one or more receiving antennas (Rx). This signal corresponds to the sum of the scatterers' contributions and is affected by n the receiver's additive noise such as:

$$s_{r,RF}(\tau) = \sum_k s_{r,k,RF}(\tau) + n(\tau). \tag{2.3}$$

The contribution $s_{r_k RF}(\tau)$ from the scatterer k at a distance r_k corresponds an attenuated, noisy and delayed version of the sent signal, and can be written as follows:

$$\begin{aligned} s_{r_k,RF}(\tau) &= a_k s_{e,RF}(\tau - \tau_k) \\ &= a_k e^{j\pi\gamma(\tau^2 - 2\tau\tau_k + \tau_k^2)} e^{j2\pi f_c(\tau - \tau_k)}, \end{aligned} \tag{2.4}$$

with the round trip delay $\tau_k = \frac{2r_k}{c}$, c the wave's celerity, a_k a coefficient. Next, the signal $s_{r_{RF}}$ is mixed with the conjugate of the transmitted signal $s^*_{e_{RF}}$. The mixing operation is called deramping or dechirping. It has two purposes: transposing the signal to the baseband and implementing a matched filter [Richards 2010b]. At the output of the mixer the beat or intermediate frequency (IF) signal $s_{\mathrm{IF,k}}(\tau)$ associated to scatterer k, illustrated in figure 2.7 can be written as:

$$\begin{aligned} s_{\mathrm{IF},k}(\tau) &= s_{r_k,RF}(\tau) s^*_{e,RF}(\tau) \\ &= a_k e^{j\pi\gamma(-2\tau\tau_k + \tau_k^2)} e^{-j2\pi f_c \tau_k} \\ &= a_k e^{-j2\pi f_c \tau_k} e^{-j2\pi f_\tau \tau_k} e^{j\pi\gamma\tau_k^2}. \end{aligned} \tag{2.5}$$

The last exponential term of $s_{\mathrm{IF},k}(\tau)$ is called the Residual Video Phase (RVP), it is undesirable and can be compensated but in our case, this term is considered negligible [Li 2021].

Fast-Time Sampling The IF signal associated to a scatterer k within one ramp can be written such as:

$$\begin{aligned} s_{\mathrm{IF},k}(\tau) &= (a_k e^{-j2\pi f_c \tau_k}) e^{-j2\pi f_\tau \tau_k} \\ S_{rf,k}(f_\tau) &= a_k e^{-j\phi_{0,k}} e^{-j2\pi f_\tau \tau_k}, \end{aligned} \tag{2.6}$$

with $\phi_{0,k}$ the phase considered to be constant within a chirp. $S_{rf,k}(f_\tau)$ corresponds to the spectrum of the range focused signal. This formulation is used to perform range measurement as it will be detailed in section 2.5.1.

Slow-Time Sampling As illustrated in Figure 2.8, by emitting a sequence of N_c chirps, separated by a pulse repetition interval T_{PRI}, the radar-scatterer motion will induce a Doppler shift. Previously, the signal processing has been detailed using a constant time delay τ_k, that choice correspond to the *stop-and-go* hypothesis. It assumes that the radar emits a signal and receives the response from the scene, then move to a new measurement position. In this thesis, this hypothesis is acceptable due to the low velocity of the rover v_R. (we verify $v_R T_{PRI} \ll \lambda_c$ and $v_R T_{PRI} \ll c/(2B)$). We can link the delay with the instantaneous radial velocity $v_{r,k}$ (or range

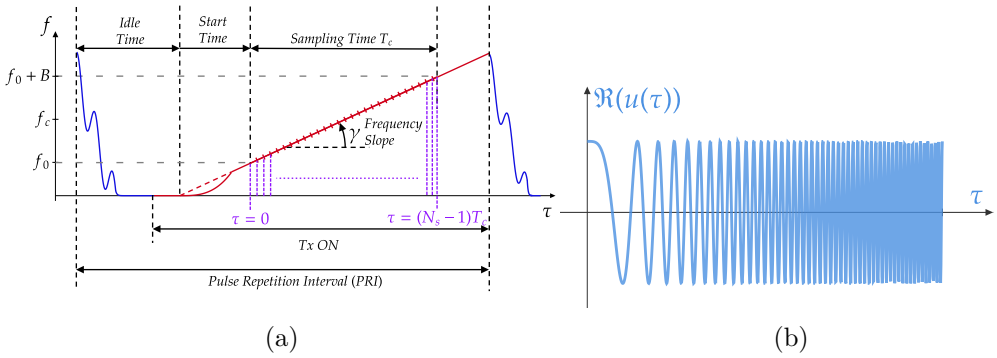

(a) (b)

Figure 2.6: (a) FMCW chirp signal
(b) Real part of the temporal baseband ramp signal

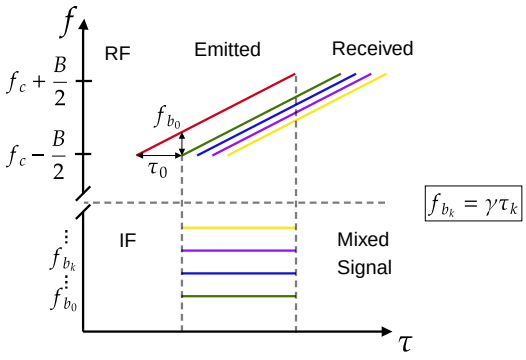

Figure 2.7: Contributions from several scatterers in RF and IF domains
Adapted from [Iovescu 2017]

rate $\dot{r_k}$) of the objects with respect to the radar such as :

$$\tau_k(t) = \frac{2r_k}{c} + \frac{2v_{r_k}}{c}t. \tag{2.7}$$

Since we have $\gamma T_c = B \ll f_c$, we can make the approximation $f_c + f_\tau \approx f_c$, considering then the slow-time sampled IF signal associated to the scatterer k within N_c chirps as a monochromatic wave:

$$s_{\text{IF,k}}(t) = a_k e^{j\psi_k} e^{-j\frac{4\pi}{\lambda_c}v_{r,k}t} \text{ , with } 0 \leq t \leq N_c T_{PRI}, \tag{2.8}$$

with $\psi_k = \frac{4\pi}{\lambda_c} r_k$. One of the strengths of the 77 GHz automotive radars is that, since their carrier's wavelength is so small, even tiny displacements result in a significant measurable phase shift. This formulation is used to perform radial velocity measurement as it will be detailed in section 2.5.2.

Spatial Sampling After fast- and slow-time sampling, the effect of spatial sampling will be now detailed. By using a radar with several antennas, it is possible to measure the angle of arrival of the object with respect to the sensor's frame $\mathcal{F}_\mathcal{S}$.

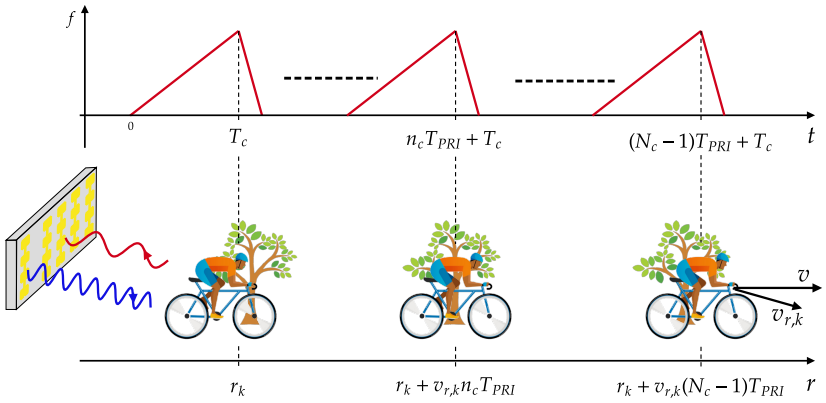

Figure 2.8: Sequence of emitted signals and impact on the phase of the received signal considering a moving scatterer

As illustrated in figure 2.9, Using at least two receiving elements, an inter-antenna phase difference can be measured due to the difference of distance travelled by the backscattered signal. By taking into account the planar case for now, using one emitting and two receiving elements each separated by a distance d, the phase shift at the two receiving element can be written as:

$$\Delta\phi = \frac{2\pi d}{\lambda}\sin(\theta) \Leftrightarrow \theta = \sin^{-1}\left(\frac{\Delta\phi\lambda}{2\pi d}\right). \tag{2.9}$$

Then, by considering N_a elements within an array, the delay $\tau_k(n_a)$ between the receiving element n_a and the scatterer k correspond to :

$$\tau_k(n_a) = \frac{2r_k}{c} + n_a\frac{d\sin(\theta_k)}{c}. \tag{2.10}$$

By using again the monochromatic wave assumption, the IF signal received at the antenna n_a can be written as:

$$S_{\mathrm{IF,k}}(n_a) = a_k e^{j\psi_k} e^{-j2\pi n_a \frac{d\sin(\theta_k)}{\lambda_c}} \text{ , with } 0 \leq n_a < N_a. \tag{2.11}$$

This formulation is used to perform angle of arrival measurement as detailed in section 2.5.3.

Finally, the signal is sampled using an analog-to-digital converter (ADC) yielding the raw ADC signal $s_{\mathrm{IF}}[n]$. The sampling is done during each sweep at a period $T_s = \frac{T_c}{N_s}$ with N_s the number of samples digitized during one chirp. In many cases, it will be used following three dimensions : delay (fast-time sampling), time (slow-time sampling) and receiving channel (spatial sampling), to yield the so-called *radar data cube* as illustrated in figure 2.10. Each sample n is associated to a range bin $n_s \in [0, N_s[$ sampled during the sweep $n_c \in [0, N_c[$ by the receiving element $n_a \in [0, N_a[$Each cube is associated to a frame N_f.

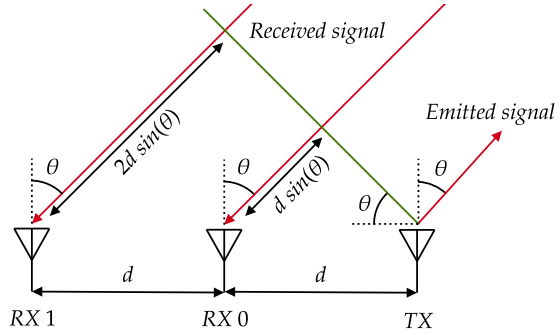

Figure 2.9: Difference of distance travelled by the backscattered signal to two receiving elements resulting in an inter-antenna phase difference

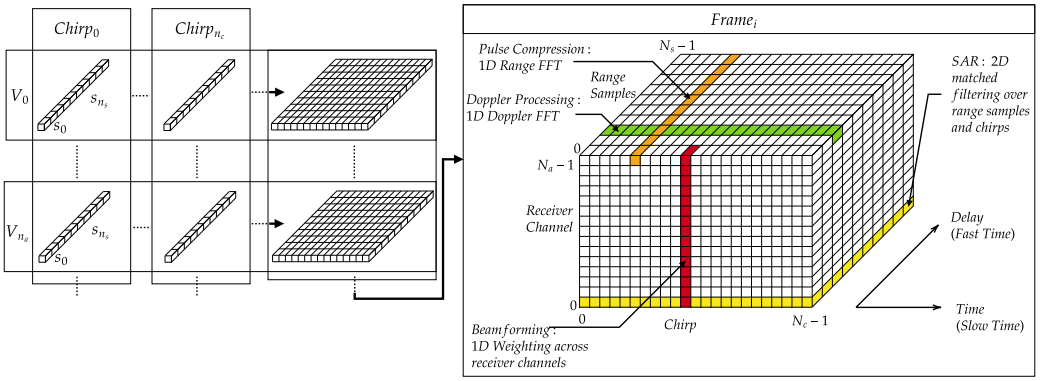

Figure 2.10: Radar Data Cube formation and processing associated to each dimensions. Adapted from [Richards 2010b]

2.5 Radar Signal Processing

This section will detail the classic radar signal processing along each dimension of the cube. By following these operations, which are a prerequisite for the contributions presented in this thesis, each cell of the cube can be associated with value for distance, radial velocity, and angle of arrival.

2.5.1 Range Measurement

From equation 2.6, the range focused signal $s_{\mathrm{IF}}[n_s]$ is then obtained with an inverse Discrete Fourier Transform (DFT):

$$\begin{aligned} s_{\mathrm{IF}}[n_s] &= \mathrm{DFT}^{-1}\left\{\mathbf{S}_{\mathrm{IF,k}}\right\} = \sum_{i=0}^{N_s-1} S_{\mathrm{IF,k}}(f_{\tau_i}) e^{j2\pi \frac{n_s i}{N_s}} \\ &= a_k e^{j\phi_{0,k}} \sum_{i=0}^{N_s-1} e^{-j\frac{2\pi i}{N_s}(\frac{2B}{c} r_k - n_s)} \\ &= a_k e^{j\phi_{0,k}} e^{-j\psi_k (N_s-1)/2} \frac{\sin(N_s\psi_k/2)}{\sin(\psi_k/2)} \\ &= a_k e^{j\phi_{0,k}} e^{-j\psi_k (N_s-1)/2} D_{N_s}(\psi_k). \end{aligned} \tag{2.12}$$

With $\psi_k = \frac{2\pi}{N_s}\left(\frac{2B}{c} r_k - n_s\right)$, $D_n(x) = \frac{\sin(nx/2)}{\sin(x/2)}$, the Dirichlet kernel or periodic sinc function. Notice that the modulus of that function correspond to:

$$|s_{\mathrm{IF}}[n_s]| = |a_k| \left| \frac{\sin(N_s\psi_k/2)}{\sin(\psi_k/2)} \right|. \tag{2.13}$$

The resolution is minimum value to make a distinction between two objects, in the case of the range resolution, r_{res} correspond to a distance. The Rayleigh criterion, defines it as the peak-to-first-null delay of the sinc function previously described. We can then write the range resolution such as:

$$r_{res} = \frac{c}{2B} = \frac{c}{2\gamma T_c}. \tag{2.14}$$

As an order of magnitude, typical bandwidths for a 24 GHZ and a 77 GHZ are 250 MHz and ∼1.5 GHZ respectively, which give respectively 60 cm and 10 cm of range resolutions.

For each type of measurement, a maximum unambiguous value of that measurement can be declared. In the case of range measurements, it can be derived from the periodicity of the function in equation 2.13, such as:

$$r_{amb} = \frac{f_s c}{2\gamma} = \frac{cN_s}{2B} = N_s r_{res}. \tag{2.15}$$

From this equation, we can note that using an FMCW radar, the sampling requirements are dictated by the frequency slope γ and the desired maximum range r_{amb}. Due to the link between r_{amb} and r_{res} a trade-off emerges: for a fixed sampling capacity, one must choose between extending the radar's maximum range or sharpening its range resolution. The sampling rate f_s acts as the primary hardware constraint.

TThe number of samples is also very important, as it will affect the SNR at the output of the processing. The signal-to-noise ratio of the focused signal SNR_{out}

corresponds to:

$$\mathrm{SNR}_{out} = N_s \mathrm{SNR}. \tag{2.16}$$

The concatenation of range focused backscattered signals over time corresponds to the backscattered signal spectrogram, it is often called a range profile and is illustrated in figure 2.11

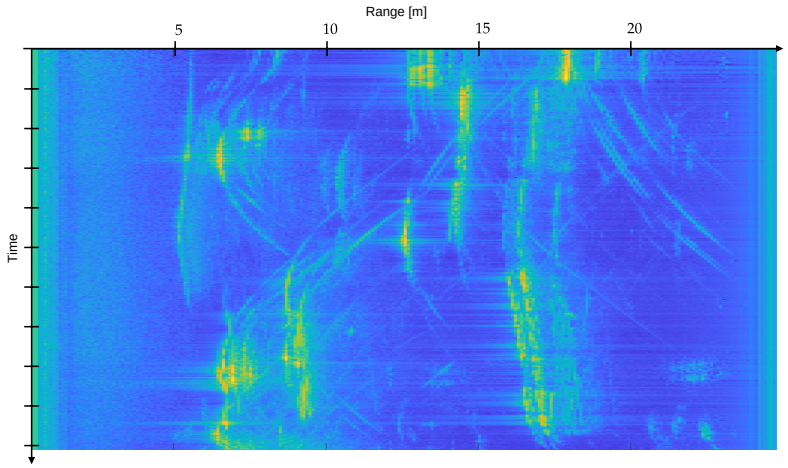

Figure 2.11: Range profile or backscattered signal spectrogram taken from a moving radar looking at a static scene

2.5.2 Radial Velocity Measurement

Radial velocity measurement is done via slow-time sampling across a sequence of N_c chirps. The received signal frequency is shifted accordingly to the scatterer-radar relative motion as detailed in equation 2.8. We can write the sampled Doppler-focused signal $s_{\mathrm{IF}}[n_c]$ via an inverse DFT on chirp to chirp samples such as:

$$\begin{aligned} s_{\mathrm{IF}}[n_c] = \mathrm{DFT}^{-1}\left\{\mathbf{S}_{\mathrm{IF,k}}\right\} &= \sum_{i=0}^{N_s-1} s_{\mathrm{IF}}(iT_{PRI}) e^{j2\pi \frac{n_c}{N_c} i} \\ &= a_k e^{j\psi_k} e^{-j\vartheta_k (N_s-1)/2} D_{N_c}(\vartheta_k), \end{aligned} \tag{2.17}$$

With $\vartheta_k = \frac{2\pi}{N_c}\left(\frac{2N_c T_{PRI}}{\lambda_c} v_{r,k} - n_c\right)$. We can again compute the radial velocity resolution by computing the peak-to-first-null length of the modulus of that function, yielding:

$$v_{r_{res}} = \frac{\lambda_c}{2N_c T_{PRI}}. \tag{2.18}$$

The radial velocity resolution depends on the number of chirps considered within a frame and T_{PRI}. In our case, the 77 GHZ modules can be set to get a resolution below 10 $\mathrm{cm.s}^{-1}$. Since we need to account for negative and positive radial velocities,

the maximum radial velocity measurable corresponds to:

$$v_{r_{max}} = \frac{N_c}{2} v_{r_{res}} = \frac{\lambda_c}{4T_{PRI}}. \tag{2.19}$$

Again, the number of chirps will have an impact on the SNR. The signal-to-noise ratio of the focused signal SNR_{out} corresponds to:

$$\text{SNR}_{out} = N_c \text{SNR}. \tag{2.20}$$

It is very common to achieve joint range Doppler processing to have access to both information simultaneously, for example using the so-called range Doppler map visualisation as shown in figure 2.12.

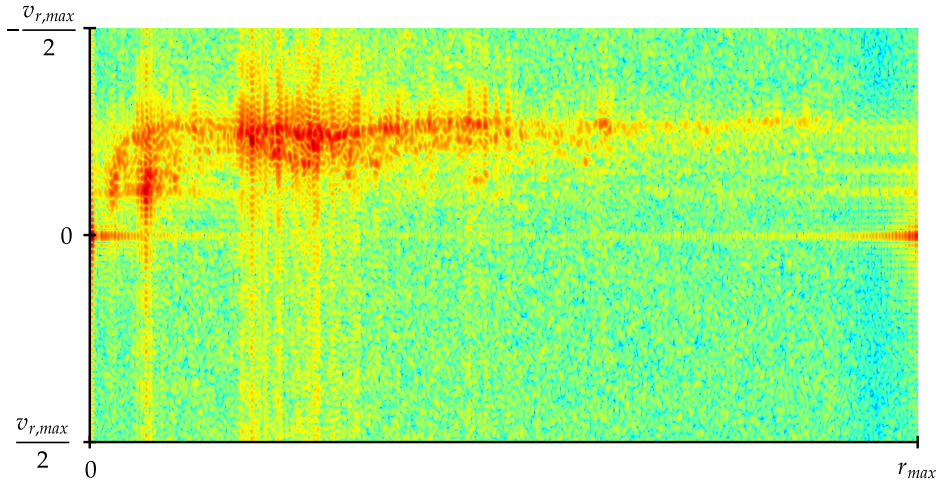

Figure 2.12: Range Doppler Map from a front facing moving radar, all the scatterers in its field of view are approaching the sensor

2.5.3 Angle of Arrival Measurement

Angle measurement is done via a spatial sampling of the received signal over several receiving elements. Thanks to the modelled signal in equation 2.11, we can write the Angle-focused signal $s_{IF}[n_a]$ via an inverse DFT on antenna to antenna samples such as:

$$\begin{aligned} S_{\text{IF}}[n_a] = DFT[s_{\text{IF}}(d_{n_a})] &= \sum_{i=0}^{N_a-1} s_{\text{IF}}(id) e^{-j2\pi \frac{n_a}{N_a} i} \\ &= a_k e^{j\psi_k} e^{\varphi_k (N_a-1)/2} D_{N_a}(\varphi_k), \end{aligned} \tag{2.21}$$

with $\varphi_k = \frac{2\pi}{N_a}\left(\frac{N_a d}{\lambda_c}\sin(\theta_k) - n_a\right)$. Here, we need to use an approximation to derive the angle resolution θ_{res} from the peak-to-first-null length of the modulus of the

function :

$$\begin{aligned} \sin(\theta)_{res} &= \frac{\lambda_c}{N_a d}. \\ &= \sin(\theta + \theta_{res}) - \sin(\theta) \\ \sin(\theta + \theta_{res}) &\approx \sin(\theta) + \theta_{res} \frac{\partial \sin(\theta)}{\partial \theta}, \text{ with first order approx.} \\ \Rightarrow \theta_{res} &= \frac{\lambda_c}{N_a d \cos(\theta)}, \end{aligned} \tag{2.22}$$

with θ the centered off-boresight scatterer-radar angle . We can also derive the maximum unambiguous angle θ_{max}. We need to take into account that FOV is centered, leading to:

$$\begin{aligned} \sin(\theta)_{max} &= \frac{N_a}{2} \sin(\theta)_{res}. \\ \Rightarrow \theta_{max} &= \sin^{-1}\left(\frac{\lambda_c}{2d}\right). \end{aligned} \tag{2.23}$$

We can emphasize that the more antennas we have (the larger the array is), the better the angle estimation will be. Also, we can say first, that the angular resolution depends on the angle of arrival itself, the more at the front an object will be, the better the resolution is. Secondly, an inter-antenna spacing of $\frac{\lambda_c}{2}$ gives an angular resolution of $\theta_{res} = \frac{2}{N_a cos(\theta)}$. Thirdly, it is essential to recognize that, in numerous radar datasheets, the specified azimuth and elevation resolutions are given for a boresight detection, i.e. at the point of maximum antenna gain. Consequently, these values represent the optimal (and theoretically highest) attainable resolution under ideal conditions. It is important to note that the advertised accuracy in radar systems is contingent upon both the angle of arrival and the signal-to-noise ratio (SNR) of the target. While increasing the number of antennas improves angular resolution, this approach significantly escalates system costs, as each receiver element requires dedicated components, including a low-noise amplifier (LNA), mixer, and analog-to-digital converter (ADC). To address this challenge, techniques for constructing large array antennas with fewer physical elements will be detailed.

The type of system used in this thesis are Multiple-Input Multiple-Output (MIMO) radars having N_e emitting and N_r receiving antennas positioned respectively at $\mathbf{x}_e$ and $\mathbf{x}_r$. In figure 2.13 such a system is illustrated. By assuming that receivers can distinguish the signals coming from different emitters, we can write the travelled distance of the signals elements to elements such as:

$$\begin{array}{ll} TX0 - RX1 & 2r + 2dsin(\theta) \\ TX0 - RX0 & 2r + dsin(\theta) \\ TX1 - RX1 & 2r \\ TX1 - RX0 & 2r - dsin(\theta) \end{array}$$

An amplitude of phase shift would have been the same using a 1TX-4RX array. A MIMO array, will then result in a set of $N_a = N_e N_r$ virtual antennas positioned at

$\mathbf{x}_a$ such as:

$$\mathbf{x}_{a,n_a} = \frac{\mathbf{x}_{e,n_e} + \mathbf{x}_{r,n_r}}{2}, n_r \in [1, N_r], n_e \in [1, N_e], n_a \in [0, N_e N_r[. \tag{2.24}$$

This formula expresses the fact that even if this system can be considered as a pseudo-bistatic radar, since the distances between emitting and receiving elements are small compared to the distance to the objects, they are equivalent to an array of monostatic systems located at the center positions of emitting and receiving elements as illustrated in figure 2.14. Now let's notice a few important points:

- Firstly, that the spacing between emitting and receiving elements is not important (since the system can still be considered as monostatic), what is relevant, are the inter-receiver and inter-emitter distances.
- Secondly, having a constant receiving elements spacing of $\lambda_c/2$ will result in a sub-array of antennas with a spacing of $\lambda_c/4$, it is not an issue since the virtual antennas are equivalent to a transceiver.
- Thirdly, as can be seen in figure 2.14, if we build the array so that $N_{a,az}$ antennas are on a same horizontal plane, they will be able to measure an azimuthal angle, equivalently, with $N_{a,el}$ antennas on a common vertical plane, they will be able to measure an elevation angle. Having both configuration simultaneously allows to locate a scatterer in three dimensions.
- Finally, even if a MIMO system appears as an engineering dream, it reduces the cost by requiring less antenna and electronics associated, reduces the form factor, reduces the amount of data to collect, etc. , they are some negative externalities. One of them comes from the first assumption that we made, the ability to distinguish the signals coming from different emitters. This is done by using dedicated MIMO waveforms. In this thesis, we used radars use Time Division Multiplexing (TDM).

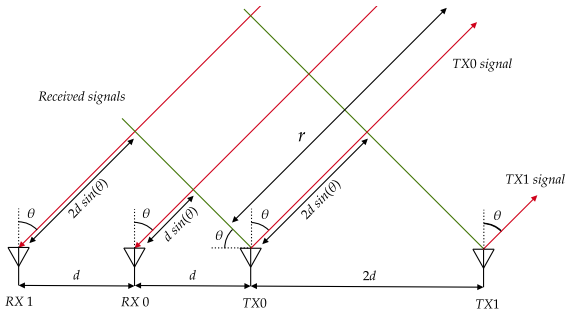

Figure 2.13: Multiple-Input Multiple-Output antenna array

We have explained what are the data that composes the radar cube and the basic processing that can be done to turn raw data into exploitable data. Each cell of the cube has a complex value and its location is related to a range, a radial velocity, and an angular phase. We will now see how to perform detection on this cube.

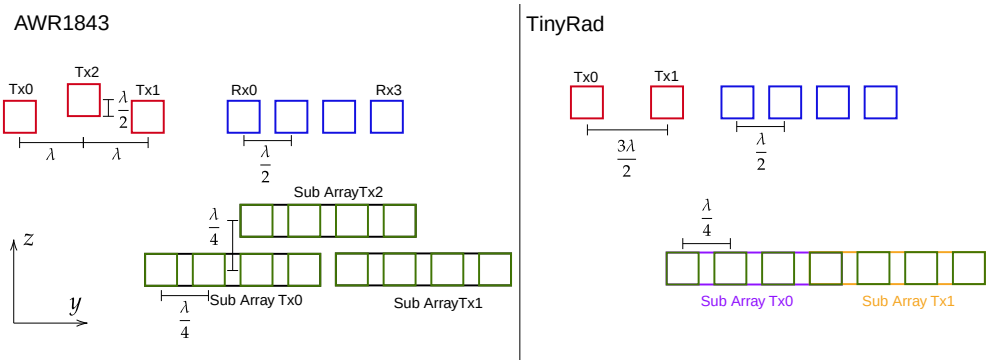

Figure 2.14: Real and Virtual arrays of elements for two different radars, AWR1843 and TinyRad. In red, blue and green are respectively emitters, receivers and virtual antennas. On the left, since an emitter is shifted vertically, the virtual array fills two vertical position. On the right, the array is linear and we can notice that the pair Tx0-Rx3 and Tx1-Rx0 give virtual elements located at the same position.

2.6 Radar In Practice

2.6.1 Constant False Alarm Rate Detector

Logically, since the volume that the radar FOV covers is not filled, the cube is composed of a lot of non-interesting data. The goal of the detection is to determine what are the parts of the data cube that are related to scatterers of interest among noise and clutter. It exists various ways to perform detection using radar raw data but the most common tool is definitely the *Constant False Alarm Rate* (CFAR) detector [Diao 2024]. This algorithm is the foundation of radar pointcloud generation (see next section) and has been used in chapter 5. The application of CFAR detector uses the magnitude of the signal on the different dimensions of the radar cube. It exists many different CFAR methods [Weiss 1982], we will describe in this section some common ones that have been used during this thesis.

A very simple detector would be to define a constant threshold to determine if whether a certain amplitude corresponds to a scatterer or not. To take into account for the radar intrinsic parameters, it would need to be dependant on at least the range and angle, due to distance attenuation and antenna aperture respectively. Unfortunately, by doing this, the detector would be not robust to noise or clutter and require fine tuning depending on the use case. The aim of the CFAR is to estimate the noise level of a certain neighbourhood of each Cell-Under-Test (CUT) to appropriately scale an adapted threshold. The working principle of the CFAR is illustrated in figure 2.15. For each CUT, we will define training (or reference) cells forming right and left windows, separated from the CUT by a certain number of, unused, guard cells. From the training cells, the noise level (background) will be estimated while the guard cells are here to account for the case of a scatterer leaking on several cells. First, the Cell Averaging CFAR (CA-CFAR) estimates the background noise by averaging the mean amplitude of each left and right windows.

The Cell Averaging Greatest-Of and Smallest-Of CFAR(CAGO- and CASO-CFAR) also compute mean amplitude of right and left windows and keeps the maximum and minimum value respectively as the noise level estimate. Finally, the Ordered Statistic CFARs will sort the amplitude values in order for example to use the median value as the noise level (OS-CFAR), or discard highest value and compute the mean (CAOS-CFAR). In table 2.2, those CFAR detector are compared following their ability to perform in presence of clutter and interfering targets. In the case of clutter, the performance is based on the ability to detect finely the clutter edges. In the context of interfering targets, the adequate detector will be able to detect two or several scatterers that are close in the considered dimension (i.e. range).

Detector / Scenario	CA-CFAR	CAGO-CFAR	CASO-CFAR	OS-CFAR
Clutter	Poor	Good	Poor	Good
Close Targets	Poor	Poor	Good	Good
Computation Time	Low	Low	Low	High

Table 2.2: CFAR detectors performances and computational time

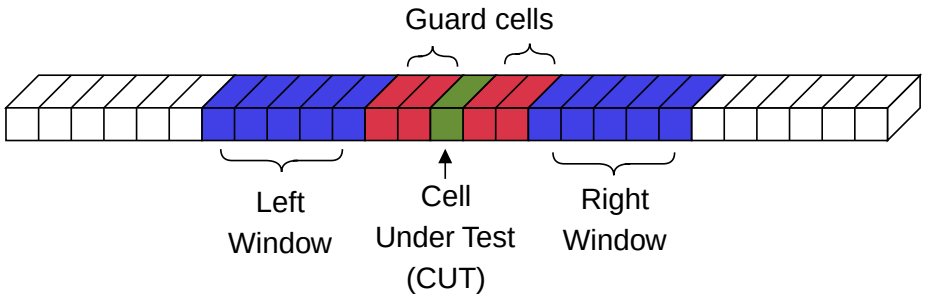

Figure 2.15: 1D CFAR principle

2.6.2 Point Cloud Generation

The creation of a point cloud of detected scatterers from the raw data cube is a common aspect of the radar signal processing in various radar domains. Numerous approaches exist, two common methods will be detailed in this section.

First, the one illustrated in figure 2.16 corresponds to the most classic approach to get a list of radar detections. A 3D DFT is performed on the full radar cube so that each cells is associated to a range, a radial velocity and an angular phase. Range-Doppler CFAR is applied so that if several scatterers are at a same range but different radial velocity they still can be detected. Then, depending on the geometry of the array, the angle of arrival of the detections is retrieved to have a Cartesian pointcloud. This method is simple but can be cost computationally expensive since the whole cube is processed. Another method depicted in figure 2.17

consists in perform a range IDFT on the cube. Then, a range CFAR will give the indices of samples of interests on which a Doppler-angle DFT is performed. Then a Doppler CFAR will allow to differentiate detections velocity-wise, the pointcloud is finally obtained via the same angle extraction. This method is less straight-forward but saves operations on the Doppler-Angle dimensions of the cube which can be interesting if samples are stored contiguously, the access of other dimensions is then slower.

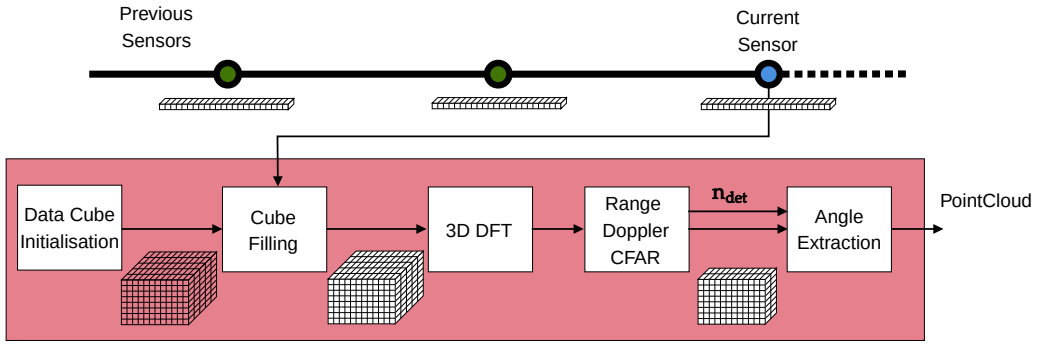

Figure 2.16: Pointcloud formation via a 3D DFT and one CFAR

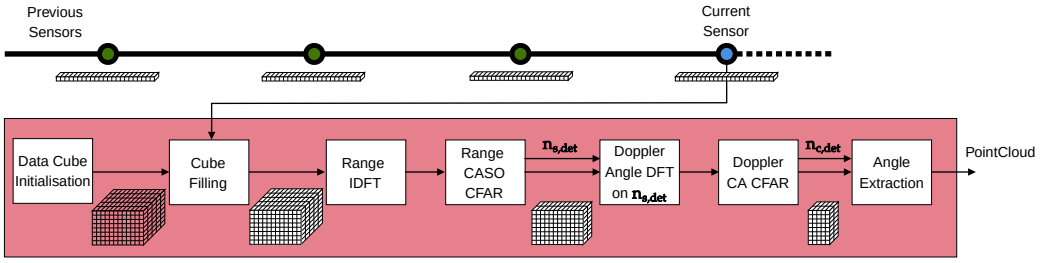

Figure 2.17: Pointcloud formation via successive DFTs and CFARs

2.7 Conclusion And Discussion

In this chapter we have introduced the radar, his history in general and in robotics. We compared it to other traditional exteroceptive sensors in robotics. We have presented how it works, the signal involved and to perform basic measurements. Then, we have seen the classic pipelines to generate a point cloud from raw data.

Now, I would like to make a discussion about the radar in robotics in practice. In my opinion, this sensor is under considered mainly due to a lack of standards and open sourced resources. While for computer vision and image processing it exists for example OpenCV and for pointcloud processing there is PCL library, there is (to my knowledge, at the moment of writing this) no open-source and actively maintained library dedicated to basic radar processing. There are probably a few reasons to that.

- The **diversity of processing and hardware possibilities** that a radar admit. The range of processing that can be performed on raw data makes the radar as a highly polyvalent and capable sensor, but it can be a repellent to standardisation. If you want to have fully access to the parametrization of your radar, you will basically not buy a radar but build it. Then, you are able to set the polarization, directivity, gain, number, positions, etc., of antennas, to use various waveforms, emitting schemes, samplings. It is still common to build a radar for a robotic application [Bähnemann 2022], while it is not at all for a camera and a lidar.
- The **late arrival of System-On-Chip (SoC) radars** as a standard hardware. Probably due to the previously cited reason, its only since the automotive industry had a need for mass produced radars that standards appeared. Before having access easily to a MIMO or rotating radar with common capabilities and way of working, researchers had to rely on in-house produced systems. Those were very hard to replicate and were often designed for specific applications (e.g. [Brooker 2007]).
- **Radar data processing and visualisation are less straightforward** than a colour or grayscale image or a high resolution lidar pointcloud from our human-being point of view. Also, the phenomena involved (multipath, ghost targets, clutter, etc) and measurement model (variability of occlusion, ambiguities) [Werber 2015] to consider are different than with other exteroceptive sensors

Finally, radar admit one of the widest diversity of information and robustness within the vision robotics field. It is increasingly used via pre-processed pointcloud and it is a good point regarding the ease of use and computational cost. Nevertheless, the field would benefit from open-sourced raw data based basic and advanced processing implementations.

Chapter 3

Radar Localisation

Contents

3.1 State Of The Art 26
3.1.1 State Of The Art on Point Cloud based Radar Localisation . 26
3.1.2 State Of The Art on Raw Data based Radar Localisation . . 28
3.1.3 Discussion 29
3.2 Single-scan state estimation 29
3.2.1 Ego-Velocity Measurement Model 30
3.2.2 Tightly-Coupled 2D Odometry 31
3.2.3 Validation on Simulation 32
3.2.4 Radar Calibration 33
3.2.5 Validation of Calibration and Odometry on Real Data 40
3.2.6 Conclusion 41
3.3 Scan-to-Scan estimation 43
3.3.1 Scan Formation 43
3.3.2 Results with Real data 47
3.4 Conclusion And Perspectives 48

One of the main challenge in mobile robotics is localization. Mobile robot localization is the problem of determining the pose of the robot along an unknown trajectory. It can be formulated as the problem of estimating the transformation between the robot frames over time. It can rely on proprioceptive information, e.g. wheel encoder, Inertial Measurement Unit (IMU), Global Navigation Satellite System (GNSS), and on exteroceptive measurements, from a camera, a lidar or in our case a radar. The main difference between these two type of informations is that only exteroceptive measurements allows environmental perception. Also, for localisation purpose, proprioceptive information will often give an immediate information on the robot state (e.g acceleration, angular velocity, etc.). On the other hand, using exteroceptive information, the robot state needs to be estimated via for example : correspondences between current measurement and past measurements aggregated in a local (*reduced* SLAM) or global map (SLAM) [Cadena 2016], external information, e.g. known map (re-localisation). In this chapter, we address the localization problem with the assumption of static environment using only radar measurements.

First, a state of the art of this field is proposed. Note that, we classified the studies depending on whether it is based on single-scan odometry, scan-to-scan odometry or Simultaneous Localization and Mapping (SLAM).

3.1 State Of The Art

It is important to notice that the pioneering works in the domain of radar odometry and SLAM have been done using rotating radars and demonstrated outstanding localisation results [Dissanayake 2001, Brooker 2001, Brooker 2007, Adams 2012, Gerossier 2009, Checchin 2010, Vivet 2013]. Also, in recent years there has even been a resurgence of publications in this field with again excellent results in large-scale and long-term localisation and mapping [Hong 2020, Burnett 2021, Weston 2022, Adolfsson 2023a, Adolfsson 2023b, Frosi 2024, Gentil 2025]. These works admit similar processing and frameworks (Doppler based odometry, scan-matching, SLAM) but a rotating radar is still very different compared to a fixed array one. With a 360° FOV, a high angular resolution ($\sim 1°$) and long range capability, the rotating radar is strongly suited for place recognition and dense scan-to-map matching. Moreover, one important difference between the two type of sensors, is that a rotating radar is generally not coherent, i.e. not SAR capable. In the context of this thesis rotating range radar are non relevant sensor. We will then focus the remaining of this state of the art on MIMO coherent fixed array radar.

3.1.1 State Of The Art on Point Cloud based Radar Localisation

3.1.1.1 Single-Scan Odometry

In the context of radar localisation, a single-scan odometry is possible thanks to the Doppler and angle of arrival informations that give us the ability to infer the instantaneous radar velocity. This velocity can be integrated over time to estimate the travelled trajectory using the radar. Kellner *et al.* [Kellner 2013, Kellner 2014] presented a mono- then multi-radar 2D odometry based on this principle that has established a standard in the community: the instantaneous ego-motion estimation. It uses RanSaC algorithm to discard wrong detections (false alarm, ghost target, etc.) or moving objects. The ability to estimate both linear and angular velocity relies on the knowledge of the sensor-vehicle calibration and on the Ackerman hypothesis (no side-slip at rear axis). Corominas-Murtra*et al.* [Corominas-Murtra 2016] extended this work by removing the Ackerman condition using a bi-radar setup in a "stereo" fashion. Through an observability analysis they provided an optimal sensor placement and showed odometry results under optimal and non-optimal configurations. After that, Doer and Trommer [Doer 2020a, Doer 2020b] integrated the RanSaC LSQ based twist estimation with Inertial Measurement Unit (IMU) data in a loosely coupled Error-State Extended Kalman Filter (ES-EKF). Extensions to 3D have then been proposed by Ng *et al.* [Ng 2021] with a continuous time

multi-radar inertial 3D odometry. Park et al. [Park 2021] proposed a 3D pose graph multi-radar odometry. They use a setup composed of two radar one facing forward and the other downward. Huang et al. [Huang 2024] proposed a factor graph-based multi-radar inertial 3D odometry using two forward facing radar one rotated horizontally and the other vertically. These two works use such setups to compensate the fact that many off-the-shelf radars admit antenna array populated mostly over one axis (implying a low angle accuracy in the other axis). Chen *et al.* [Chen 2023] presented a radar inertial odometry relying on ground extraction in structured environments to improve the robustness of the estimation. Finally, in [Chen 2024c], a tightly-coupled continuous time Radar-Inertial velocity estimator is proposed.

3.1.1.2 Scan-To-Scan Odometry

Scan-to-scan odometry consists in finding correspondences between two consecutive sets of data to estimate the relative displacement. Rapp *et al.* [Rapp 2015] proposed an odometry using a joint spatial- and Doppler-based estimation. They map the detections using a k-means clusterisation and perform scan-matching using a Doppler-weighted Normal Distribution Transform (NDT). Michalczyk *et al.* [Michalczyk 2022] presented a tightly-coupled radar-inertial EKF relying on the prediction of both Doppler and position of all the targets associated via a Munkres algorithm. Galeote-Luque *et al.* [Galeote-Luque 2023]. Kubelka *et al.* [Kubelka 2023] provided a comprehensive study in diverse environments questioning the need for scan-matching versus single-scan estimation in radar(-inertial) odometry. They conclude that using a modern high-end[1] MIMO radar is more suited to closed or indoor environment (such as mine) but is outperformed by scan-matching in open environments (forest, car park scenario) especially for the orientation and elevation estimation. Do *et al.* [Do 2024] presented a radar odometry using a stochastic cloning indirect EKF (SC-IEKF) using data from radar point clouds and an IMU. The point cloud is first used to estimate velocity via a RanSaC-LSQ estimation and fused with the gyroscope to have a prior pose estimate. Then, each set of inliers is gathered over a window of n scans and registered to the previous window sets via the Iterative Closest Point (ICP) algorithm. Finally, using information from prior estimates, the accelerometer and the registration a measurement update and correction is done to estimate the transform between current frame and the n-th past one. Zhang et al. [Zhang 2024] proposed a generalized-ICP (GICP) algorithm which uses plane-to-plane matching between radar keyframes. Kim *et al.* [Kim 2024a] employed a 2D two-way weighted ICP on point clouds rectified thanks to single-scan velocity estimation providing a mono-radar 2D odometry. Girod *et al.* [Girod 2024] presented a baro-radar-inertial odometry using a factor-graph m-estimator. They noticed that in comparison to other exteroceptive sensors, their

[1] High-end is denoted here to high angular accuracy thanks to densely populated antenna array, i.e the radar used in the cited article has 2304 virtual elements allowing horizontal and vertical resolution of 1.25° and 1.7° respectively

setup achieved outstanding robustness in the context of drone trajectory in both urban and forest environments. Recently, a few works have proven that it is possible to use KISS-ICP [Vizzo 2023] with radar point clouds providing an easily integrable scan-to-submap matching solution. Kim *et al.* [Kim 2024b] demonstrated its use on a local polar grid filled with RCS-velocity filtered radar point clouds. They showed promising results in both localisation accuracy and computation time. Similarly, Herraez *et al.* first in [Herraez 2024] proposed to extend the ICP used by KISS-ICP to a Doppler ICP (DICP) as presented by Hexsel *et al.* [Hexsel 2022]. Then, in addition to the first velocity-based point cloud filtering, they proposed an extension [Herraez 2025] with RCS and ground heuristics.

3.1.1.3 SLAM

The main difference between single-scan, scan-to-scan and SLAM approaches is the fact that information is kept all along the process via a global map for possible loop closure techniques (i.e. via bag of words). First, Holder *et al.* [Holder 2019], proposed a multi-sensor pose-graph SLAM. It relies on an UKF fusing radar-based velocity estimate, wheel speed, steering angle and gyroscope for an odometry solution, scan-to-scan matching and loop closure between submaps. Then, Almalioglu *et al.* [Almalioglu 2021] within their Milli-RIO work, presented a solution based on scan-to-map matching via a NDT. The global map is created by iterative k-mean clusterisation of the Munkres' associated detections. As an input of the NDT they rely on a gyroscope integration and on a Long Short Term Memory (LSTM) as motion model for state prediction. Recently, several works have been presented using radar-based pose-graph SLAM with single-scan velocity, scan-to-scan registration and loop-closure factors. Li *et al.* [Li 2023] uses a point cloud filter using ground and previous scan based heuristics. Also, their loop-closure is done using intensity-based modified ScanContext [Kim 2018]. Zhang *et al.* [Zhang 2024] proposed a similar solution with an optional integration of both barometer and GPS. Zhuang *et al.* [Zhuang 2023] proposed a Kalman filter based RIO extended with a loop detection triggering Global ICP (GICP) and pose-graph for odometry and global map refinement.

3.1.2 State Of The Art on Raw Data based Radar Localisation

The studies presented previously are mainly from the robotics community and thus use as an input 3D or 4D data pre-processed point clouds. However, recently, within the radar community, numerous studies have been published presenting localisation based radar raw data. The single-scan velocity estimation based odometry have been employed in several studies [Steiner 2020, Gao 2021, Iqbal 2021]. Grebner *et al.* , using a car-mounted radar network, integrated this method in a graph-based SLAM with feature based matching between occupancy grid maps and a loop-closure detection [Grebner 2024]. Yuan *et al.* [Yuan 2023b] proposed a 3D localisation based on single-scan velocity estimation for translation estima-

tion and consecutive scan matching using Kabsch algorithm [Kabsch 1976] for rotation estimation. Manzoni *et al.* [Manzoni 2023a, Balducci 2023] proposed an autofocus-based Bayesian tracking of residual motion for rectilinear trajectory. Using salient points on a set of MIMO-SAR images, they compute their residual angular Doppler frequency to infer a velocity error giving the ability to both correct the estimated trajectory and the quality of the SAR mapping. Finally, Lubanco *et al.* [Lubanco 2024] proposed a pose-graph SLAM relying on Fourier-Radon transform for rotation estimation, Doppler based velocity estimation for the translation and a Radon transform based loop-closure.

3.1.3 Discussion

From this section, we can acknowledge that the radar-based localisation has given rise to a wide variety of work which, together with the evolution of the sensor itself, makes this field of research particularly active due to contributions from both the robotics and radar communities. However, many existing solutions rely on multi-sensor fusion, often integrating IMU or other complementary sensors. While effective, this approach introduces additional complexity in, data synchronization, and algorithmic integration.

In our work, we address these challenges by focusing on a radar-only localisation solution, using for both lateral- and forward-looking radars. This choice is motivated by two main factors. First, simplifying the sensor suite by avoiding the need for additional type of sensor, thereby reducing system complexity. Secondly, a lateral radar is more effective for SAR imaging, while a forward-facing radar provides necessary data on the terrain ahead of the rover.

In the next sections we will detail the contributions in both single-scan and scan-to-scan estimation. The single-scan estimation consists in a multi-radar Doppler-based single-scan 2D odometry. The approach is first validated through simulation, then to validate it on real data, a calibration is needed. Then, we proposed a multi-radar calibration process tailored for skid-steering rovers, also validated in simulation. After that, since odometry performance depends on both radar placement and calibration quality, we perform an observability analysis to optimize sensor positioning, focusing on the observability of both velocimetry and calibration parameters. We then validate the calibration and odometry methods using real-world data.

3.2 Single-scan state estimation

To estimate the rover trajectory we first propose to evaluate a single-scan approach.

While many state-of-the-art solutions rely on an IMU and the use of optimization for ego velocity estimation, our fully filter-based algorithm uses an Implicit Extended Kalman Filter to predict each target's radial velocities based on their angle of arrival and the vehicle states $[v, \omega]$ to estimate its 2D trajectory. We propose a matching- and tracking-free approach that does not rely on additional IMU

sensors.

3.2.1 Ego-Velocity Measurement Model

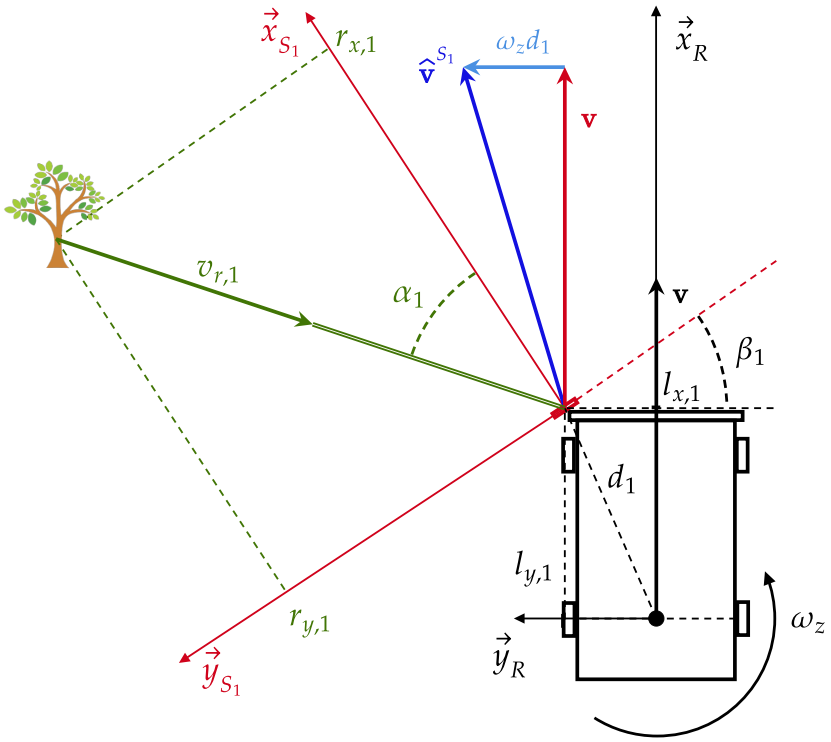

Figure 3.1: Frame convention - in black robot frame, in red sensor frame

Considering a set of radar detections, it is possible to estimate the radar velocity using only the information of radial velocity and angle of arrival. As illustrated in figure 3.1 for the 2D case, the radial velocity of the detected static targets corresponds to the projection of the radar's velocity $\mathbf{v}^S = [v_x^S, v_y^S, v_z^S]$ in the direction of observation (azimuth angle α in the figure). Thus, we can express in equation 3.1 the radial velocity $v_{r,j}$ associated with detection j obtained in the direction $\mathbf{r_j} = \frac{\mathbf{p_j}}{\|\mathbf{p_j}\|}$, with $\mathbf{p}$ the 3D position of the detection the radar frame.

$$\underbrace{\begin{bmatrix} v_{r,1} \\ v_{r,2} \\ v_{r,j} \\ \vdots \end{bmatrix} = \begin{bmatrix} r_{x,1} & r_{y,1} & r_{z,1} \\ r_{x,2} & r_{y,2} & r_{z,2} \\ r_{x,j} & r_{y,j} & r_{z,j} \\ \vdots & \vdots & \vdots \end{bmatrix} \begin{bmatrix} v_x^S \\ v_y^S \\ v_z^S \end{bmatrix}}_{\mathbf{y}=\mathbf{H}\mathbf{v}^S}. \tag{3.1}$$

Finally, the estimated radar's velocity $\hat{\mathbf{v}}^S$ is obtained using one scan via a least squares minimisation (LSQ):

$$\hat{\mathbf{v}}^S = \left(\mathbf{H}^T\mathbf{H}\right)^{-1}\mathbf{H}^T\mathbf{y}. \tag{3.2}$$

3.2.2 Tightly-Coupled 2D Odometry

This section proposes the extension of the methodology to multiple radars.

Measurement Model If we consider the 2D case, using the pose of the radar i in the vehicle frame, the radar's velocity $\mathbf{v}^{S_i}$ is provided by the equation 3.3.

$$\mathbf{v}_i^{S_i} = \mathbf{R}_R^{S_i}\left(\mathbf{v} + \begin{bmatrix} 0 \\ 0 \\ \omega_z \end{bmatrix} \times \begin{bmatrix} l_{x,i} \\ l_{y,i} \\ 0 \end{bmatrix}\right), \tag{3.3}$$

with $[l_x, l_y]$ and $\mathbf{R}_R^{S_i}$ the translation vector and rotation matrix between the robot and the sensor frames and $\mathbf{v}$ and ω_z the linear and rotational velocities of the vehicle. Thus, from equations (3.1) and (3.3), we can then write the expected radial velocity of a target $\hat{v_{r,ij}}$ depending on its angle of arrival α_{ij} as:

$$\begin{aligned} \hat{v_{r,ij}} &= (v_x - \omega_z l_{y,i})\cos(\beta_i + \alpha_{ij}) + (v_y + \omega_z l_{x,i})\sin(\beta_i + \alpha_{ij}) \\ &= (v_x - \omega_z l_{y,i})\cos(\phi_{i,j}) + (v_y + \omega_z l_{x,i})\sin(\phi_{i,j}) \end{aligned} \tag{3.4}$$

With β_i the angle around $\overrightarrow{z}$ axis between robot and radar i frames. Unfortunately, the Jacobian of $\hat{v_{r,ij}}$ with respect to $[v_x, v_y, \omega_z]$ is not of full rank since we can write relation:

$$-l_{y,i}\frac{\partial \hat{\mathbf{v}}_\mathbf{r}}{\partial v_x} + l_{x,i}\frac{\partial \hat{\mathbf{v}}_\mathbf{r}}{\partial v_y} = \frac{\partial \hat{\mathbf{v}}_\mathbf{r}}{\partial \omega_z}, \tag{3.5}$$

With $\hat{\mathbf{v}}_\mathbf{r} = [\hat{\mathbf{v}}_{\mathbf{r},0}, \ldots, \hat{\mathbf{v}}_{\mathbf{r},i}, \ldots]^T$ and $\hat{\mathbf{v}}_{\mathbf{r},i} = [\hat{v_{r,i0}}, \ldots, \hat{v_{r,ij}}, \ldots]^T$. To solve this issue, we can use a stereo-radar configuration [Corominas-Murtra 2016] but a common way in an Unmanned Ground Vehicle (UGV) configuration is to rely on the hypothesis which places the origin of the vehicle frame where there is null lateral velocity $v_y = 0$ (center of rear-axis for an Ackermann vehicle or equidistant point of the wheels for a skid-steering vehicle). Finally, we can write the measurement model linking the state of the vehicle $[v_x, \omega_z]$, and the angle of arrival of a target to the expected radial velocities as:

$$\begin{aligned} \hat{v_{r,ij}} &= (\hat{v_x} - \hat{\omega_z} l_{y,i})\cos(\beta_i + \alpha_{ij}) + \hat{\omega_z} l_{x,i}\sin(\beta_i + \alpha_{ij}) \\ &= (\hat{v_x} - \omega_z l_{y,i})\cos(\phi_{i,j}) + \hat{\omega_z} l_{x,i}\sin(\phi_{i,j}). \end{aligned} \tag{3.6}$$

Notice that this measurement model is working with one or more radar and it will be denoted as the function $h(\hat{\mathbf{x}}, \alpha) = \hat{\mathbf{v}}_\mathbf{r}$.

Motion Model The state of the system is composed of the 2D pose of the vehicle $[x, y, \theta]$ and its linear and angular velocities $[v, \omega] = [v_x, \omega_z]$. The global state $\mathbf{x}_k$ at time k related to the vehicle can be written $\mathbf{x}_k = [x, y, \theta, v, \omega]^T$.

The motion model of the system follows a Constant Velocity and Turning Rate (CTRV) model with equation 3.7.

$$\begin{aligned}\mathbf{x}_{k+1} = \begin{bmatrix} x_{k+1} \\ y_{k+1} \\ \theta_{k+1} \\ v_{k+1} \\ w_{k+1} \end{bmatrix} &= \begin{bmatrix} \frac{v_k}{w_k}\sin\left(w_k\Delta t + \theta_k\right) - \frac{v_k}{w_k}\sin\left(\theta_t\right) + x_k \\ -\frac{v_k}{w_k}\cos\left(w_k\Delta t + \theta_k\right) + \frac{v_k}{w_k}\cos\left(\theta_k\right) + y_k \\ w_k\Delta t + \theta_k \\ v_k \\ w_k \end{bmatrix}, \quad w \neq 0. \\ &= \begin{bmatrix} v_k\cos\left(\theta_k\right)\Delta t + x_k \\ v_k\sin\left(\theta_k\right)\Delta t + y_k \\ \theta_k \\ v_k \\ 0 \end{bmatrix}, w = 0.\end{aligned} \tag{3.7}$$

Filter The presented measurement model requires the angle of arrival to obtain the expected radial velocity of the target. Such formulation of the observation model is implicit (some observations are dependent on other observations). We then use classical Implicit Extended Kalman Filter (IEKF) equations to compute the innovation and its associated covariance according to equation 3.8, with the observation function h given by equation 3.6 and $\mathbf{H}_\alpha$ and $\mathbf{H}_\mathbf{x}$ are respectively the Jacobians of this h function relative to the angle of arrival and the vehicle state.

$$\begin{aligned}\tilde{\mathbf{y}}_k &= \mathbf{v}_{\mathbf{r},k} - h\left(\hat{\mathbf{x}}_{k|k-1}, \alpha_k\right) = \mathbf{v}_{\mathbf{r},k} - \hat{\mathbf{v}_{\mathbf{r},k}}. \\ \mathbf{S}_k &= \mathbf{H}_{\mathbf{x},k}\mathbf{P}_{k|k-1}\mathbf{H}_{\mathbf{x},k}^T + \mathbf{R}_{v_r,k} + \mathbf{H}_{\alpha,k}\mathbf{R}_{\alpha,k}\mathbf{H}_{\alpha,k}^T.\end{aligned} \tag{3.8}$$

$$\mathbf{H}_\mathbf{x} = \begin{bmatrix} \frac{\partial h(\mathbf{x},\alpha_0)}{\partial v} & \frac{\partial h(\mathbf{x},\alpha_0)}{\partial \omega} \\ \vdots & \vdots \\ \frac{\partial h(\mathbf{x},\alpha_i)}{\partial v} & \frac{\partial h(\mathbf{x},\alpha_i)}{\partial \omega} \end{bmatrix}. \tag{3.9}$$

$$\mathbf{H}_\alpha = \left[\frac{\partial h(\mathbf{x},\alpha_0)}{\partial \alpha_0}, \ldots, \frac{\partial h(\mathbf{x},\alpha_i)}{\partial \alpha_i}\right]^T. \tag{3.10}$$

3.2.3 Validation on Simulation

To validate the working principle of the presented filter we ran experiments on simulated data. Using Matlab Driving Scenario, data were generated to obtain sets of radar points and the position of a vehicle along a trajectory, as illustrated in Figure 3.2. The Kalman filter state estimation was tested in both single-radar and multi-radar cases. The results of these tests are shown in Figures 3.3 and 3.4.

The mean error (RMSE) between the estimated trajectory and the true trajectory is $0.41m$ and $0.33m$ for the single and multi-radar trajectories, respectively. Since, we have more information with two radars, it was expected to get a better RMSE. These tests validate our algorithm in a simulation context where both the

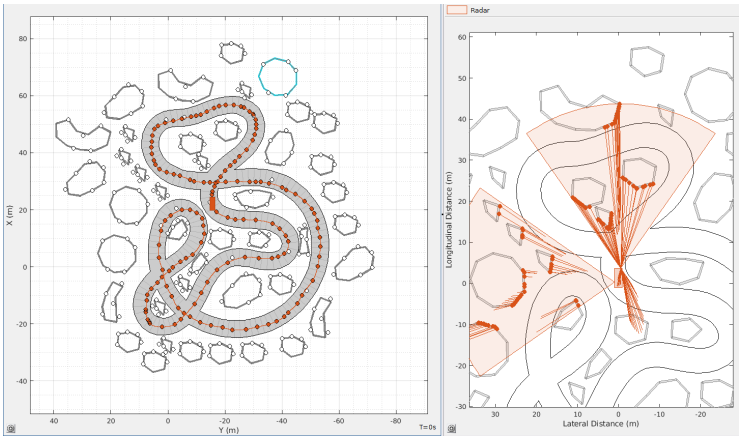

Figure 3.2: Matlab Driving Scenario simulator. Left: environment definition. Right: Simulated radar measurements

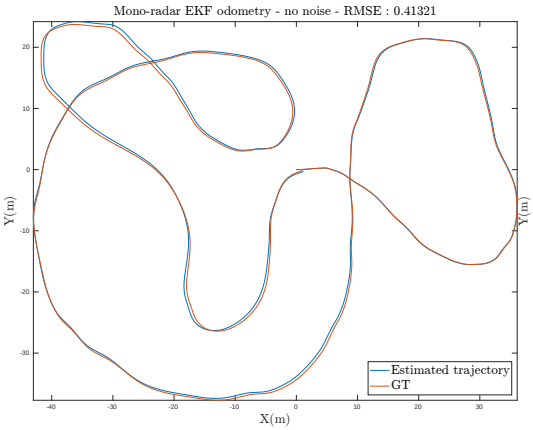

Figure 3.3: EKF estimation and ground truth - Single radar case

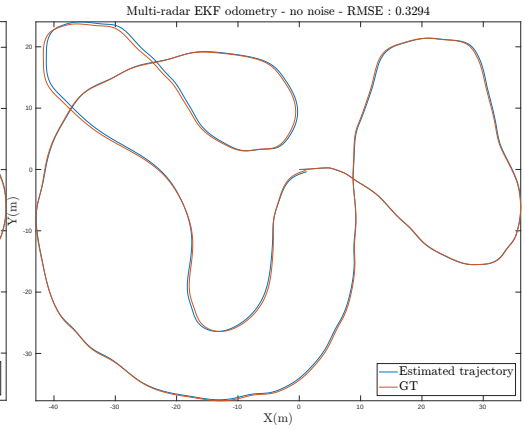

Figure 3.4: EKF estimation and ground truth - Multi-radar case

ground-truth calibration and the noise statistics are known. The remaining errors can be accounted to the sampling and CTRV integration of the trajectory since we do not have access to the motion model of the Matlab simulator. To validate our single-scan odometry on real world data, we first need to estimate the extrinsic calibration of the radars on the platform.

3.2.4 Radar Calibration

The extrinsic calibration corresponds to the ability to estimate a transformation between two frames for example, between two sensor frames or between a sensor frame and a vehicle reference frame.

3.2.4.1 State of the art in radar Calibration

In terms of radar calibration, several works were presented relying on the use of reflective corners that are convenient for data association through consecutive scans coming from one radar or between multiple sensors [Ubezio 2023, Wise 2023, Grebner 2022a]. Recently, target-less methods have been presented, facilitating the calibration process. Doer *et al.* [Doer 2020b] included in their radar-inertial odometry an online estimation of the 3D radar-IMU extrinsic parameters. Chen *et al.* [Cheng 2023a], proposed a 2D calibration of radar pairs, relying on a batch optimization of the fusion of estimated velocities by each radar and estimates the translation up to the scale and the rotation between two radars. Chen *et al.* [Chen 2024a, Chen 2024d] presented a spatiotemporal 3D targetless calibrator estimating the 3D extrinsic parameters between one or multiple exteroceptive sensors (camera, lidar, radar) and at least one IMU.

Many of the existing methods are dedicated to IMU-radar calibration. In this section, we propose a radar-only approach. The objective is to estimate the multi-radars to vehicle extrinsic calibrations.

3.2.4.2 2D Radar-Vehicle Calibration

We propose a targetless 2D radar-vehicle calibration, filter-based and dedicated to skid-steering vehicles. We will start by describing the measurement model, then we will derive an observability analysis dedicated to estimate an optimal radar mounting configuration.

Measurement Model and Estimation Feasibility As a reminder, in equation 3.6, we gave the expected radial velocity of a detection depending on its angle of observation such as:

$$\begin{aligned}\hat{v_r}_{,ij} &= (v_x - \omega_z l_{y,i})\cos(\beta_i + \alpha_{ij}) + \omega_z l_{x,i}\sin(\beta_i + \alpha_{ij}) \\ &= (v_x - \omega_z l_{y,i})\cos(\phi_{i,j}) + \omega_z l_{x,i}\sin(\phi_{i,j}).\end{aligned}$$

If we want to estimate the calibration $\mathbf{C}_i = [l_{x,i}, l_{y,i}, \beta_i]$ of each radar i only by relying on its measurement, since we do not have access to another estimate of velocities $[v_x, \omega_z]$, we need to do a joint estimation. Unfortunately, a full joint velocity-calibration estimation would require $H_{\mathbf{O}}$ the Jacobian of the measurement model with respect to the considered observable $\mathbf{O} = [v_x, \omega_z, C_1, \ldots, C_n]$ to be full rank, but in our case $H_{\mathbf{O}}$ is rank deficient ($\det(H_{\mathbf{O}}) = 0$). The Jacobian is given in equation 3.11, the linear relations between its columns are given in equation 3.12 and 3.13.

$$H_{\mathbf{O}} = \begin{bmatrix} \frac{\partial \hat{\mathbf{V}}_{\mathbf{r,1}}}{\partial v} & \frac{\partial \hat{\mathbf{V}}_{\mathbf{r,1}}}{\partial \omega} & \frac{\partial \hat{\mathbf{V}}_{\mathbf{r,1}}}{\partial C_1} & \cdots & \mathbf{0} \\ \vdots & \vdots & \vdots & \ddots & \vdots \\ \frac{\partial \hat{\mathbf{V}}_{\mathbf{r,n}}}{\partial v} & \frac{\partial \hat{\mathbf{V}}_{\mathbf{r,n}}}{\partial \omega} & \mathbf{0} & \cdots & \frac{\partial \hat{\mathbf{V}}_{\mathbf{r,n}}}{\partial C_n} \end{bmatrix}. \tag{3.11}$$

$$
\begin{aligned}
\frac{\partial \hat{\mathbf{V}}_{\mathbf{r,i}}}{\partial v} &= cos(\phi_{\mathbf{i}}) \\
\frac{\partial \hat{\mathbf{V}}_{\mathbf{r,i}}}{\partial \omega} &= -l_{y,i}cos(\phi_{\mathbf{i}}) + l_{x,i}sin(\phi_{\mathbf{i}}) \\
\frac{\partial \hat{\mathbf{V}}_{\mathbf{r,i}}}{\partial l_{x,i}} &= \omega sin(\phi_{\mathbf{i}}) \\
\frac{\partial \hat{\mathbf{V}}_{\mathbf{r,i}}}{\partial l_{y,i}} &= -\omega cos(\phi_{\mathbf{i}}) \\
\frac{\partial \hat{\mathbf{V}}_{\mathbf{r,i}}}{\partial \beta_i} &= -(v - \omega l_{y,i})sin(\phi_{\mathbf{i}}) + \omega l_{x,i}cos(\phi_{\mathbf{i}}).
\end{aligned}
$$

$$
\omega \frac{\partial \hat{\mathbf{V}}_{\mathbf{r}}}{\partial w} = \textstyle\sum_i l_{x,i} \frac{\partial \hat{\mathbf{V}}_{\mathbf{r,i}}}{\partial l_{x,i}} + l_{y,i} \frac{\partial \hat{\mathbf{V}}_{\mathbf{r,i}}}{\partial l_{y,i}}. \tag{3.12}
$$

$$
-\omega \frac{\partial \hat{\mathbf{V}}_{\mathbf{r}}}{\partial v} = \textstyle\sum_i \frac{\partial \hat{\mathbf{V}}_{\mathbf{r}}}{\partial l_{y,i}}. \tag{3.13}
$$

Because of these relations, the influence of variations on v, ω and $l_{x,i}$ $l_{y,i}$ are ambiguous and cannot be isolated. It is important to notice also that, while the odometry can be performed in the mono- or multi-radar case, the calibration cannot be done considering only one radar (detailed in next paragraph). Therefore, we will consider the multi-radar-vehicle calibration problem. We will describe in the two next paragraphs the proposed procedure to estimate the calibrations by avoiding the non-observable cases. To do so, we need first to estimate the sensors' orientations and secondly the sensors' positions.

Estimation of sensors orientations As said previously, we cannot perform a mono-radar calibration since $H_{\mathbf{O}}$ the Jacobian of the observation model with respect to $\mathbf{O} = [v, \omega, \beta]$ admit a rank deficiency due to the relation given in equation 3.14.

$$
-l_x \frac{\partial \hat{\mathbf{V}}_{\mathbf{r}}}{\partial \beta} + (v - \omega l_y) \frac{\partial \hat{\mathbf{V}}_{\mathbf{r}}}{\partial \omega} = (\omega(l_x^2 - l_y^2) - v l_y) \frac{\partial \hat{\mathbf{V}}_{\mathbf{r}}}{\partial v} \quad \text{Mono-radar case.} \tag{3.14}
$$

Then, using at least two radars, $H_{\mathbf{O}}$ is of full column rank, which makes it possible to estimate the extrinsic angle of the radars. For this first step, the radars' positions are initially unknown but required. Fortunately, the method is effective even with minimal prior knowledge, such as random positions in the appropriated vehicle's XY plane quadrants.

Estimation of the radars' lever-arms First, the rank deficiency due to equation (3.12) introduces a scale ambiguity, we propose to use two radars with a known inter-distance in a sensor bench configuration. By knowing the baseline $b = \sqrt{(l_{x,1} - l_{x,2})^2 + (l_{y,1} - l_{y,2})^2}$, we can add it as a measurement to our observation model, we then have $H_{\mathbf{O}}$ as written in equation 3.15:

$$
H_{\mathbf{O}} = \begin{bmatrix}
\frac{\partial \hat{\mathbf{V}}_{\mathbf{r}}}{\partial v} & \frac{\partial \hat{\mathbf{V}}_{\mathbf{r}}}{\partial \omega} & \frac{\partial \hat{\mathbf{V}}_{\mathbf{r}}}{\partial l_{x,1}} & \frac{\partial \hat{\mathbf{V}}_{\mathbf{r}}}{\partial l_{y,1}} & \frac{\partial \hat{\mathbf{V}}_{\mathbf{r}}}{\partial l_{x,2}} & \frac{\partial \hat{\mathbf{V}}_{\mathbf{r}}}{\partial l_{y,2}} \\
0 & 0 & \frac{\partial b}{\partial l_{x,1}} & \frac{\partial b}{\partial l_{x,2}} & \frac{\partial b}{\partial l_{x,2}} & \frac{\partial b}{\partial l_{y,2}}
\end{bmatrix}. \tag{3.15}
$$

Notice that the calibration estimation can be done up to the scale as illustrated in figure 3.5, which is the result of a Monte Carlo experiment where the calibration procedure as been tested through 100 runs with two radars without baseline knowledge and gave well estimated up to the scale lever-arms.

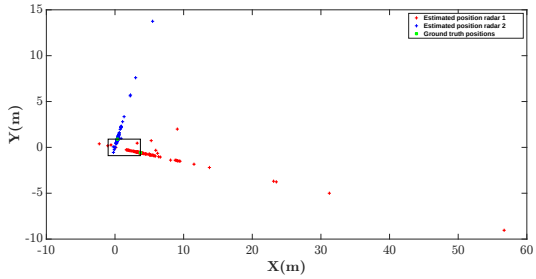

Figure 3.5: Position estimation of two radars - 100 runs

Secondly, even with the described configuration, the equation 3.13 still remains true. To solve that issue, since we use a skid-steering rover, it can execute a pure rotational trajectory. Then, we have $v = 0$, and the following state vector: $x_k = [\theta, \omega, l_{x,1}, l_{y,1}, l_{x,2}, l_{y,2}]$ with Jacobian of the measurement model with respect to $[\omega, l_{x,1}, l_{y,1}, l_{x,2}, l_{y,2}]$ which is now in full column rank.

We presented the proposed two-step calibration procedure. Following this, since we did an observability analysis to check the feasibility of the estimation, we thought of extending it to maximise the observability of our estimator by using an optimal sensor placement.

3.2.4.3 Observability Analysis For Optimal Sensor Placement

To mount two radar systems on a vehicle, it is of main concern to have a good sensor placement. To find the best sensor poses, the method presented in [Corominas-Murtra 2016] is used. The observability of the state vector is evaluated thanks to the determinant of the information matrix. The higher the value of such a determinant, the better the configuration. On the other hand, a null value, indicate a non-observable placement. The information matrix $\mathcal{I}$ can be computed with equation 3.16:

$$\begin{aligned} \mathcal{I} = &\ H_{\mathbf{O}}^T R H_{\mathbf{O}} \\ = &\ H_{\mathbf{O}}^T (R_{v_r} + H_\alpha R_\alpha H_\alpha^T) H_{\mathbf{O}}. \end{aligned} \tag{3.16}$$

with $H_{\mathbf{O}}, H_\alpha$ respectively the Jacobians of the measurement model with respect to the considered observables and to the azimuth angle of each detection and R_{v_r}, R_α respectively the covariance matrices of the radial velocity and azimuth angle measurements.

3.2.4.4 Experimental setup and results

To estimate the optimal sensor placement, we will compute $|\mathcal{I}|$, the determinant of the information matrix, for each possible radar pose. For this theoretical study, we consider that each radar admits detections that are uniformly distributed in their field of view (FOV) and that each radar is placed around the vehicle as depicted in figure 3.6. The mounting poses are indexed in the interval $[0, 8[$.

The results of observability analysis are shown in figure 3.7.

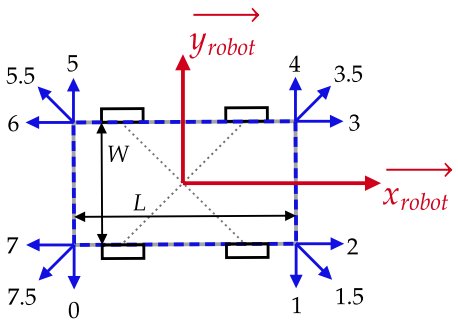

Figure 3.6: Mounting poses indexing

Each plots are the results of the computation of $|\mathcal{I}|$ at each pose for one radar (a) and two radar (b,c,d). Plots (a,b) correspond to the observability of $[v, \omega]$ with the knowledge of the extrinsic calibration. In plot (c), the considered observables are $[v, \omega, \beta_1, \beta_2]$. Finally, plot (d), shows the observability in the zero velocity scenario estimating $[\omega, l_{x_1} l_{y_1}, l_{x_2}, l_{y_2}]$ having the knowledge of the baseline and the extrinsic angles. We computed $|\mathcal{I}|$ with several values of ω centered on 0 and kept the minimum value to take into account the vehicle's motion. For plots (a,b,c), we used $V_x = 1.5m/s$ and $\omega \in \{-0.3, 0, 0.3\}$ and the same for (d) except that $\omega = 0$.

Since in plot (d), a lot of cells are equal to zero, meaning non-observable configurations, and that the accuracy of calibration has an impact on the accuracy of motion estimation, we propose a final metric for observability which corresponds to the element-wise multiplication of plot (b), (c) and (d). By doing this, we will first avoid the configurations where calibration cannot be performed and find the sensor placement that provides the optimal trade-off between motion estimation and calibration. The result of this metric is given in figure 3.8 and the resulting optimal sensor placements pairs are depicted in figure 3.9.

3.2.4.5 Validation of Calibration via Simulation

Calibration Simulations were conducted again on Matlab Driving Scenario to generate sensor data, follow the proposed procedure and compare the results against a ground-truth. The proposed experimentation of the calibration consists first by doing an unknown trajectory with noised extrinsic parameters on the lever-arm: $\sigma_{l_{x,y}} = 0.2$ m, and on the extrinsic angles β with two different level of noise: $\sigma_{high} = 20\,\text{deg}$ and $\sigma_{low} = 5\,\text{deg}$ and estimate the orientation of both radars. Then, to calibrate the lever-arm of the radars w.r.t the vehicle reference frame, for this second step we use the estimated radars orientations and the same noise on the radars' positions, and we perform a pure rotational trajectory. We performed 100 runs to compute Root-Mean Square Error (RMSE) of the estimated variables. The results obtained are depicted in table 3.17.

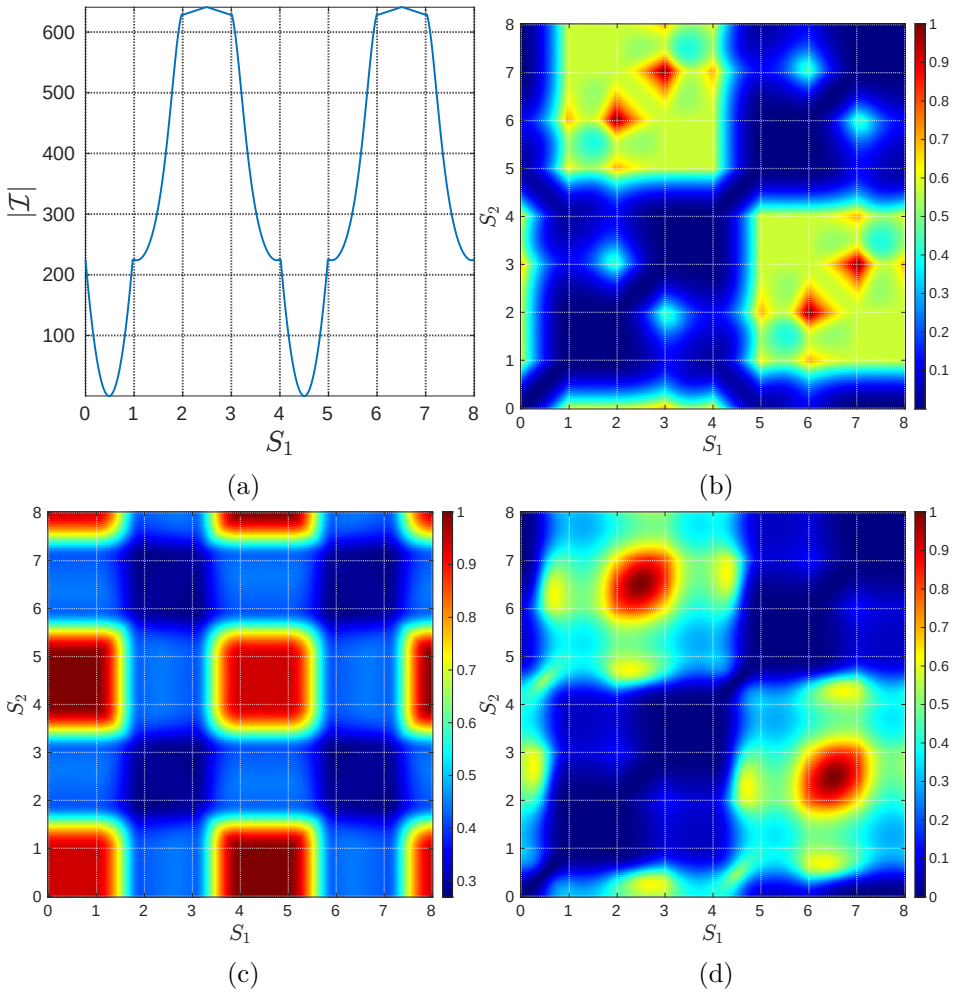

Figure 3.7: Values of $|\mathcal{I}|$ are depicted on y-axis of plot (a) and with color on others. x-axis represents poses of sensor 1 (S_1). On plots (b),(c) and (d) poses of sensor 2 (S_2) are on y-axis. Plots (a) and (b) corresponds to velocity estimation for mono- and multi-radar. Plots (c) and (d) represents respectively the observability of orientation and lever-arm estimation

	Orientation	Position
	$[\beta_1, \beta_2](deg)$	$[l_{x,1} l_{y,1}, l_{x,2}, l_{y,2}](m)$
RMSE σ_{high}	$[2.26, 2.33]$	$[9.4, 14.4, 9.5, 14.3] \times 10^{-3}$
RMSE σ_{low}	$[1.38, 1.12]$	$[8.5, 9.2, 7.8, 7.7] \times 10^{-3}$

(3.17)

Note that in both noise case, we obtain a calibration accuracy that is better than the direction of arrival accuracy of the sensor ($< 3\,\text{deg}$) even considering a poor initial lever-arm knowledge. The RMSE obtained on the position is at least one order of magnitude lower than the initial noise level and generally less than a centimeter which is a more than decent result.

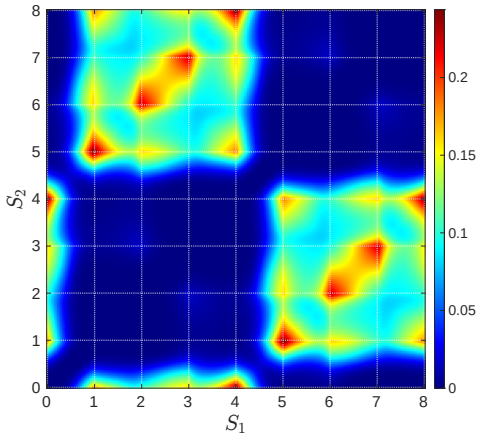

Figure 3.8: Minimums of observability by element-wise multiplication

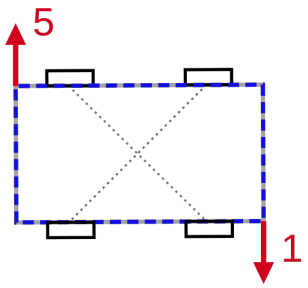

Figure 3.9: Optimal sensor placements poses pair

Odometry To test the efficiency of the calibration procedure, we will present odometry results first using the ground truth calibration and then using the estimated calibration. We computed Relative Pose Error (RPE) and Absolute Pose Error (APE) between the ground truth poses and the one estimated by the odometry in both cases. For the odometry with estimated calibration, we performed 100 runs over a 140m trajectory with a noise level on the extrinsic parameters corresponding to the RMSEs detailed previously, therefore, the results are the mean RPE and APE over 100 runs.

Odom	w/ GT calib	w/ est. calib σ_h	w/ est. calib σ_l
	$trans(m), rot(deg)$	$t(m), r(deg)$	$t(m), r(deg)$
RPE	$[1.08, 0.15] \times 10^{-2}$	$[0.23, 0.31]$	$[0.21, 0.31]$
APE	$[1.08, 0.07]$	$[12.11, 16.37]$	$[7.31, 16.7]$

In simulation, the odometry and the proposed calibration have shown promising results considering both the noise level on the extrinsic parameters and the accuracy of the radar used. Notice that to replicate the real rover, the level of motion excitation set is quite low and the size of the simulated vehicle correspond to the real one. By doing this, the gap between simulation and real data experiments is smaller. Nevertheless, a higher level of motion excitation would be better for two reasons: there will be a better SNR on the radial velocities and the influence of translation and rotation on the Doppler could be less ambiguous. This last point is also true with a higher baseline between the two radars which would be the case with a car-like vehicle.

3.2.5 Validation of Calibration and Odometry on Real Data

Calibration The proposed experimentation of the calibration consists first by doing an unknown trajectory with rough estimate of the radars' position and estimate the orientation of both radars. Then, to calibrate the lever-arm of the radars with respect to the vehicle frame, for this second step we use the estimated radars orientations, and we perform a pure rotational trajectory. We tested the calibration with two radars, a TI AWR1843 and a TI AWR1843AOP, both mounted on our rover as depicted in figure 3.10.

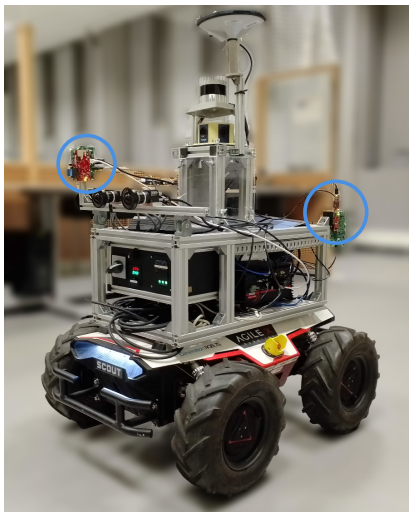

Figure 3.10: Instrumented rover used for single-scan odometry

The configurations used for both radars correspond to $\alpha_{res,1843} = 15\,\text{deg}$, $\alpha_{res,1843AOP} = 30\,\text{deg}$, $Vr_{res} = 0.08m/s$. The frame frequency was 20 Hz. For the update, the measurement noise is based on the theoretical resolution of the sensor and the Signal to Noise Ratio (SNR) of the target, using $\sigma_x = x_{res}/\sqrt{SNR}$ [Dell 1963] with $x \in \{\alpha, Vr\}$.

The radar mounting poses correspond to the configuration $[2, 5]$ shown in figure 3.6 and 3.10.

The a priori calibration has been set, for the extrinsic angle estimation, to $C_1 = C_2 = [0, 0, 0]$, and for the position estimation, to $[l_x, l_y]_1 = [0.1, -0.1]$ and $[l_x, l_y]_2 = [-0.1, 0.1]$. The initial standard deviation of the calibration was defined as $10\,\text{deg}$ and $0.1m$ for the angle and position. The outlier rejection used consists in a χ^2 test on the Mahalanobis distance associated to each target. The results of the angle and position calibration are depicted in figure 3.11 and 3.12 respectively.

We can see that the estimation of extrinsic parameters converges rapidly to relevant values considering the mounting poses. We ran angle calibration on several datasets and it always converged around these angles. The translation estimate depends on the defined baseline, but also converges to positions in line with the configuration.

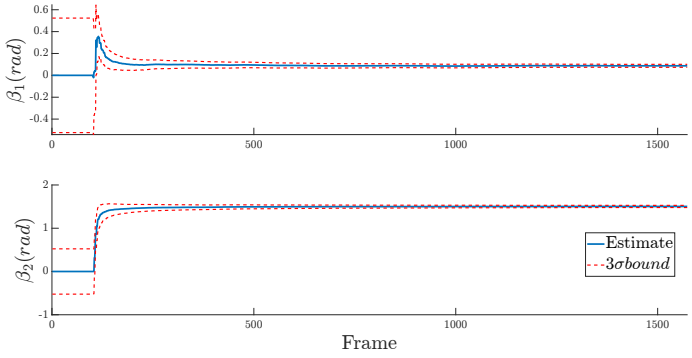

Figure 3.11: Estimated extrinsic angles

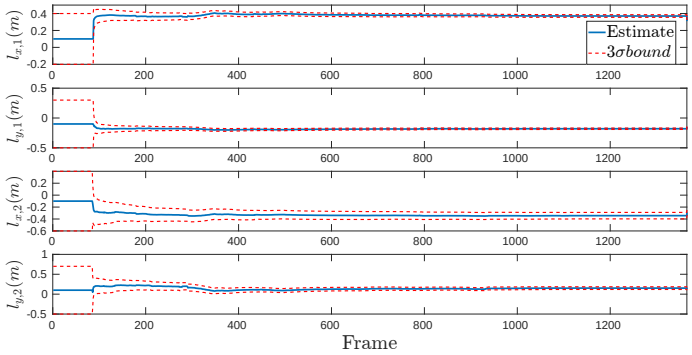

Figure 3.12: Estimated extrinsic positions

Odometry The final tests of the IEKF based single-scan odometry and calibration has been done using the same setup and the estimated calibration as presented in the previous paragraph. The results of the trajectory estimation and velocimetry from two trajectories are shown in figure 3.13. From these we can say that the translation is well estimated as the linear velocity has a stable low error while the angular velocity admits a notable error resulting in a drift compared to the ground-truth trajectory. The main issue from single-scan odometry using a rover, compared to a car, is the relatively small baseline between the sensors making the rotation estimation worst. Also, since we use the calibration from the IEKF estimation, and that we do not have a ground-truth calibration, we cannot determine if the error arises from odometry or calibration, making error accounting a non-trivial issue. Finally, we used non-triggered radars which is also source of error since we rely on the inter-scan delay computed from the ROS timestamp.

3.2.6 Conclusion

In the previous sections, we first addressed mono- and multi-radar single-scan odometry using an Implicit Extended Kalman Filter, built on Doppler-based ego-velocity estimation principle. We then proposed a filter-based, target-less extrinsic multi-radar vehicles calibration method. We provided an observability analysis to determine optimal sensor positioning accounting for both velocimetry estimability and

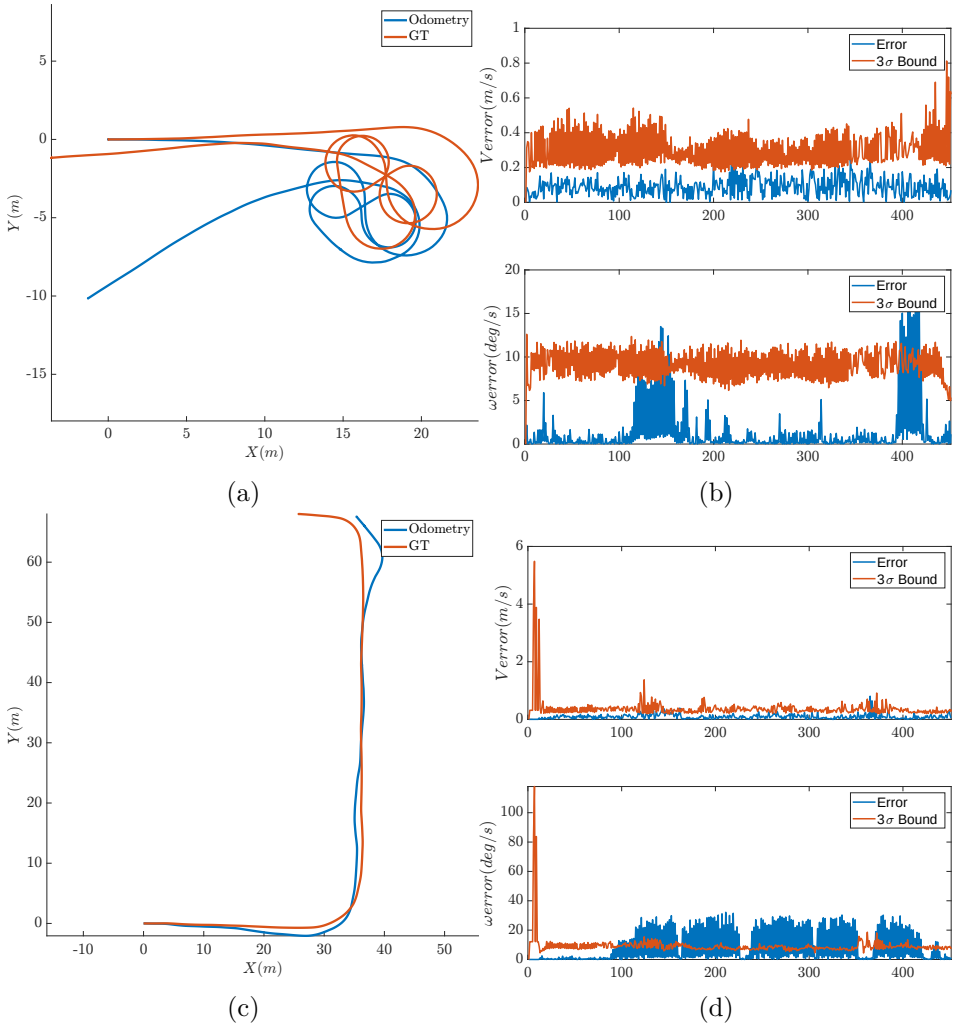

Figure 3.13: Results of the IEKF based single-scan odometry obtained with 2 radars

calibrability. Finally, we proposed a validation of the presented work through both simulation and real world experiments achieving adequate lever-arm estimation and decent odometry results. This work has been published is [Tyack 2025]. We have seen that the translation estimation is accurate and stable. Nevertheless, the difficulty using a rover lies in the small achievable lever-arms, making the estimation of the rotation a challenging task if relying only on single-scan odometry. Another difficulty related to the tight-coupled embedded in an Kalman filter is that the weighting of the covariance is complex. As said in section 2.3, the sources of noise and outlier in radar are not trivial making the tuning of the filter quite hard and/or non robust.

The main issue of the presented odometry is the poor estimation of the rotation. Since we only used Doppler and angle informations for this strategy, we proposed calculating this rotation using range and angle informations using a scan-to-scan approach.

3.3 Scan-to-Scan estimation

Scan-to-scan estimation in radar-based systems typically relies on either point cloud alignment or image registration. Point cloud alignment, often addressed using Iterative Closest Point (ICP), is challenging using radar data due to sparsity, noise, and outliers. Unlike lidar, radar point clouds suffer from lower detection repeatability, making correspondence between successive scans unreliable, especially in environments with few strong scatterers. Additionally, extracting a point cloud is a prerequisite. Alternatively, raw radar data provides dense (though noisy) information that remains consistent across scans. Registration can be achieved through dense methods or feature-based ones. Dense methods avoid the need for explicit association, while feature-based approaches simplify matching via descriptor similarity. Moreover, images used for registration may also serve as inputs for dense mapping tasks.

This section will focus on Raw data based odometry. This kind of odometry rely on the matching between successive scans. In radar, a scan can be represented as a range-azimuth map. We will first detail the beamforming-based method to get these maps. Then, the type of registration of such scans will be given. Finally, we will explicit the rotation estimation employed and results obtained.

3.3.1 Scan Formation

We will detail how from a set of range-focused measurement obtained from an array of antenna, we can use beamforming techniques to get a range-azimuth map.

Beamforming Beamforming is a signal processing technique used with data obtained by sensor arrays to estimate the direction of arrival of the backscatter signal among a chosen span of tested angles θ_k. It exists numerous beamformers [Krim 1996] often classified by type of methods (spectral, parametric), the resolution capability, the computational cost, etc.. The most classic beamformer corresponds to that of Bartlett, but we have chosen to use Capon's because it offers better performance in terms of resolution at the cost of a reasonable increase in computational cost. Compared to some other methods, it does not require prior knowledge of the number of scatterers.

First, we will detail the theoretical concepts shared by many beamformers. From equation 2.21, we can write the range focused set of measurements $\mathbf{x} \in \mathbb{C}^{N_a}$ at output of the antenna array such as:

$$\mathbf{x} = s_{re}(0)[1, e^{-j\frac{2\pi}{\lambda}d\sin(\theta)}, \dots, e^{-j\frac{2\pi}{\lambda}d(N_a-1)\sin(\theta)}],$$

with θ the angle of arrival of the signal. Frequency domain beamforming use the so-called spatial covariance $R = \mathbb{E}[\mathbf{x}\mathbf{x}^T]$. When assuming a zero-mean Gaussian white noise, we can model R as:

$$R = \mathbf{V}S\mathbf{V}^H + \sigma^2 I, \tag{3.18}$$

with σ, I and S the variance of the noise, identity matrix and the source covariance matrix respectively. The array manifold vector $\mathbf{V} = [\mathbf{a}(\theta_0), \ldots, \mathbf{a}(\theta_k)]$, and $\mathbf{a}(\theta) = [1, e^{j\frac{2\pi}{\lambda}d\sin(\theta)}, \ldots, e^{j\frac{2\pi}{\lambda}d(N-1)\sin(\theta)}]^T$ a steering vector in direction θ.

The capon beamformer The Capon [Capon 1969] beamformer attempts to minimize the power received from both noise and any signals coming from other directions than θ, while maintaining a fixed gain in θ's direction. From these constraints it is also called Minimum Variance Distortionless Response (MVDR) beamformer and it is formulated such as:

$$\begin{aligned} R &= \mathbb{E}[\mathbf{x}\mathbf{x}^T] \\ \mathbf{w}_{Capon}(\theta) &= \frac{R^{-1}\mathbf{a}(\theta)}{\mathbf{a}^H(\theta)R^{-1}\mathbf{a}(\theta)} \\ P_{Capon}(\theta) &= \frac{1}{\mathbf{a}(\theta)^H R^{-1}\mathbf{a}(\theta)}. \end{aligned} \tag{3.19}$$

The advantage of the Capon beamformer lies in the significantly higher resolution compared to the DFT beamformer.

Range-azimuth map creation We have seen how to estimate the level of interference between a set of measurement from an array and its expectation over an angular span. Then, from a range-focused data cube, by doing this for each range bin, we can map these level of interferences over a polar coordinate grid, the so-called range-azimuth map (RA map). It will correspond to a spatial repartition of the probable scatterers in the field of view of the radar. An example of such map in its original form and interpolated into a Cartesian grid is given in figure 3.14.

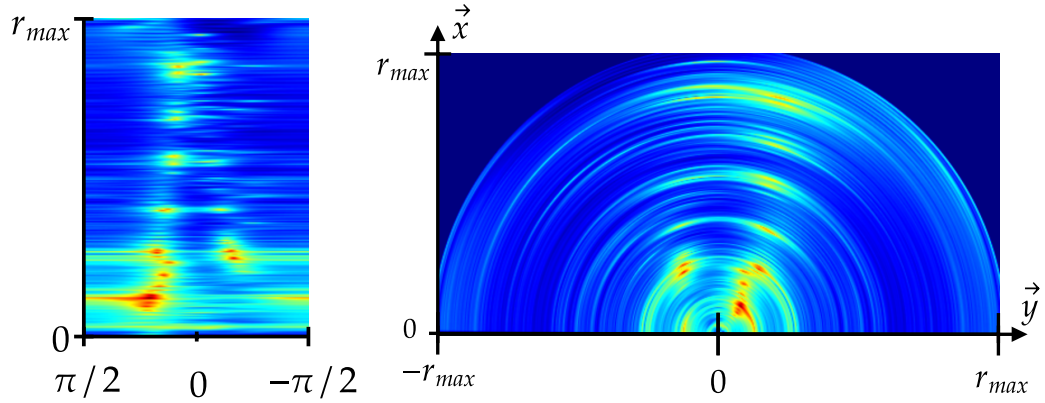

(a) (b)

Figure 3.14: RA map a) in polar coordinates and b) transformed in Cartesian coordinates

Note that, because we are working with a MIMO radar mounted on a moving

platform, we have to take into account the phase-errors existing between signals from different sub-arrays due to the motion. For more information on the issue of motion-compensation due to Time Domain Modulation MIMO array, one can refers to Annex A.1.

3.3.1.1 Feature Detection And Association

To align two or more radar images taken at different times, it exist two main kind of approaches: dense and feature-based.

The first has been used extensively with rotating radars [Burnett 2021, Adolfsson 2022, Hong 2020]. Dense methods have the benefit of avoiding the need for explicit association by doing a full image to image registration. However, they are well suited for such radars since they work best using wide FOV sensors ($> 180°$) and works best with finely resolved images. However, radar scans are prone to speckle, multipath and saturations that can affect strongly dense based methods [Barnes 2020]. To overcome this, masking can be employed but it is a challenging task [Adolfsson 2021].

The second approach using feature-based matching has been employed on OGM based matching and for loop closure [Holder 2019, Grebner 2024]. Feature-based method can admit outliers due to speckle or other effects but diverse rejection approaches can be used [Adolfsson 2021, Hong 2020] to tackle this issue. Nevertheless, in low-backscatter regions such as fields, it is hard to find reliable features. Finally feature based methods have been applied within a wide range of applications and numerous algorithms are implemented in a highly optimized way in OpenCV.

In our application we opt for feature-based solution to align our range-azimuth images. To do this matching different steps are required: the detection of accurate and robust features, the choice of a matching approach and the transformation estimation.

Feature There are numerous feature detectors available [Li 2015]. In this study we opted for Accelerated KAZE (AKAZE) features [Alcantarilla 2012, Alcantarilla 2013]. The efficiency of KAZE features has been proven in multiple works [Grebner 2024, Holder 2019, Demchev 2017, Pourfard 2022]. The reason of this choice is linked to the nature of the images. The features to be detected are closer to blobs than edges or corners. A blob is defined as a region where pixels are similar to each other but distinct from their surrounding neighbourhoods. Nonlinear diffusion filtering, as used in KAZE, preserves shapes, unlike detectors based on partial differentiation in Gaussian scale spaces (e.g., SURF, SIFT), which tend to blur the image. In our solution we selected the accelerated version of KAZE it benefits from an OpenCV implementation. This feature detector is associated to its specific descriptor the Modified-Local Difference Binary (M-LDB) which is rotation and scale invariant. It exploits gradient and intensity informations from the nonlinear scale space. From this, we can obtain sets of detected features that we call keypoints, and their associated descriptor for each image.

Correspondence We need to identify possible correspondences between the detected keypoints of the two images. A brute-force matcher is employed, meaning that the descriptor of one feature in first set is tested with all other features in second set using a distance calculation, and the closest one is returned. Since we use a binary descriptor, we can efficiently perform the distance computation using Hamming distance. An example of obtained matches between two consecutive RA maps is given in figure 3.15.

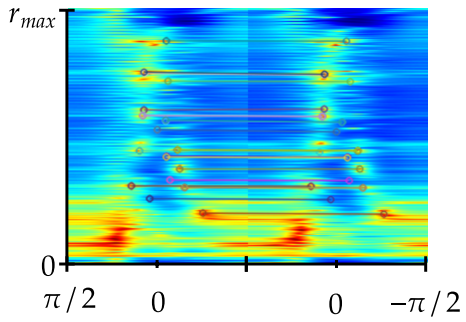

Figure 3.15: Two consecutive RA map and correspondences pairs between detected features

Transformation Estimation Once feature correspondences have been established, the next step is to estimate the geometric transformation between the two RA maps. Each match links a point p_i extracted from the previous image to a point q_i extracted from the current one. Since keypoints are expressed in image coordinates, we first compute polar coordinates, then they are projected into a 2D Cartesian frame. We then have two sets of matches of 2D points $\{p_i\}$ and $\{q_i\}$.

In our application, the relative translation between consecutive RA maps assumed to be known thanks to Doppler angle velocity integration. For this reason, we estimate only the 2D rotation R, using the Kabsch algorithm [Kabsch 1976]. Then, this rotation matrix needs to minimize:

$$\sum_i \|q_i - Rp_i\|^2.$$

To perform Kabsch algorithm, usually, centroids of both set of points is computed and subtracted to the points to translate both sets at the origin frame. In our case, the translation is set according to the one obtained from Doppler-Angle Regression (DAR) and subtracted to $\{p_i\}$ giving $\{p'_i\}$. Then, we compute the cross-covariance

matrix and we obtain the rotation with a Singular Value Decomposition:

$$\begin{aligned} S &= \sum_i p'_i q_i^T \\ S &= U\Sigma V^T \\ R &= VU^T. \end{aligned} \tag{3.20}$$

RANSAC-based rotation estimation Radar data may contain spurious matches due to noisy detections or ambiguous reflections. To ensure robustness, we embed the Kabsch rotation estimation inside a RANSAC loop. Following the steps at each iteration:

1. Randomly sample a minimal set of correspondences (two pairs in 2D).
2. Compute a candidate rotation matrix R_{hyp} with the Kabsch algorithm.
3. For all correspondences, evaluate the alignment error

$$e_i = \|q_i - R_{\text{hyp}} p_i\|.$$

4. Count inliers using a predefined tolerance.

The rotation hypothesis with the highest inlier count is selected, and the final rotation matrix is recomputed using all inliers. This robust scan-to-scan rotation estimation is then inserted into the radar odometry pipeline to update the frame-to-world transformation.

3.3.2 Results with Real data

We tested the proposed algorithm using real data recorded with a 77GHz MIMO radar and the pipeline has been implemented in C++ relying on SaDVIO's [Debeunne 2024] code, especially for feature and landmark management. In Figure 3.16a, the aligned estimated trajectory and the ground-truth one are shown. So far, the state estimation results obtained are not good enough at this stage to hope, for example, to perform SAR mapping. Nevertheless, we think that the proposed method has potential for SLAM applications. Indeed, the Figure 3.16b shows histograms of number of associated features to a landmark using Kanade-Lucas-Tomasi [Lucas 1981] feature tracking and feature matching. We can see that with both methods, first, more than half of the landmarks admit 3 or more features associated, secondly, some landmark reaches high number of associated features. Also, we noticed that the KLT based pipeline admit higher estimation errors but may performs better within a SLAM pipeline since it generally admit a higher number of associated feature per landmark.

Finally, the trajectory estimation solution retained that will be used for SAR mapping on non-linear trajectories corresponds to a pointcloud scan-matching one. It relies on Doppler-Angle Regression using RANSAC for translation estimation and pointcloud filtering and for the 2D rotation estimation we use the KISS-ICP [Vizzo 2023] pipeline with the filtered pointcloud and DAR estimated translation

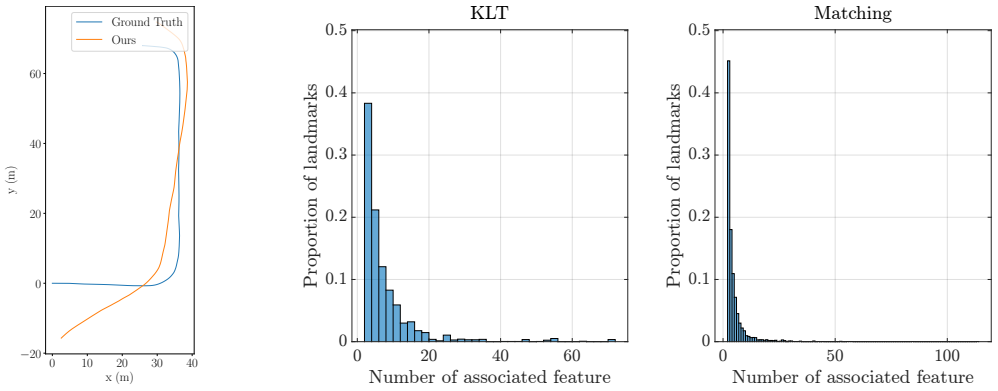

(a) (b)

Figure 3.16: a) Estimated trajectory from range-azimuth scan-matching and DAR. b) Histograms of number of associated features to a landmark using KLT feature tracking (left) and feature matching (right)

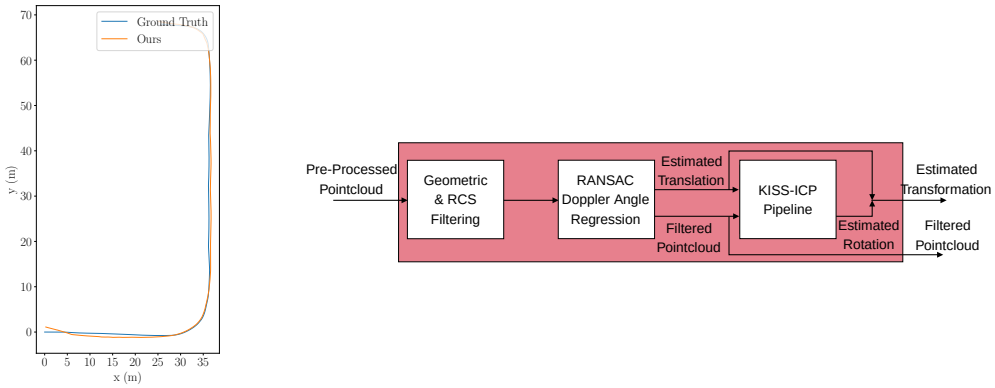

(a) (b)

Figure 3.17: a) Estimated trajectory from KISS-ICP and DAR b) Pointcloud based kept trajectory estimation solution

as inputs. The trajectory estimation result is shown in Figure 3.17a, the pipeline is illustrated in Figure 3.17b.

In this section, we presented the proposed raw-data feature-based scan-to-scan estimation relying on range azimuth maps.

3.4 Conclusion And Perspectives

This chapter focused on radar based localisation, its stakes, the state-of-the-art and our contributions on that topic. First, the single-scan pointcloud-based estimation has been detailed and we presented the simulation results of a 2D EKF-based odometry. The requirements for an optimal 2D multi-radar-vehicle calibration has been explained and the validation of the multi-radar odometry and calibration has been

done using real data. After that, we detailed the first results of a scan-to-scan raw-data based estimation. We demonstrated the ability to track landmarks along a trajectory using range-azimuth maps and detailed its potential applications within a SLAM framework. Finally, we explained the chosen localisation solution relying on pointcloud based Doppler-Angle regression and ICP. This solution and the work done on range-azimuth map feature matching are part of the localisation and mapping library developed during this thesis shown in Appendix C.

There are numerous state estimation problems to extend these contributions.

First, the calibration could be extended using range and RCS information of the targets. We could consider static radar measurements and moving target tracking.

Spatial Calibration It could be interesting to develop the calibration's observability study with the addition of scan-to-scan techniques such as ICP. By doing this, we could see the impact on calibration requirements and on optimal sensor placement. There may be several ways to tackle this problem, at least we could consider trajectory alignment and map alignment. The second one may improve observability requirements at the cost of a harder feasibility due to inter-radar landmark matching especially with a non-overlapping field-of-view setup. Would this additional information be sufficient for 3D calibration?

Temporal Calibration A non-triggered radar is providing a stamp that admits a time bias that limits its performance. Since works have presented for spatio-temporal calibration of radar-IMU [Chen 2024b, Chen 2024d], radar-camera [Wise 2023], radar-lidar [Lee 2020] setups, radar-radar temporal calibration should be studied. The avenues of research are velocity alignment [Chen 2024d] and RCS- and FOV-based map alignment [Lee 2020]. Also, when considering mixed data, pointcloud and raw data messages admit different stamps. A robust association method should be considered or time alignment.

Localisation Considering scan-to-scan estimation, since recently the ICP based method have shown promising results [Kubelka 2023], especially Doppler-ICP [Herraez 2024], Ground-ICP [Herraez 2025], and RCS-weighted ICP [Kim 2024b] all combined with diverse filtering strategies, it could be interesting to extensively study these techniques within different scenarios, individually or combined, to benchmark all these methods.

Then, the extension of the presented works within a SLAM framework appears necessary to increase the robustness and performances of the localisation and mapping. Regarding raw-data based estimation, we have seen that the range azimuth map feature-based matching has a room for improvement using sliding window optimization. Also, one of the most appealing perspective considering raw-data based localisation and mapping optimization is to study autofocus based methods (detailed in Chapter 4) in our context. For both pointcloud and raw-data based estimation, adding loop-closures techniques would be a key feature. An extensive study

would be required for both data types to judge which solution can be used, which lidar [Kim 2018, Yuan 2023a, Dubé 2019] or camera [Gálvez-López 2012] methods performs best using radar. Finally, in visual-inertial SLAM, two main architectures have proven to work robustly and with best performance : factor graph [Campos 2021] and Multi-State Constrained Extended Kalman Filter(MSCKF) [Geneva 2020]. It would be then the two targeted framework for SLAM extension of the proposed work, benchmarking them in the context of radar-only or radar-inertial SLAM would be valuable.

Chapter 4

Radar Mapping

Contents

4.1 Map representations 51
4.1.1 Sparse Landmark Map 52
4.1.2 Grid Map 53
4.2 Synthetic Aperture Radar 55
4.2.1 Motivations And Principle 55
4.2.2 Geometry 58
4.2.3 State Of The Art 60
4.2.4 Time Domain Back Projection 64
4.2.5 Performing SAR Imagery 65
4.3 Validation Steps 71
4.3.1 Rectilinear Trajectory 71
4.3.2 Non-Linear Trajectory 72
4.3.3 Processed Angular Aperture 76
4.3.4 SAR Vs Lidar 79
4.4 Conclusion 81

Mapping is a key feature, it corresponds to the perception of the robot's environment. It needs to be accurate to ensure safe and efficient path planning and also can be the main purpose of a mission in itself [Petracek 2024]. Radar-based mapping is interesting for redundancy and to increase the diversity of information since it is affected by its environment in a different way than a camera or a lidar. In this chapter, we will describe first a few concepts of mapping in robotics, and then describe one of the core work of this thesis: the use of Synthetic Aperture Radar in the context of UGV navigation. We will start with the concept and motivations of this technique, then detail the state of the art. Finally, we will present our contribution on robot-based SAR imaging. The chapter will be concluded by a discussion about SAR for ground-robots.

4.1 Map representations

It exists a lot of map representations in robotics: sparse map, dense map, topological map, semantic map... Over all of these representation, two representations

are well suited for radar data and are mainly used: sparse maps (composed of distinct object of interests called landmarks), and occupancy grids (representing a regular discretization of the 2D or 3D space). An illustration of those two mapping strategies is given in figure 4.1.

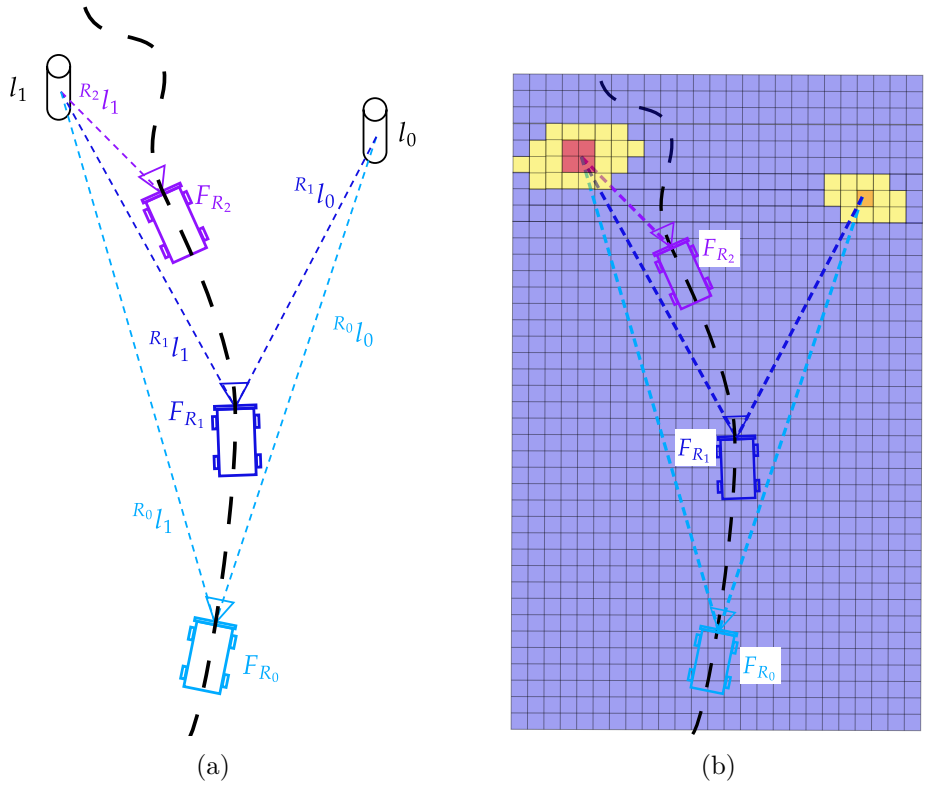

Figure 4.1: Mapping strategies: a) Landmark based, b) Grid based

4.1.1 Sparse Landmark Map

The sparse map is a collection of object of interest. Such a map is represented as a set of landmarks $\mathbf{l}_{0:L} = \{l_0, \ldots, l_L\}$ that have the specificity to be easily detected with high repeatability in the data. These detections are called *features*. A feature u corresponds typically to a high intensity gradient detected in a measurement z: a corner in an optical image or the response of a point scatterer in a radar range azimuth image.

During the robot motion, the detected features are tracked or matched in the successive sensor acquisitions. Then, if the feature has been tracked over enough data acquisitions (from iteration i to j), a landmark is created using the inverse of the observation model h^{-1} such as:

$$l_k = h^{-1}(\mathbf{x}_{i:j}, u_{i:j}).$$

If the feature tracked is already associated to a landmark, the current observa-

tion is added to the set of features $u_{i:j}$. As a consequence, the objective of sparse mapping is to maintain the best knowledge for $\mathbf{l}_{0:L}$:

$$p(\mathbf{l}_{0:L}|\mathbf{x}_{i:j}, u_{i:j}).$$

More generally, a filtering or optimization process can be done over a given horizon of robot pose to smooth the trajectory and correct the entire sparse map. Such process is called Simultaneous, Localization and Mapping (SLAM).

$$p(\mathbf{x}_{0:N}, \mathbf{l}_{0:L}|z_{0:N}).$$

4.1.2 Grid Map

A grid map corresponds to a dense cartography consisting in compressing the continuous 3D world as a 2D (or 3D) discrete representation [Moravec 1985]. This type of map can, generally, be generated both locally (from the current measurement) and globally (using all the measurements). The second case is often preferred for navigation since it will produce more reliable cartography but at the cost of the knowledge of the trajectory. The type of measurement for creating the maps shown in the following can be either a set of detections or dense data (i.e. range azimuth map).

4.1.2.1 Probabilistic Occupancy Grid Map

The Occupancy Grid Map (OGM) uses measurements, robot states and a sensor model to compute for each cell of the grid the occupancy probability such as:

$$L(m_k) = \log \frac{p(m_k|\mathbf{z_{0:k}}, \mathbf{x}_{0:k})}{1 - p(m_k|\mathbf{z_{0:k}}, \mathbf{x}_{0:k})}, \tag{4.1}$$

with $L(m_k)$ the log-odd representation of the posterior occupancy probability of cell m at time k (Note that the log-odd is preferred to avoid numerical instabilities). The term $p(m_k|\mathbf{z_{0:k}}, \mathbf{x}_{0:k})$ corresponds to the inverse sensor model and describes the influence of a measurement on the grid with respect to the characteristics of the sensor. One major difference of the radar sensor model is that cameras and lidar assume empty space between the sensor and a detection, while radar can detect non-line-of-sight objects (e.g., reflections or see-through).

4.1.2.2 Amplitude Grid Map

Another classical grid representation is the Amplitude Grid Mapping (AGM) method, it is faster to compute than an OGM, often at the cost of a coarser mapping. Here, each cell of the map will not be linked to a probability of occupancy as with an OGM but will represent the accumulated received power by the sensor along mapping. Each measurement will produce a local AGM that correspond to a Cartesian grid of the FOV of the sensor. Each cell of this grid is filled accordingly

to the power of the detected scatterers. Then, the global AGM is created iteratively by fusing each local AGM. The merge can be done in a various manner using whether a simple summation or via weighted-mean, median, etc.. The result is an efficient, simple, but rough representation of the environment.

When using radar, there is two main categories of mapping. First, as presented in many studies, the simple concatenation of filtered point clouds can be used as a map. This type of map is affiliated to sparse landmark mapping but, in the context of radar, it appears to be noisy as shown in the examples of Figure 4.2 and does not use all the capabilities of the radar data. As an alternative, other approaches make use of grid map representation. The objective is to reach a much higher resolution by forming a long synthetic aperture along the trajectory. We will first explain the motivations and the principle of such a technique. Then, we will detail the state-of-the-art on that subject. After that, the used algorithm will be described. Finally, validation through iterative experiments and comparison with lidar data are given. We will conclude with a discussion on the proposed strategy.

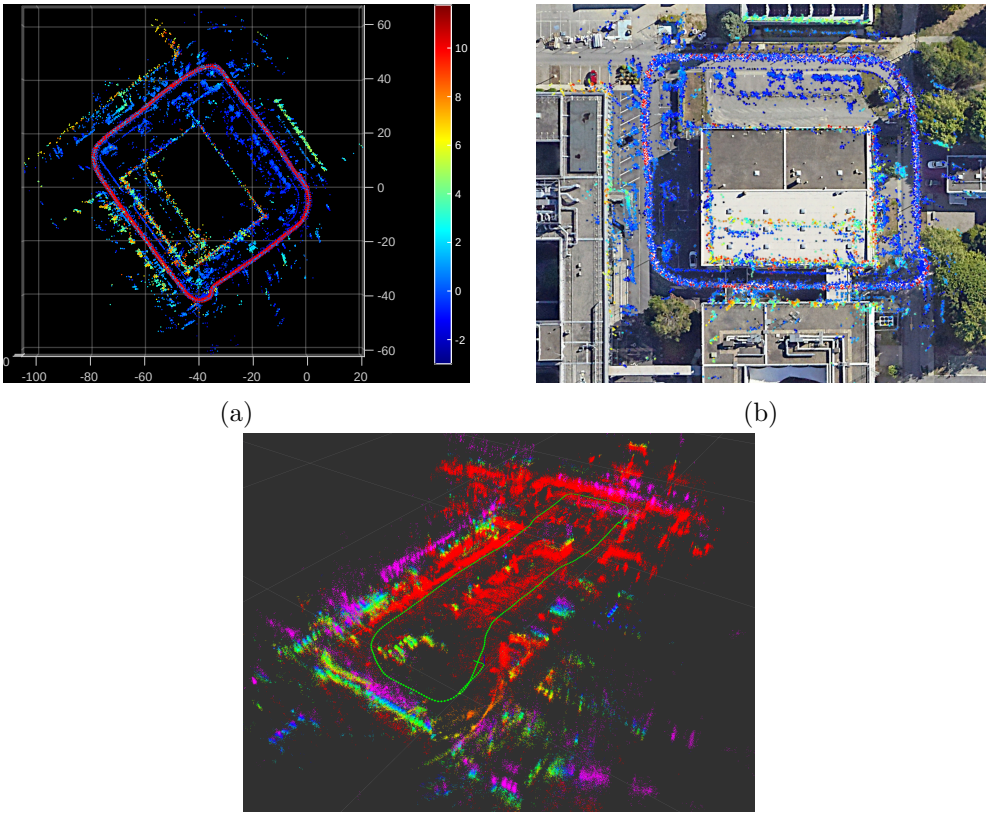

(a) (b)

(c)

Figure 4.2: Sparse mapping from concatenated pointcloud, color denotes height. Using our radar, a) Top-Down view and b) Superimposition on satellite optical image. c) Pointcloud map using high-resolution radar (48 Vx) [Zhang 2024]

4.2 Synthetic Aperture Radar

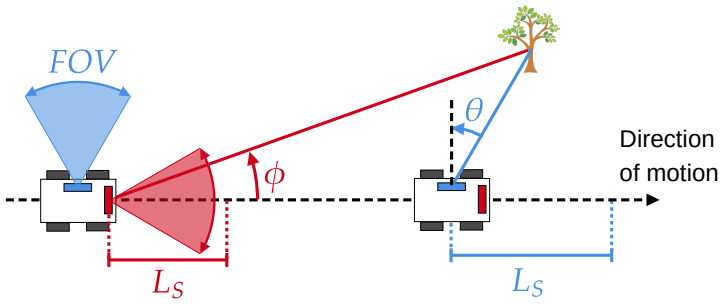

Figure 4.3: Array synthesis from front-looking and side-looking radars

One of the main issues with radar in robotics, is the sparsity and low angular accuracy of the mapping. The first arises when relying on pointcloud based methods. The second is due to the antenna aperture of the array, which is, even using a MIMO radar, quite small, imposing a poor angular resolution. The goal of using SAR imaging is to leverage both issues. This section will describe the principles of Synthetic Aperture Radar (SAR) imaging used in this thesis.

4.2.1 Motivations And Principle

Motivations As stated previously, Real Aperture Radar (RAR) angular resolution is poor making naïve mapping approach (using for example range-azimuth images or local MIMO imaging) inaccurate. To compensate this effect, the method consist in using the phase of the backscatter signal not only within one frame but using several successive frames. This results in the synthesis of a virtual array as large as the radar's displacement that significantly improve the angular resolution.

To better understand the difference, we will compare the angular resolutions associated to RAR and SAR. When we use a fixed array the angular resolution $\theta_{RAR,res}$ (detailed in section 2.5.3), is given by:

$$\theta_{RAR,res} = \frac{\lambda}{N_a d \cos(\theta)} \quad \text{with } d = \lambda/2 : \theta_{RAR,res} = \frac{2}{N_a \cos(\theta)}, \tag{4.2}$$

with θ the central off-boresight radar-scatterer viewing angle. In SAR, considering one moving antenna along a synthesised aperture of length L_S, the angular resolution $\phi_{SAR,res}$ corresponds to:

$$\phi_{SAR,res} = \frac{\lambda}{2 \sin(\phi) L_S}, \tag{4.3}$$

with ϕ the central angle between the direction of motion and synthesised array-scatterer direction [Tebaldini 2022] (illustrated in Figure 4.3).

The resulting resolutions are illustrated in figure 4.4 to compare both RAR versus forward-looking antenna SAR (FL-SAR) and versus side-looking at 90° antenna

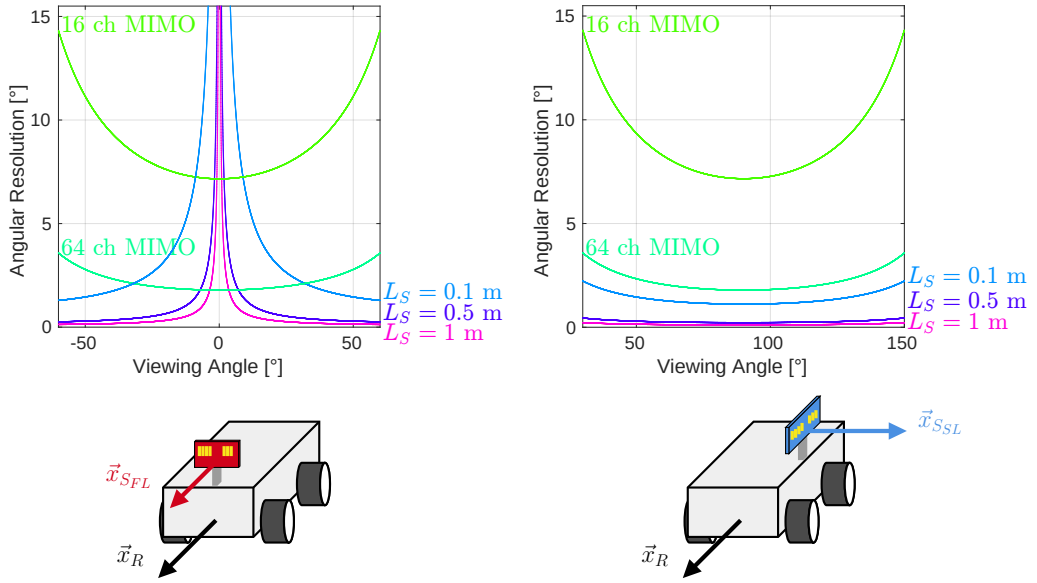

(a) (b)

Figure 4.4: RAR vs SAR angular resolution depending on the viewing angle (relatively to direction of motion) for a a) front-looking radar b) side-looking radar

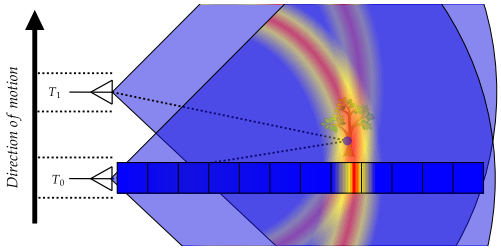

Figure 4.5: Range focused signal spread over an aperture

SAR (SL-SAR) resolutions. We can see that in the case of FL-SAR, the resolution at the front of the radar is poorer than all MIMOs but still admits a better one quite rapidly. On the other hand, all SL-SAR configurations outperforms the MIMOs resolution. From this, we can state that a low-end radar with a decent synthetic aperture can achieves better angular resolution than common to high-end MIMO radar except for forward mapping.

Principle SAR imagery consists in coherent superposition of received radar signals. As illustrated in figure 4.5, the way we synthesise a long virtual array is by "spreading" (interpolating) the up-sampled range focused backscatter signal over a small aperture angle θ_a. As a result, at each chirp received, high intensity parts of the focused signal, corresponding to scatterers, will draw circular arcs.

If radar motion estimation is accurate enough the arcs should cross (sum) at the true positions of the scatterers as shown in figure 4.6, equivalently, the strong

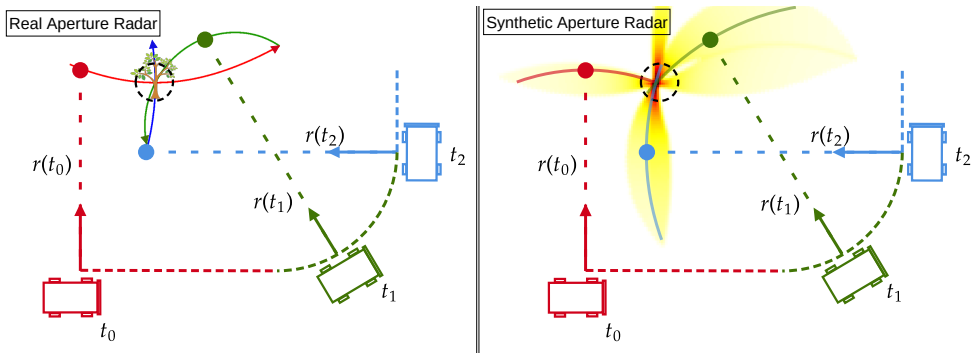

Figure 4.6: Sketch of side-looking wide beam-width mono-antenna RAR and SAR imaging principles. Along the trajectory, the radar-scatterer measured range (dots) is projected perpendicularly to the direction of motion. RAR: Solid lines represent the evolution of projected range. SAR: Measured range is spread over an aperture creating arcs. Summation of those arcs leads to an intensity grid map

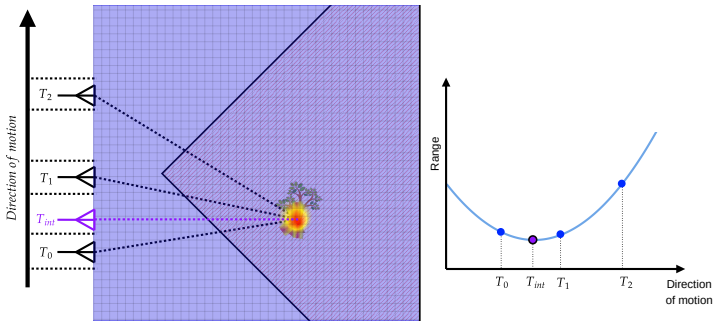

Figure 4.7: Resulting SAR image. Scatterer's position has been interpolated as if it was measured by an antenna located between T_0 and T_1. Hatched part of the drawing correspond to overlapping FOV

signal responses will overlap only around the positions of the true targets.

Considering this, by summing signals, only scatterers responses will stand out from the background. The other parts of the image will show mostly uncorrelated noise summation. By doing this, as illustrated in figure 4.7, the strong responses in the final image will correspond to scatterers' interpolated positions as if they were seen at the boresight of an antenna located on radar's path. Of course, to synthesize such an array, we need a good estimate of the radar's pose at each chirp. For having such position one can use radar odometry as described in chapter 3 or any other source of localization.

Finally, we can define the SAR map as the amplitude of the complex valued SAR image. It can be seen as an Amplitude Grid Map that uses multiple successive scans equivalently to one scan from a very large array. The result is a more accurate map than a real aperture based one.

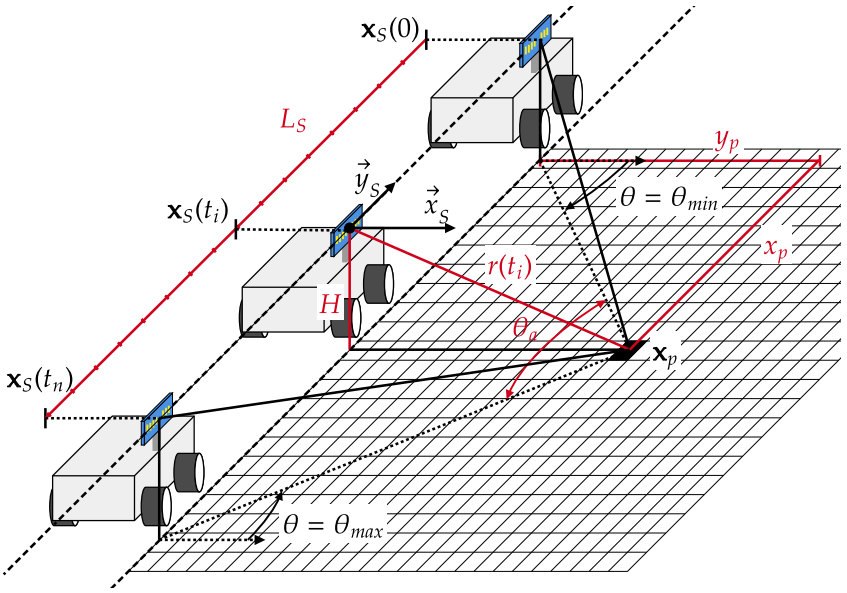

Figure 4.8: Geometry of Synthetic Aperture Radar imagery

4.2.2 Geometry

To conclude that introduction to Synthetic Aperture Radar imagery, it appear important to define the geometry of our problem and detail the resolution cited in equation 4.3. Even though the objective of this thesis is to produce SAR images in a non-rectilinear trajectory, it is clearer to first detail the rectilinear case and then extrapolate from it. This case is illustrated in Figure 4.8 showing a moving platform with position $\mathbf{x}_S = (x_S, y_S, z_S)$ along a rectilinear trajectory with a side-looking radar. The pixel centered at position $\mathbf{x}_p = (x_p, y_p, z_p)$ will contain all the contributions from the scatterers whose coordinates $\mathbf{x} = (x, y, z)$ satisfy:

$$|r - r(t)| \leq r_{res} \quad \text{and} \quad |x - x_S| \leq W_x(r, \theta_a), \tag{4.4}$$

with $r = \|\mathbf{x} - \mathbf{x}_s\|$, $r(t) = \|\mathbf{x}_p - \mathbf{x}_s\|$, W_x the footprint of the antenna system in the direction of motion and θ_a the aperture angle. This aperture angle is chosen when performing imagery, it depends on hardware and software considerations, for now it can be considered as the angle-span of the antenna diagram outside of which the backscattered signal's amplitude is considered negligible. Then, we can define the radar-pixel azimuth angle $\theta(t)$ and r_0 the minimum range during the aperture such as:

$$\begin{aligned} \sin(\theta(t)) &= \frac{x_p - x_S(t)}{r(t)}, \\ r_0 &= \sqrt{(H - z)^2 + y^2}. \end{aligned} \tag{4.5}$$

If we consider the side-looking case, as detailed in [FERRO-FAMIL 2013], by deriving the instantaneous wavenumber in azimuth, we can define the spatial azimuth

resolution (along-track direction), such as:

$$x_{res} = \frac{\lambda_c}{4\sin\left(\frac{\theta_a}{2}\right)}. \tag{4.6}$$

Now, the assumptions made to obtain the angular resolution given in equation 4.3 can be detailed:

$$\begin{aligned} \sin\left(\frac{\theta_a}{2}\right) &= \frac{L_S}{2r} \\ \Rightarrow x_{res} &= \frac{\lambda 2r(t)}{4L_S}, \text{ from eq. 4.6.} \end{aligned}$$

$$\begin{aligned} \sin(\phi + \phi_{res}) &= \sin(\phi) + \phi_{res}\cos(\phi) \\ \sin(\phi)_{res} &= \phi_{res}\cos(\phi), \text{ first order approximation.} \\ \sin(\phi)_{res} &= \frac{x_{res}}{r(t)}, \text{ from eq. 4.5.} \\ \Rightarrow \sin(\phi)_{res} &= \frac{\lambda}{2L_S} \\ \Rightarrow \phi_{res} &= \frac{\lambda}{2L_S\sin(\phi)}. \end{aligned} \tag{4.7}$$

This resolution is equivalent to the one of real aperture fixed full array of length L_S facing the orthogonal of the direction of motion.

One last point related to the SAR resolution that will be highlighted is that SAR resolution depends also on the type of trajectory since it will affect how a scatterer will be seen. Indeed, the greater the angular diversity from which a scatterer is observed, the better the resolution will be. This principle is illustrated in figure 4.9, with a SL configuration, to explicit the impact on the resolution. The inner-arc scatterer admit a resolution as if it was seen during a longer equivalent rectilinear trajectory than the one of the outer-arc scatterer. The inner-arc scatterer will be better resolved.

Finally, what can be stated from all these examples, is that what matters the most, theoretically, to improve the resolution using a SAR approach is the angular diversity. The more a single diffuser has been seen with a wide range of angles, the better its resolution will be.

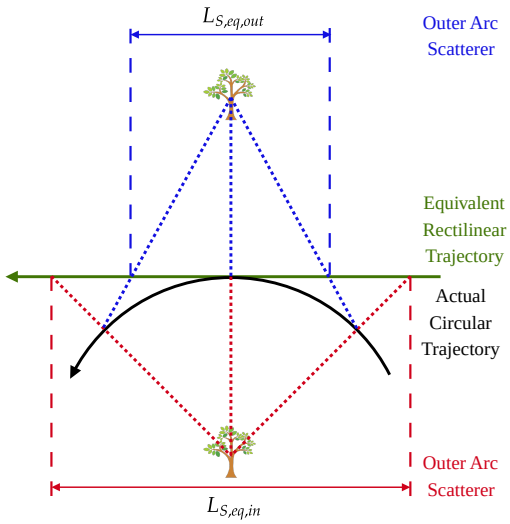

Figure 4.9: Equivalent aperture of SAR imagery depending on the trajectory and orientation of the radar: circular trajectory and $\pm 90°$ radar orientation case. The blue aperture result from a radar looking at a scatterer on the outer side of the circular radar's trajectory. The red aperture is from a scatterer located in the inner side. The greater the angular diversity from which a scatterer is observed, the larger the aperture from an equivalent radar following a rectilinear trajectory

4.2.3 State Of The Art

Historically, Synthetic Aperture Radar has been performed in space-borne and airborne contexts [Moreira 2013] but since coherent radar sensors have appeared on board moving ground vehicles, the field of application of SAR imaging has broadened. Early works demonstrating the ability to perform SAR imaging from a ground based moving vehicles dates back to early 2000s with the works of Cho *et al.* [Cho 2006] and Duersh *et al.* [Duersch 2004] with codenames μSAR and $AutoSAR$ respectively. They both presented impressive results relying on coarse SAR image generation refined via Phase Gradient Autofocus (PGA) [Wahl 1994] to get high resolution images. Cho *et al.* even showed the Interferometric SAR (InSAR) capability of their system. In 2009, Wu *et al.* [Wu 2009] proposed an automotive SAR algorithm dedicated to parking lot detection. The proposed solution is based on the use of an accelerometer estimating the radar's displacement on the range direction to perform SAR imagery from a rectilinear trajectory using $\omega - k$ algorithm (also known as Range Migration Algorithm RMA). Latter, they extended their work [Wu 2011] by using a one-axis gyroscope and a two-axis accelerometer to have a better estimate of their trajectory. The work of Stanko *et al.* [Stanko 2016] demonstrates early on what could be an upper limit of the capabilities of ground vehicle-based SAR imagery. They developed the MIRANDA-300 system which is a radar operating in the lower terahertz region (300 GHz) with a 40 GHz bandwidth and coupled it with a high-end IMU/GNSS system to achieve SAR imagery of roads

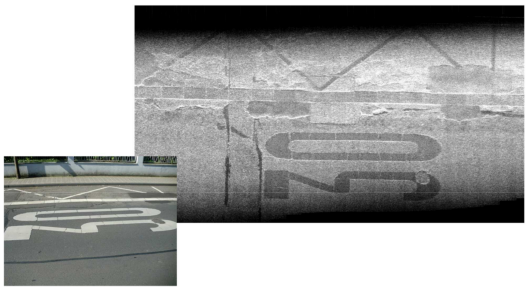

Figure 4.10: At the center, Miranda-300 SAR imaging, on the bottom left, optical image of the scene [Stanko 2016]

at a millimetre resolution level via Time Domain Back Projection (TDBP) (illustrated in figure 4.10). Then, Feger *et al.* [Feger 2017] proposed the first 77-GHz commercial sensor based SAR imaging from a moving vehicle following a rectilinear trajectory using $\omega - k$ algorithm. After that, the number of publications related to automotive SAR started to increase substantially.

Harrer *et al.* [Harrer 2017] presented a SAR algorithm aimed at creating high-resolution amplitude maps for automotive applications. This work was notable for using and describing the implementation of the TDBP to update a global map via SAR imaging on a local grid using sub-apertures. They extend their work [Gisder 2018] by presenting an online ready version of the SAR-backprojection thanks to a pixel-based parallelization concept for GPU-based SAR image calculation. A research group from Ulm University have been particularly active and prolific in the field, their works have been compiled in a book [Waldschmidt 2025] which encompasses several hot topics of millimetre wave radar. They focus mainly on the capabilities of a radar network composed of two to six sensors mounted on a car as illustrated in figure 4.11a. They started with a SAR-imaging based on a localisation solution relying on an ego-motion estimation by combining CFAR detections from 3D focused data of all sensors [Steiner 2020]. After that, they dove into environment representation by comparing OGM and SAR images from the same setup [Grebner 2022b]. They highlighted that OGMs are more robust and less computationally expensive than SAR but at the cost of a lower resolution. Finally, they proposed a SAR-imaging based on a graph-based SLAM including ego-motion estimation, OGM scan-matching and loop-closure. Another leading research group in the field of automotive SAR as of today is from Politecnico di Milano. Their approach is different since they rely on other sensors for navigation using several on-board IMUs and GNSS sensors and a wheel encoder. On the other hand they use only one MIMO radar in a forward looking configuration for SAR imaging, their experimental platform is shown in figure 4.11b. Based on that, they showed centimeter-level accuracy mapping capability in an urban environment [Rizzi 2021, Tebaldini 2022]. Next, they presented an autofocus algorithm dedicated to automotive SAR [Balducci 2023, Manzoni 2023a] to increase imaging accuracy using a Bayesan tracking of residual motion. They also presented a study

on the use of a multi-beam SAR that showed interesting results particularly for target recognition in an urban scenario [Rizzi 2022]. They also studied the impacts of multipath effects in automotive SAR [Manzoni 2023b, Manzoni 2023c]. Additionally, Gao *et al.* [Gao 2021] proposed a hierarchical MIMO-SAR algorithm for high-resolution imaging. The algorithm proposes an interesting strategy that perform CFAR detection on the data cube to perform localisation but also to define region-of-interest on which they apply backprojection to reduce computational cost compared to full SAR imaging.

More recently, Hoffmann *et al.* [Hoffmann 2023] presented a study on optimizing the backprojection algorithm to perform real-time automotive SAR imaging. They implemented various measures, including GPU utilization, mathematical optimizations, and reductions in reconstruction and aperture points, to significantly reduce computation time and data size. An interesting work has been done by Lubanco *et al.* [Lubanco 2024] who introduced a MIMO-radar-only SLAM algorithm called MS-SLAM. The algorithm estimates the traversed trajectory and builds a visual representation using only radar data, achieving high performance in place recognition and SLAM. It combines coherent and incoherent processing for mapping and operates effectively in dynamic environments. Finally, Wang *et al.* [Wang 2025] proposed a smart imaging strategy in the context of forward-looking radar mapping. Since in this configuration, at the boresight of the radar the resolution of synthetic aperture imaging is the worst and the real aperture imaging is the best, then, they combined those two means to get a best of both joint imaging. In table 4.1, we classified the SAR-related cited algorithm of this section. For image formation, algorithms like TDBP offer exact reconstruction but at a high computational cost, while Chirp Scaling is more efficient but only provides approximated results under specific conditions. $\omega - k$/RMA strikes a balance with moderate computational needs and exact reconstruction, though it requires a uniform trajectory. In terms of image refinement, techniques like PGA help correct motion-induced phase errors, improving image quality. Finally, InSAR (Interferometric SAR) by using two or more SAR images at different baselines allows to create detailed maps of surface deformation or Digital Elevation Model (DEM) with potential application in 3D autonomous navigation.

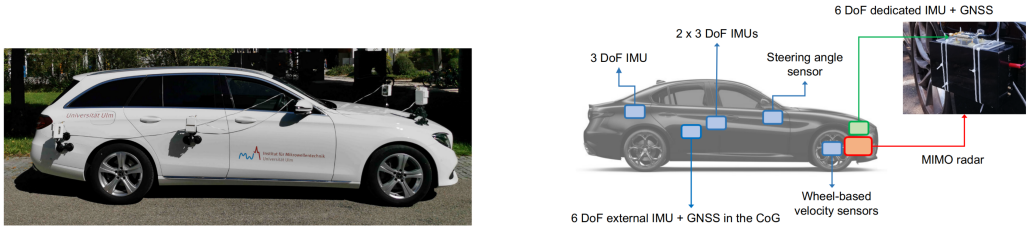

(a) (b)

Figure 4.11: Instrumented platforms of a) Ulm University, equipped with a radar network of 6 triggered sensors, and b) Politecnico di Milano with several IMUs, GNSS sensors and a wheel encoder

Type	Algorithm			
Image Formation		Computational Cost	Reconstruction Exactness	Requirements
	TDBP	High	Exact	None
	Chirp Scalling	Low	Approximated	Moderate bandwidth
	ω-k/ RMA	Mid	Exact	Uniform trajectory
Image Refinement	Autofocus	Phase-based [Eichel 1989] or Entropy-based [Xi 1999] gradient descent to correct motion-induced phase errors		
Radar Technique	Inter- -Ferometric SAR (InSAR)	Uses several SAR images to generate maps of surface deformation or digital elevation models, using phase differences		

Table 4.1: SAR related cited algorithm comparison

Discussion From this review of the existing works done on ground-based vehicle SAR imaging, we can say that it is a very active field of research where the interests of radarists and roboticists converges, often in the context of automotive SAR. The very early works were proofs of concepts using in-house sensors and setups. They showed promising results but were hard to reproduce. In the mid 2010s, SAR imagery studies using recent off-the-shelf 24 GHz and 77 GHz radars have been proposed. They cover convenient use case of rectilinear trajectory, first from a sensor bench, then with a moving vehicle. After that, in the late 2010s and beginning of 2020s, the non-linear trajectory using back projection algorithm are studied. They succeed to provide outstanding imagery results but often relying on heavy setups such as radar networks or fusion of IMU(s), GNSS sensor(s), and wheel odometry.

Furthermore, we haven't meet yet works that proposes to use both pre-processed pointcloud and raw data so that SAR mapping could be performed within a real-time framework. Finally, none of the publications cited contain any open-source code archives. From these observations, our contribution is oriented to be used with off-the-shelf sensor embedded on an UGV to perform SAR imagery. To use, if possible, pre-processed radar pointcloud for localisation to lower the computational cost. Also, it appears interesting to propose a library, mainly dedicated to roboticist, so that this discipline can get more accessible.

In our case, since we aim to develop an exact mapping that is adaptable to various configurations (sensor placement and trajectory), we will then use the Time Domain Back Projection algorithm.

4.2.4 Time Domain Back Projection

The Time Domain Back Projection (TDBP) algorithm relies on the matched filter principle. The idea is to match the radar signal obtained for every samples of each chirps to his expectation S_{exp} for every pixel of the image [Soumekh 1999]. To do so, S_{exp} corresponds to the complex-conjugate of the expected signal for a scatterer at these coordinates. Then the pixels with highest values (and SNRs) corresponds to scatterers. The image creation process is defined by :

$$I(\mathbf{x}_p) = \sum_{n_c=0}^{N_c-1} \sum_{n_s=0}^{N_s-1} S_{IF}[n_s, n_c] S_{\text{exp}}[n_s, n_c], \tag{4.8}$$

with $I(\text{x}_\text{p})$ the value of the pixel of the image I at the position $\mathbf{x}_p$. From equation 2.6, we can write the complex-conjugate of the expected IF signal for one target at the pixel located at range r_0 from the radar as:

$$S_{\text{exp}}[n_s, n_c] = e^{j\frac{4\pi}{c}(f_c+\gamma n_s T_s) r_0(n_c T_{PRI})}, \tag{4.9}$$

with $r_0(t) = ||\mathbf{x}_p - \mathbf{x}_S(t)||$, $\mathbf{x}_S$ being the position of the sensor S. The sample and chirp indices are linked so that: $t = n_c T_{PRI}$ and $\tau = n_s T_s$ meaning that we do not consider intra-chirp sensor motion. Then, we can develop the pixel value as:

$$\begin{aligned}
I(\mathbf{x}_p) &= \sum_{n_c=0}^{N_c-1} \sum_{n_s=0}^{N_s-1} S_{IF}[n_s, n_c] S_{\text{exp}}[n_s, n_c] \\
&= \sum_{n_c=0}^{N_c-1} \sum_{n_s=0}^{N_s-1} S_{IF}[n_s, n_c] e^{j\frac{4\pi}{c}(f_c+\gamma n_s T_s) r_0(n_c T_{PRI})} \\
&= \sum_{n_c=0}^{N_c-1} e^{j\frac{4\pi}{c} f_c r_0(n_c T_{PRI})} \underbrace{\sum_{n_s=0}^{N_s-1} S_{IF}[n_s, n_c] e^{j2\pi \frac{n_s}{N_s} \frac{r_0(n_c T_{PRI})}{r_{res}}}}_{\text{DFT}^{-1}\left[S_{IF}[\frac{r_0(n_c T_{PRI})}{r_{res}}, n_c]\right]} \\
&= \sum_{n_c=0}^{N_c-1} e^{j\frac{4\pi}{c} f_c r_0(n_c T_{PRI})} \underbrace{s_{IF}\left[\frac{r_0(n_c T_{PRI})}{r_{res}}, n_c\right]}_{\text{Interpolation of } s_{IF,up}}.
\end{aligned} \tag{4.10}$$

As detailed in this equation, the value of a pixel correspond to the sum of all the interpolated range focused signal impacting that location multiplied by a factor $e^{j\frac{4\pi}{c} f_c r_0(n_c T_{PRI})}$. The up-sampled range focused signal $s_{re,up}$ is obtained via an inverse DFT on the up-sampled mixed signal (zero-padding). The up-sampling factor N_{up} is generally chosen to be 4 or 8, resulting in an up-sampled range vector $\mathbf{r}_{up} = [0, \frac{r_{res}}{N_{up}}, \frac{2r_{res}}{N_{up}}, ..., r_{max}]$ of size $N_s N_{up}$. The range focused signal is obtained via a linear, cubic or spline interpolation. In our case, we use a linear interpolation.

Then we have:

$$
\begin{aligned}
r = r_0(n_c T_{PRI}), \qquad & r_{res,up} = \frac{r_{res}}{N_{up}} \\
n_{up,f} &= \lfloor \frac{r}{r_{res,up}} \rfloor \\
\left\{ \frac{r}{r_{res,up}} \right\} &= \frac{r}{r_{res,up}} - n_{up,f} \\
S_{IF}[\frac{r}{r_{res}}, n_c] &= s_{re,up}[n_{up,f}, n_c] \\
&\quad + \left\{ \frac{r}{r_{res,up}} \right\} (s_{re,up}[n_{up,f}+1, n_c]) - s_{re,up}[n_{up,f}, n_c]),
\end{aligned}
\tag{4.11}
$$

with $\{\cdot\}$ and $\lfloor \cdot \rfloor$ the fractional and integer part functions respectively. For clarity reason, we derived the method considering N_c chirps, meaning an aperture of one frame, but the calculations are the same for $N_c N_f$ chirps.

As a result, the SAR image can be built using the Time Domain BackProjection algorithm. Next section will focus on the practical implementation we used for SAR imaging.

4.2.5 Performing SAR Imagery

The synoptic of the SAR processor developed in this thesis is illustrated in figure 4.12. In this section, we will explain how it works and each bold word will be the subject of paragraph dedicated to the explanation of that step.

Pipeline The processor is first **initialised**. Then the main loop is launched in an independent thread ①. This loop will grab the frames from the queue filled by the sensor ②, waiting to have N_f frames forming a sub-aperture of the final global image. If the N_f frames have been collected, we will get the **local grid** on which we will work by extracting the part of the global grid that the radar has seen during the sub-aperture ③. After that, we get the signal spectrogram of the sub-aperture via an inverse DFT on the samples of all the $N_c N f$ chirps collected ④. We perform a **leakage removal** on that signal spectrogram ⑤. Then, to obtain the local SAR image we go through the operations of radar-pixels **distances computations**, **culling**, **signal interpolation**, local summation and **normalization** in a for loop that iterates $N_c N_f$ times ⑥. This loop is parallelized to lower the computational time. Then, the local SAR map is summed to the global SAR map which is normalized also ⑦. Then the updated global SAR map is available. Data related to the local SAR map are cleaned and the first loop starts grabbing frames from the queue again.

Initialisation This first step consist in mainly two steps: collect some required parameters (frequencies, range resolution, etc.) and allocate the global grid map. It is on this map that we will sum all the future sub-aperture images. We chose to

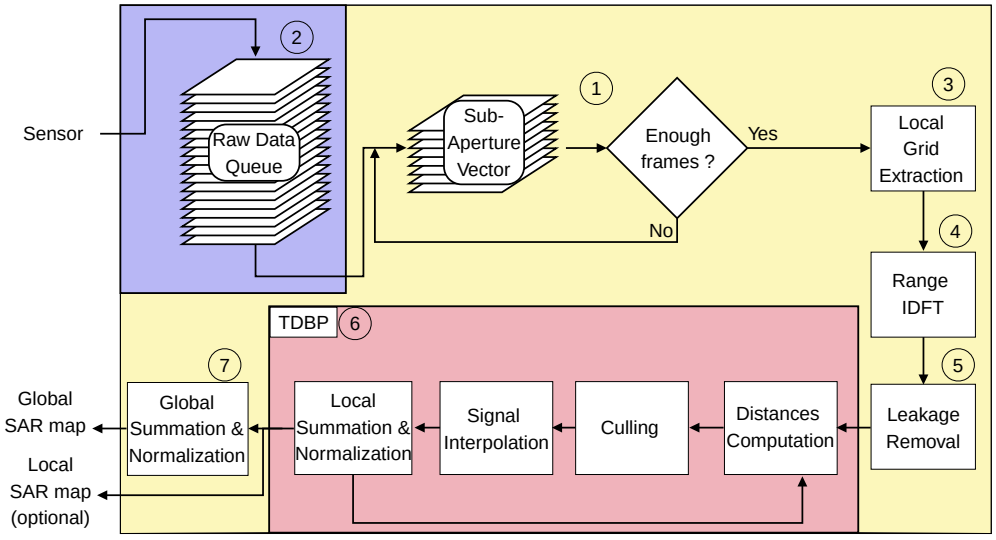

Figure 4.12: Pipeline of the SAR processor class. Each color depicts a thread fashion. Yellow and red boxes are running independently from the blue one. Yellow operations are done sequentially (mono-threaded) while the TDBP is multi-threaded. Blue part is called by the SLAM when a radar frame is sent to the SAR Processor. The interface between the SAR processor are done via the shared data queue (input) and displayable SAR map (output)

initialise it at a fixed size and resolution. It needs to be large enough to encompass the desired area to map. The pixel resolution can be chosen based on many parameters: the range resolution, the desired computation time, the type of trajectory. For example in our case, since the radar is following an uncharacterised trajectory, we are using squared pixels, then $\Delta x = \Delta y$. The global map size (number of pixels) is then defined as:

$$(N_{u,G}, N_{v,G}) = \left(\frac{x_{sar,max} - x_{sar,min} + 1}{\Delta x}, \frac{y_{sar,max} - y_{sar,min} + 1}{\Delta y} \right).$$

Defining the vectors of pixel global coordinates as

$$\mathbf{u_G} = [x_{sar,min},\ x_{sar,min} + \Delta x,\ \ldots, x_{sar,min} + (N_{u,G} - 1)\Delta x]\,.$$

and

$$\mathbf{v_G} = [y_{sar,min},\ y_{sar,min} + \Delta y,\ \ldots, y_{sar,min} + (N_{v,G} - 1)\Delta y].$$

Local Grid Extraction The figure 4.13 illustrates how the local grid map is extracted from the global grid map.

We need to compute the world coordinates of the vertices that encompass the total FOV of the sub-aperture. First, we need to compute the positions of each FOVs extremums in the sensor frame : $\begin{pmatrix} x^S_{FOV,left} \\ y^S_{FOV,left} \end{pmatrix}$, $\begin{pmatrix} x^S_{FOV,right} \\ y^S_{FOV,right} \end{pmatrix}$, $\begin{pmatrix} x^S_{FOV,mid} \\ y^S_{FOV,mid} \end{pmatrix}$

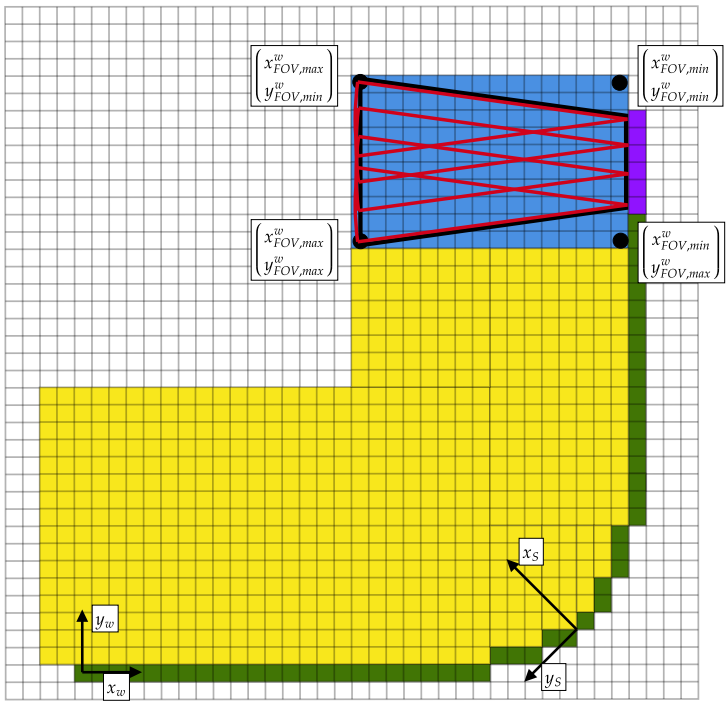

Figure 4.13: Extraction of the local grid map (blue) from the global grid map (white). In yellow are the pixels of the global map that have been seen in the past. In green, the past trajectory of the side looking radar (with a past sensor frame). In purple, the trajectory of the sensor during the sub-aperture used to synthesise the local SAR image

and transform those into the world frame to get $\begin{pmatrix} x^w_{FOV,left,n_f} \\ y^w_{FOV,left,n_f} \end{pmatrix}$, $\begin{pmatrix} x^w_{FOV,right,n_f} \\ y^w_{FOV,right,n_f} \end{pmatrix}$, $\begin{pmatrix} x^w_{FOV,mid,n_f} \\ y^w_{FOV,mid,n_f} \end{pmatrix}$, with $n_f \in [0, N_f[$. Then we have:

$$\begin{aligned} \begin{pmatrix} x^w_{FOV,max} \\ y^w_{FOV,max} \end{pmatrix} &= \begin{pmatrix} \max\limits_{n_f}\left(x^w_{FOV,right,n_f}, x^w_{FOV,left,n_f}, x^w_{FOV,mid,n_f}, x^w_{S,n_f}\right) \\ \max\limits_{n_f}\left(y^w_{FOV,right,n_f}, y^w_{FOV,left,n_f}, y^w_{FOV,mid,n_f}, y^w_{S,n_f}\right) \end{pmatrix} \\ \begin{pmatrix} x^w_{FOV,min} \\ y^w_{FOV,min} \end{pmatrix} &= \begin{pmatrix} \min\limits_{n_f}\left(x^w_{FOV,right,n_f}, x^w_{FOV,left,n_f}, x^w_{FOV,mid,n_f}, x^w_{S,n_f}\right) \\ \min\limits_{n_f}\left(y^w_{FOV,right,n_f}, y^w_{FOV,left,n_f}, y^w_{FOV,mid,n_f}, y^w_{S,n_f}\right) \end{pmatrix}, \end{aligned} \tag{4.12}$$

with $\begin{pmatrix} x^w_{S,n_f} \\ y^w_{S,n_f} \end{pmatrix}$ the 2D translations from world to sensor frames. Then, we look for the integer coordinates of the closest pixels in the global map corresponding to the vertices $\begin{pmatrix} x^w_{FOV,max} \\ y^w_{FOV,max} \end{pmatrix}$, $\begin{pmatrix} x^w_{FOV,min} \\ y^w_{FOV,min} \end{pmatrix}$ for, respectively, bottom-left and top-right

corners of the local map:

$$\begin{aligned}\begin{pmatrix} u_{L,min} \\ v_{L,min} \end{pmatrix} &= \begin{pmatrix} \underset{u}{\text{argmin}}(|\mathbf{u}_G(u) - x^w_{FOV,min}|) \\ \underset{v}{\text{argmin}}(|\mathbf{v}_G(v) - y^w_{FOV,min}|) \end{pmatrix} \\ \begin{pmatrix} u_{L,max} \\ v_{L,max} \end{pmatrix} &= \begin{pmatrix} \underset{u}{\text{argmin}}(|\mathbf{u}_G(u) - x^w_{FOV,max}|) \\ \underset{v}{\text{argmin}}(|\mathbf{v}_G(v) - y^w_{FOV,max}|) \end{pmatrix}. \end{aligned} \tag{4.13}$$

yielding a local map of size $(N_{u,L}, N_{v,L}) = (u_{L,max} - u_{L,min} + 1, v_{L,max} - v_{L,min} + 1)$. From this, we can perform block operations on the global map using these variables: $(u_{L,min},\ v_{L,min},\ N_{u,L},\ N_{v,L})$. The vectors of pixel local coordinates will be denoted as $\mathbf{u}_L$ and $\mathbf{v}_L$. To speed-up equations 4.15 and 4.16, when we create the local grid map, we will define the matrices of the coordinates of the pixels, U_L and V_L, such as:

$$\begin{aligned} U_L &= \underbrace{\begin{bmatrix} \mathbf{u}_L & \dots & \mathbf{u}_L \end{bmatrix}}_{N_{v,L} \text{ columns}}. \\ V_L &= \begin{bmatrix} \mathbf{v}_L^T & \dots & \mathbf{v}_L^T \end{bmatrix}\}, \ N_{u,L} \text{ rows}. \end{aligned} \tag{4.14}$$

Tx-Rx Leakage Removal When using wide beam antennas, a constant strong response at low range values appears (see Fig. 4.14a).

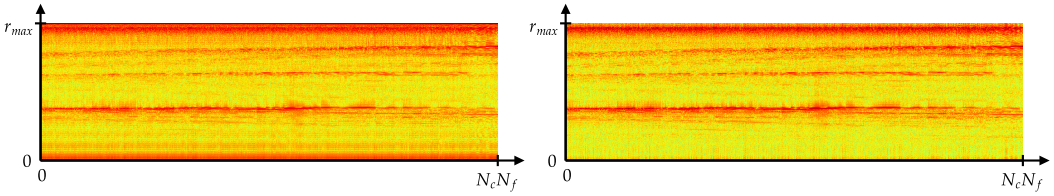

(a) (b)

Figure 4.14: Backscatter signal spectrograms a) before and b) after leakage removal

This is due to signal leakage: the direct propagation of the signal from Tx to Rx is causing at the beginning of the sampling interval a high response which fades rapidly depending on the path taken by the signal as illustrated in figure 4.15.

To reduce this effect, we compute the complex vector of mean values of each sample's complex value over the N_cN_f chirps and subtract this complex mean to the spectrogram. Since the leakage is the only constant and strongly correlated response over time, the other parts of the signal will be shifted but keeps the same distribution. The effect of the leakage removal can be seen on the re-normalized backscatter signal spectrogram in figure 4.14b.

Distances Computation To be able to interpolate the signal for each pixel as required in equation 4.10, we need to compute the distance matrix D_i at each

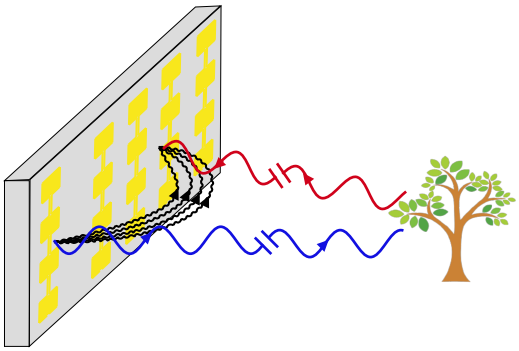

Figure 4.15: TX-RX leakage path compared to useful sent and received signal

iteration $i \in [0, N_c N_f[$ such as:

$$\begin{aligned} D_i &= \begin{bmatrix} ||\mathbf{x}_p^w(0,0) - \mathbf{x}_{S,i}^w|| & ||\mathbf{x}_p^w(0,1) - \mathbf{x}_{S,i}^w|| & \cdots \\ ||\mathbf{x}_p^w(1,0) - \mathbf{x}_{S,i}^w|| & \ddots & \\ \vdots & & ||\mathbf{x}_p^w(N_u-1, N_v-1) - \mathbf{x}_{S,i}^w|| \end{bmatrix} \\ &= \sqrt{(U_L - x_{S,i}^w) \odot (U_L - x_{S,i}^w) + (V_L - y_{S,i}^w) \odot (V_L - y_{S,i}^w)} \end{aligned} \tag{4.15}$$

With, $\odot$ the element-wise product, $\mathbf{x}_{S,i}^w$ the 2D interpolated position of the sensor in world frame at time iT_c and $\mathbf{x}_p^w(u,v) = (\mathbf{u}_L(u), \mathbf{v}_L(v))^T$ the world position of the local map pixel at coordinates (u,v).

Culling The term comes from the computer graphics domain and is used to compute, as an example, what is seen by the user in a video game at each frame. In our case, by defining an aperture angle θ_a, we want to check for each chirp if a pixel from the local map is seen by the radar or not. To do so, it exists many methods. In our case, as shown in figure 4.16, what we need to do is 2D rasterization, meaning that we want to check what pixels lies within a cone defined by the radar pose located at the vertex V_0, oriented in direction of vertex V_d with a maximum and minimum range r_{max} and r_{min} over an azimuthal aperture of θ_a. First, we need to do an angular check using dot-product:

$$\begin{aligned} &\mathbf{x}_p = \begin{pmatrix} x_p \\ y_p \end{pmatrix}, \mathbf{x}_S = \mathbf{x}_{V_0} = \begin{pmatrix} x_S \\ y_S \end{pmatrix}, \mathbf{x}_{V_d} = \begin{pmatrix} x_{V_d} \\ y_{V_d} \end{pmatrix} \\ &\vec{A} = \mathbf{x}_p - \mathbf{x}_S, \vec{B} = \mathbf{x}_{V_d} - \mathbf{x}_S \\ &\cos(\phi) = \frac{\vec{A}\vec{B}}{||\vec{A}||\ ||\vec{B}||} = \frac{\vec{A}\vec{B}}{D_i(u,v)} \\ &\cos(\theta_a) > \frac{\vec{A}\vec{B}}{D_i(u,v)} \end{aligned} \tag{4.16}$$

Since V_d is only a direction unit vector, we have $||V_d|| = 1$. One could notice that this operation is similar than the one of the local grid extraction. The culling operation is a precise check of which pixel among the local grid is seen at each chirp acquisition time ($N_c N_f$ checks). In contrast to the local grid extraction that is a coarse estimation of the grid that encompasses the FOVs at each frame time.

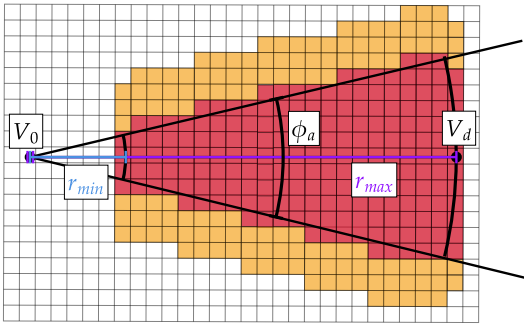

Figure 4.16: Rasterization of the SAR aperture on the local image. The pixels currently seen are in red and in orange the ones that are seen within the same sub-aperture

Normalizations To share a common scale of amplitude between both each local and global map over time, it is necessary to normalize the maps. When initializing global and local maps, we also initialize the counter matrices C_G and C_L as all-ones matrices (the division identity) of the same size as the maps. Then, each time interpolated data is summed into a pixel that has already been observed, we increment the corresponding pixel in the matrix C_L by one. When merging the local map into the global map, we increment all observed pixels in C_G by one for that sub-aperture. Finally, the normalization of the global is done thanks to an iterative average such as:

$$I_G(k) = I_G(k-1) \odot (C_g(k) - 1) + \frac{I_L}{C_g(k)} \tag{4.17}$$

With I_L the local grid map, $I_G(k)$ and $C_g(k)$ the global grid map and its associated counter at iteration k ($k-1$ is related to before summation and k after summation).

Finally, an example of the raw global SAR image obtained is presented in the figure 4.17. This map covers half of the mechanical club building of the ISAE-SUPAERO's campus using a side-looking radar mounted on our rover.

To validate this SAR pipeline with our different radar embedded on the robot, we perform different validations steps with simple use case that will be described in next section.

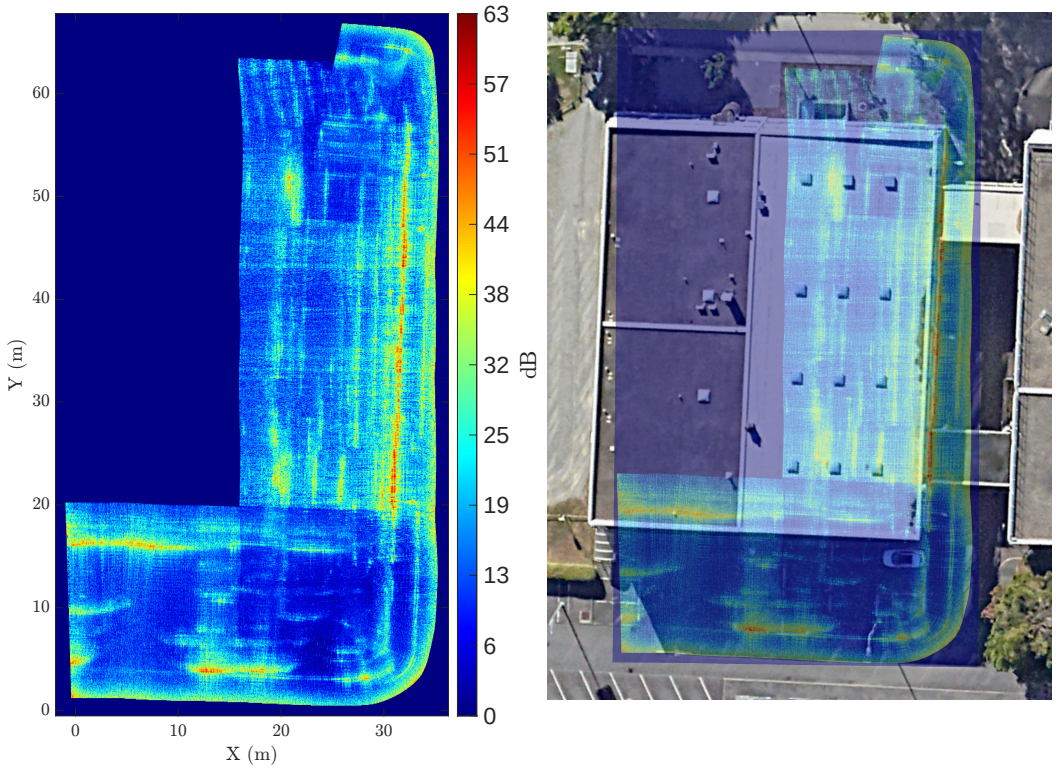

(a) (b)

Figure 4.17: Amplitude in dB of Raw Global SAR image and its projection on optical satellite image using Google Earth

4.3 Validation Steps

To validate our SAR imaging, we first perform it on a straight-line trajectory using ground-truth positioning with a 24 GHz radar. Next, we repeated the validation but replaced ground truth with velocity estimation. Finally, we confirmed the imaging performance using both 24 GHz and 77 GHz sensors on a 2D planar trajectory using ground-truth positioning.

4.3.1 Rectilinear Trajectory

The very first experiment was to produce a SAR image using a 24 GHz side-looking sensor following a rectilinear trajectory perpendicular oriented to the imaged scene. It has been achieved both relying on a ground-truth (GT) positioning using a Differential-GNSS (D-GNSS) having a millimeter accuracy and localisation from the integrated estimated velocity. First, we will detail the performance of our 1-D position estimation. In figure 4.18, we can see that, the estimated velocity along $\overrightarrow{y}$ axis is not well estimated. Then, since we knew the rover was following a quasi-straight trajectory we used a 1d-velocity estimation. Also, we can notice that the

RanSaC outlier rejection helps significantly to get a better accuracy. The produced images are shown in figures 4.19. They are almost identical, but there are still differences, since the estimated velocity is not as accurate as the GT. A noticeable difference is highlighted with boxes in the images. Since our position estimate accumulates errors, particularly along the $\overrightarrow{y}$ axis, the pavement is not as straight as with GT positioning.

For qualitative results, in figure 4.20, the image has been superimposed on an optical satellite image of the measured scene.

To validate the imagery we would like to check its quality via quantitative results. It exists numerous metrics to estimate a quality of a SAR image or compare two SAR images [Chatzitheodoridi 2023], in our case we choose to compute the classical entropy metric E of both images. Entropy is a statistical measure of randomness that can be used to characterize the texture of the input image. The entropy is calculated thanks to equation 4.18.

$$\begin{aligned} q_{\mathbf{x}} &= |I(\mathbf{x})|, \\ Q &= \sum_{\mathbf{x}} q_{\mathbf{x}} \\ p_x &= \frac{q_{\mathbf{x}}}{Q} \\ E &= -\sum_{\mathbf{x}} p_x \log_2(p_x). \end{aligned} \tag{4.18}$$

We can observe that the entropy of the image synthesised using the GT positioning is lower than the one from integrated estimated velocity but still close : $E_{GT} = 0.0745$, $E_{Odom} = 0.0773$.

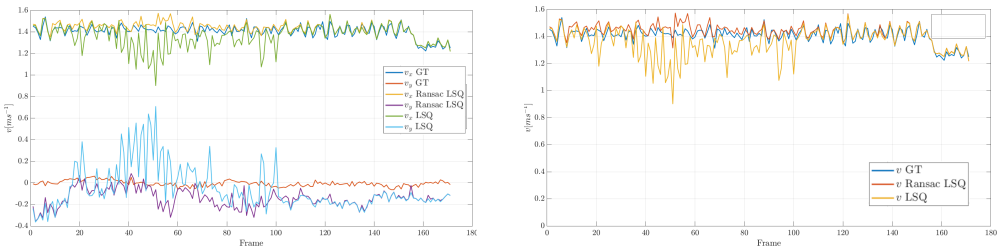

(a) (b)

Figure 4.18: GT velocity compared to estimated velocity using a LSQ approach with or without RANSAC outlier rejection

Once the easier case of rectilinear trajectory has been validated, the goal was to reproduce such results on non-linear trajectory.

4.3.2 Non-Linear Trajectory

The validation of SAR imagery from a non-linear trajectory has been done with both 24 GHz and 77 GHz radars using whether GT positioning or our odometry.

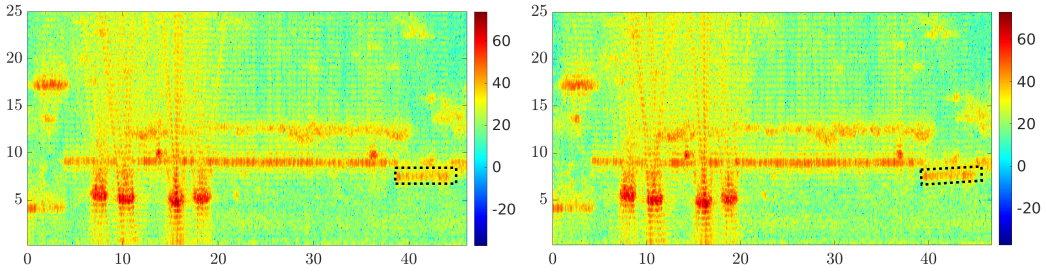

(a) (b)

Figure 4.19: Normalized backscatter in dB (log-amplitude) of SAR images using a side-looking 24 GHz sensor relying on a) GT positioning and b) integrated estimated velocity

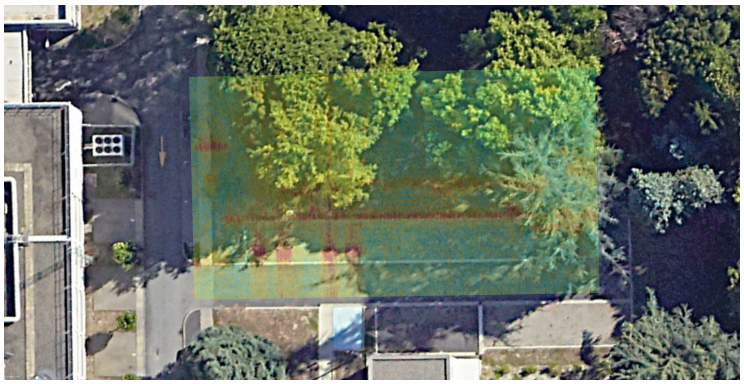

Figure 4.20: SAR image superimposed on an optical satellite image of the measured scene

4.3.2.1 With GT positioning

24 GHz First, with the radar used in the previous section, we validated the imagery on a non-straight trajectory. To provide a more straightforward visualisation, figure 4.21 shows the normalised SAR image and the same image after applying a morphological opening operation and cutting at 0 dB. The ability to finely image scatterers such as metal poles assess the quality of the SAR imagery. For qualitative result, the SAR image has been superimposed on an optical satellite image in figure 4.25a.

The portion of the trajectory on the upper part of the image is challenging for SAR imagery. It is a narrow passage between two concrete buildings with two overhead walkways which make it prone to interference and multipath effects (especially visible at locations $[5, 50]$ and $[35, 50]$, depicted in Figure 4.22). However, we can see that the reconstruction is consistent with the shape of the buildings. Metal targets such as posts, lampposts, and cars respond very strongly. The same applies to buildings and road surfaces made of concrete. An interesting result is that we can discern a difference in the intensity of the response from the bushes

in the lower right-hand corner of the image. We wanted to test the see-through capability of a 24 GHz radar. Figure 4.23 shows the SAR image focused when the radar is behind these bushes. Even at 24 GHz, the bushes appear too dense to see the metal posts that should be located around $[-10, 10]$ in the local image.

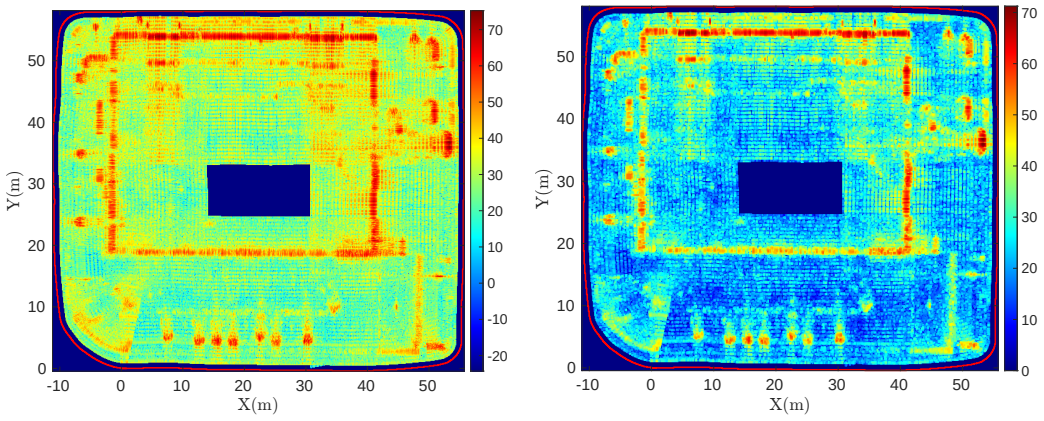

Figure 4.21: Normalized backscatter in dB (log-amplitude) of :
a) SAR image from a non-straight trajectory using a 24 GHz radar
b) SAR image after opening morphological operation and cutting at 0 dB

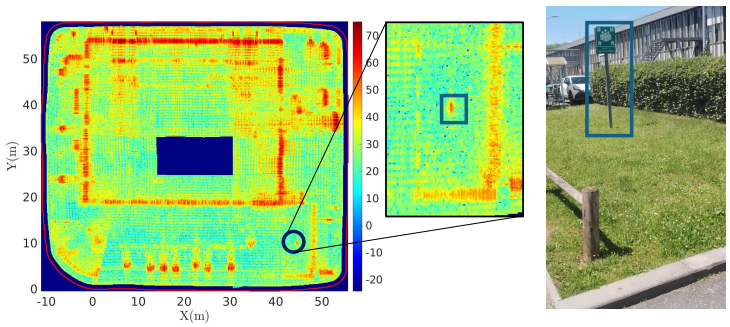

Figure 4.22: Point diffuser imaging and associated object

77 GHz After testing SAR imagery using a 24 GHz radar, we wanted to use a higher dynamic one. A 77 GHz radar has the benefit of having access to a larger bandwidth (typically $B > 1$ GHz $\Leftrightarrow r_{res} < 15$cm) but will be more sensible to positioning error. In figure 4.24 are illustrated the SAR imagery on a part of a similar trajectory as the one in the previous paragraph.

To compare the imagery quality between two type of sensors, SAR images from both have been projected on optical satellite image in figure 4.25. To make a link between scatterers in SAR images and real objects, an association is given in figure 4.26 using images from an embedded fish-eye camera. It is clear from these figures

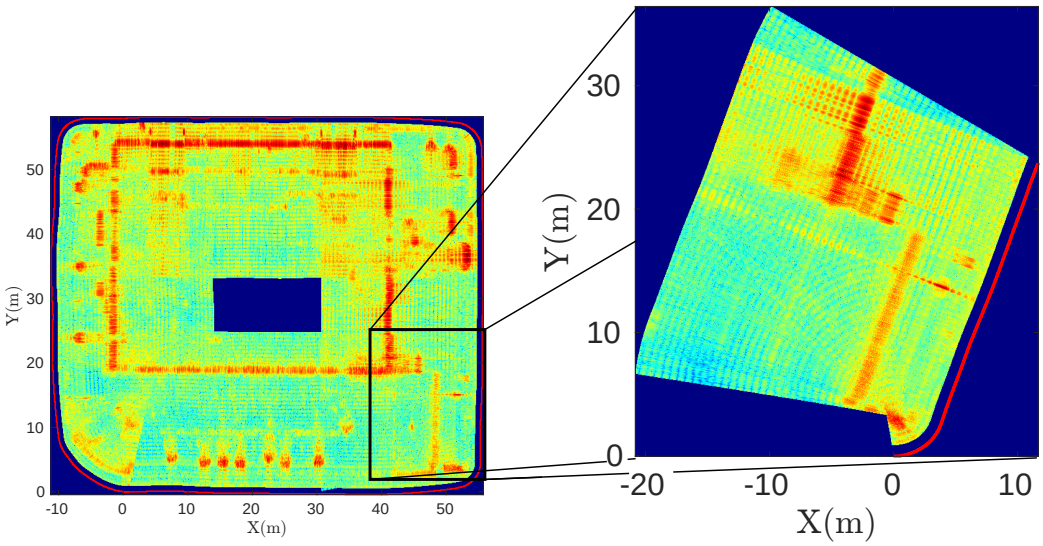

Figure 4.23: 24 GHz SAR image synthesised from behind the bushes

that both type of sensors are affected by the narrow passage and the walkways. The effect of a better range resolution using the 77 GHz sensor is quite clear on the effect of the imagery. The large scatterers such as walls or pavements admit a much thinner response and the point scatterers appear finely resolved. Nevertheless, it appears that 77 GHz imagery is more prone to speckle rather than the 24 GHz one. This could be due to an inaccurate estimation of the radar trajectory, with potential sources being time synchronisation or extrinsic calibration between GT and radar data. However, we can apply morphological operations to reduce the impact of speckle on the mapping, and the points of interest remain visible.

We have seen the results of SAR imagery using the ground-truth trajectory, we will now detail the impact on the imagery when using the radar-based estimated trajectory .

4.3.2.2 With Odometry

The setup used consists in a front-looking radar dedicated to odometry and a front-looking one for imagery. The localisation strategy is detailed and justified in Chapter 3. For this experiment, we rely on a Doppler-Angle based translation estimation and we use KISS-ICP for rotation estimation resulting in a 2D pose mono radar-only odometry. The synthesised images using estimated and GT trajectory are illustrated in Figures 4.27a and 4.27b respectively. In figure 4.27c we can see the comparison of the used trajectories after Umeyama alignment. We can see that the odometry admit an angular error at the beginning of the trajectory that won't be corrected changing the shape of the image. Otherwise, the imagery is quite similar compared to the GT-based one.

We have seen the validation steps of the SAR algorithm on both rectilinear and non-linear trajectories and compared the results when using a 24 GHz or a 77 GHz

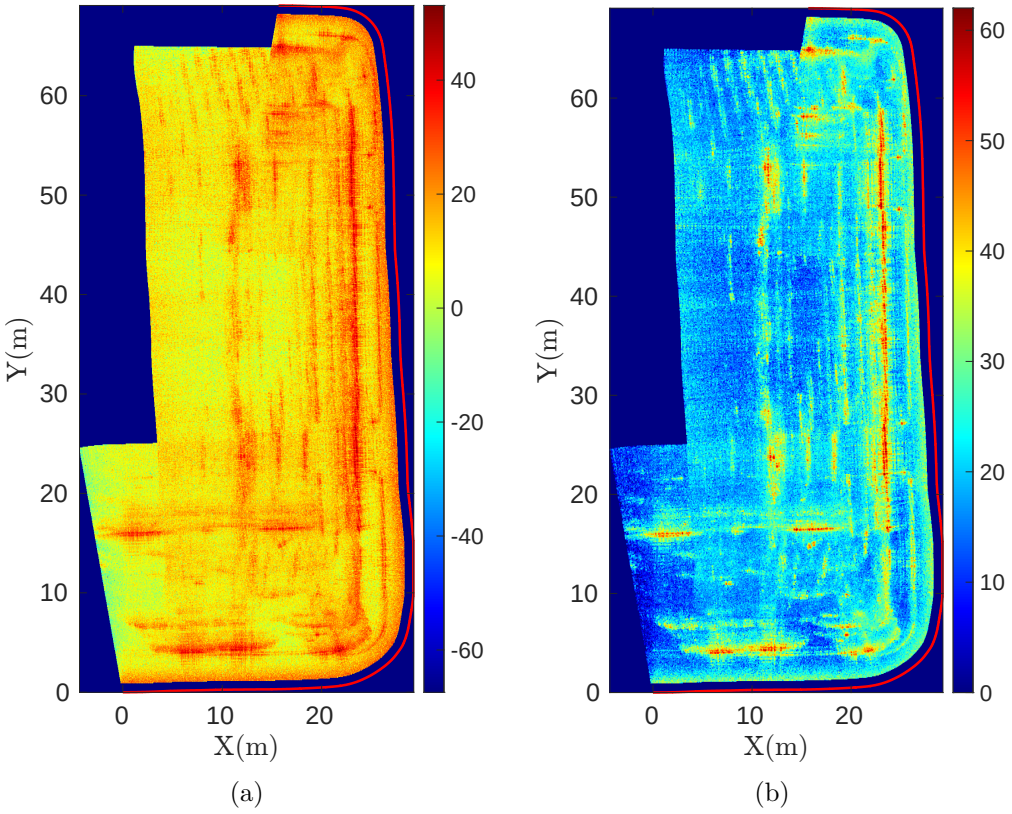

Figure 4.24: Normalized backscatter in dB (log-amplitude) of :
a) SAR image from a non-straight trajectory using a 77 GHz radar
b) SAR image after opening morphological operation and cutting at 0 dB

sensor in different configurations. Now, the role of the chosen processed angular aperture will be examined.

4.3.3 Processed Angular Aperture

The choice of $\theta_{a,proc}$ the processed width of the aperture is crucial, in our context, it depends highly on experimental conditions. We will first develop the sampling requirements related to our system. From [FERRO-FAMIL 2013], we have :

$$\begin{aligned} &\frac{v}{x_{res}} \leq PRF \leq \frac{1}{T_{amb}} = \frac{c}{2r_{max}} \\ &x_{res} = \frac{\lambda_c}{4sin(\frac{\theta_a}{2})}, \end{aligned} \tag{4.19}$$

with v, x_{res} the velocity of the platform and the azimuth resolution respectively. The order of magnitude of the used PRF is $\approx 10^3$Hz, which largely respect the $1/T_{amb} \approx$ 10 MHz condition. Then, with $v = 1.5$ m.s^{-1}, we could reach an azimuth resolution of $x_{res,min} \approx 1.5$mm with $\theta_{a,proc} = 2\text{asin}(\lambda_c/(4x_{res,min})) \approx 80°$. Unfortunately, as

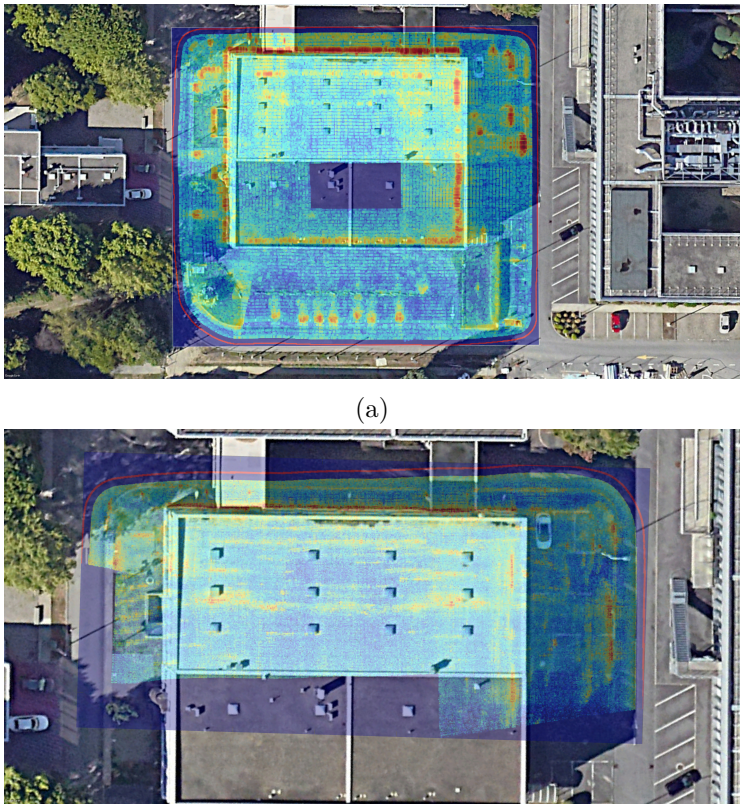

(a)

(b)

Figure 4.25: Normalized backscatter in dB (log-amplitude) super-imposed on optical satellite image from Google Earth with a) 24 GHz and b) 77 GHz sensors' SAR images after opening morphological operation and cutting at 0 dB

depicted in figures 4.28a, 4.28b and 4.28c with SAR images having aperture angles $\theta_a = 5°, 10°$ and $20°$ respectively, it is not the case (see figure 4.29 for context). When increasing the processed aperture, there are others effects to take into account that will affect the resolution of the image due to phase errors. Firstly, diffusers with rough surfaces allow backscatter that is not identical for different viewing angles, so the signal is no longer strictly coherent. Second, using observations at large viewing angles is prone to decrease resolution. Indeed, an inaccurate positioning will introduce a distance error δd (between each pixel and the antenna) giving a phase error $\Delta\phi$ such as:

$$\Delta\phi = \frac{4\pi}{\lambda_c}\delta R. \tag{4.20}$$

In our case, if we consider $\delta R = 0.1$mm, we obtain $\Delta\phi \approx 185°$ which corresponds almost as a complete phase reversal. We have detailed the advantages of a 77 GHz sensor earlier, in the context of SAR, such a frequency (short λ_c) requires a positioning accuracy in the order of magnitude of 0.1mm.

To lower these effects, the angular aperture is chosen in consequences. On one

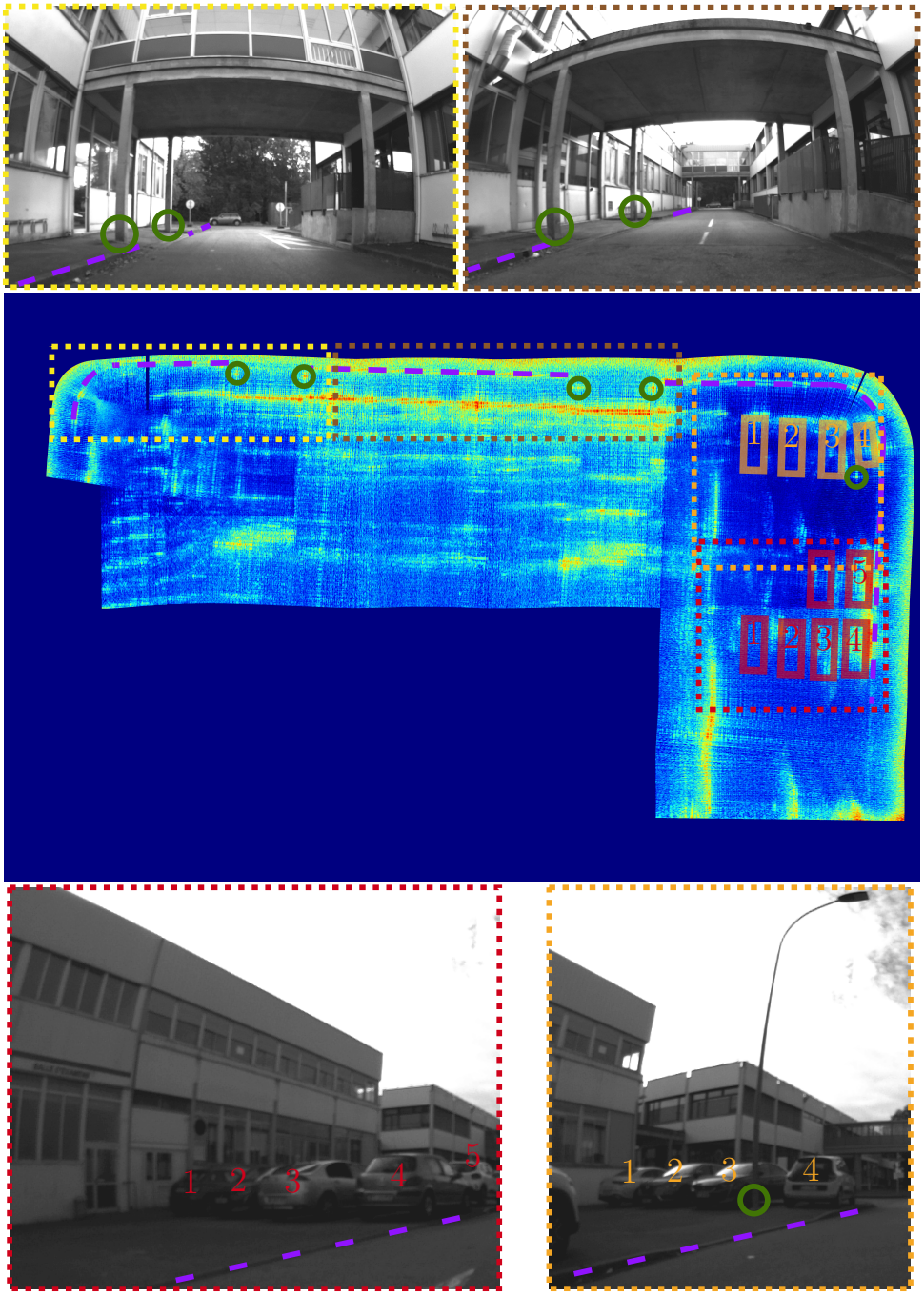

Figure 4.26: Link between scatterers in SAR image and associated objects in image from embedded fish-eye camera. Dotted rectangles are related to approximation of viewed scenes from each images. Digits and rectangles are related to cars. Green circles are related to point scatterers such as poles and pillars. Dotted magenta lines are related to sidewalks

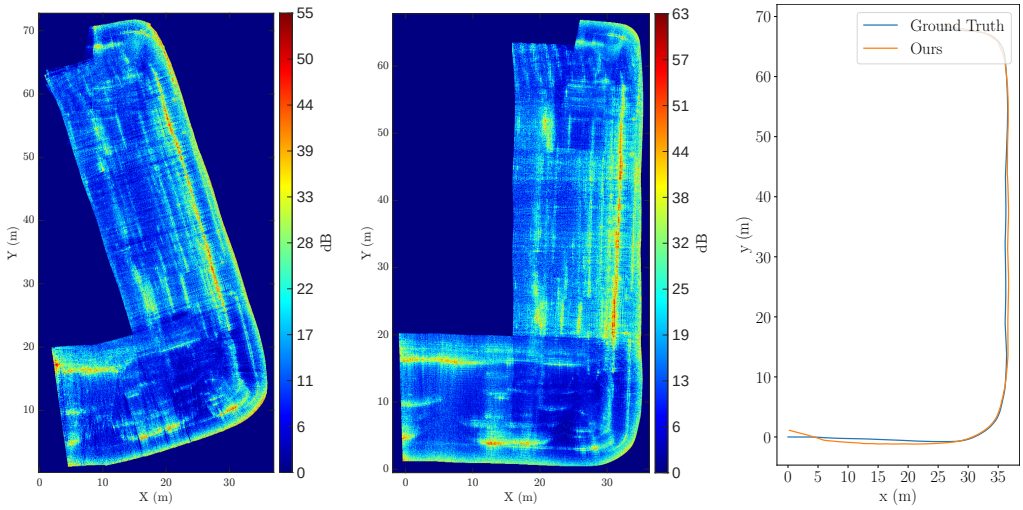

(a) (b) (c)

Figure 4.27: Amplitude in dB of SAR image using a) estimated and b) GT trajectory using a 77 GHz sensor.
c) Orange : estimated trajectory after Umeyama alignment on GT (blue)

hand, if it is too narrow the length of the aperture L_S will be short, we synthetize a smaller array with a poorer resolution. On the other hand, if it is too wide, it will deteriorate the coherency of the phase each time we integrate signal having effects such as increasing the width of the main lobe (degraded resolution), sidelobes increasing and apparent noise increases as useful coherence collapses.

After giving explanations on the choice of the processed aperture angle, we propose to define the specificities of the SAR mapping in the context of robotics by comparing it to lidar data.

4.3.4 SAR Vs Lidar

SAR imaging projects all backscatter signals from a 3D world onto a 2D grid. Nevertheless, without further processing, the imagery does not contain elevation information. It corresponds only to the intensity of the signal received by the radar. Following to the formulation of the RCS the SAR map indicates mainly whether areas include: surfaces that are more or less oriented towards the radar and materials that are more or less reflective and if the scatterers are far or not. Thus, we wish to highlight the characteristic of SAR-based mapping in the context of robotics by comparing it with maps from other modalities. To do so, we propose a product that reproduces radar back-projected images mechanism using lidar data. It consists in an Orientation AGM that maps the amplitudes of incident angles coming from oriented surfaces within the radar FOV. It is created from the accumulated point cloud of the lidar and the FOVs of the radar along the trajectory. Basically, the algorithm is equivalent to a back-projection of the amplitude of the simulated received intensity obtained at each pose, without taking into account the reflectivity

of the materials, the radar antenna pattern, multipath effects or the radar-scatterer distance, etc. The steps followed to create such a product are :

- Creation of accumulated point cloud of the imaged scene by transforming them according to lidar-world transformation (cf. Figure 4.30)
- Downsampling of the accumulated point cloud
- Computation of the normals of each points using a Principal Component Analysis (PCA) based algorithm [Hoppe 1992]
- For each pose, evaluate which normals falls into radar FOV (cf. Figure 4.30)
- For those, compute the amplitude of the scalar product between the normals and the radar direction.
- Sum these amplitudes with their associated cell on a 2D grid.
- Normalize the grid using iterative averaging.

Urban Scenario First, this algorithm has been applied with lidar data from the same recording as the SAR images of figure 4.28 (same scene as figure 4.29) resulting in the grid map in figure 4.31. This product is interesting since it gives a qualitative upper bound of what a SAR image in our case should tends to be, a pseudo ground-truth. When comparing qualitatively SAR images and this product, we see that the high values of dot product are associated to strong amplitude values in the SAR image too. Nevertheless, it also enlighten the influence of the undesired effects (i.e. sidelobes) on the imagery compared to what it should look like. Within this scenario, such a comparison is helpful to clarify if artifacts in the SAR image are potentially due to multipath effects or actual real scatterers (i.e. walls behind windows or walkway). Finally, since radar and lidar are both active sensors, comparisons are interesting to understand and validate products from both, it is common in the aerial and satellite radar imagery to use lidar-derived product on a validation site to enhance, evaluate, analyse, adjust radar imagery [Tebaldini 2023, Huang 2021].

Field Scenario Second, we achieved the comparison with a dataset recorded in a field filled. The platform was following a path surrounded by tall dry grass, on Figure 4.32 only grass is visible in radar's FOV while on Figure 4.33 the radar was facing grass in the first plan and a metallic fence and tall trees in the background. For the context, Figures 4.34a and 4.34b show the lidar products on optical satellite image and a picture from the field respectively. From these experiments, we can state that the radar has probably the ability to see, at least partially, across such tall grass since scatterer responses can be seen even after a first patch of grass. Although, we cannot conclude on its ability to see the metallic fence since the strong responses may be due to the trees. Further experiments should be done to assess the perception capabilities of the radar in such environments, especially with a lidar that is at the same height of the radar (see Figure 4.32c) and with punctual metallic reflectors in the background. Nevertheless, the fact that SAR images admit similar regions of strong responses as the lidar product (using an

elevated lidar) is a promising result for potential applications of radar navigation within such environments. Thanks to its potential to see through grass, radar-based traversability could not only rely on traditional geometrical aspect used in pointcloud based traversability [Goldberg 2002] but also on semantic information as it is investigated using camera [Jiang 2022].

Finally, lidar is widely used in robotics, it offers outstanding results in localisation and mapping but often at the cost of a high amount of data to process. MIMO radar is becoming increasingly popular in this field and by working with the raw data, lidar like products, especially for mapping, can be targeted.

4.4 Conclusion

In this chapter, we introduced radar based mapping and presented our contributions related to this topic. First, we detailed SAR imaging strategy. Then, validated it first on a straight trajectory using ground-truth positioning with a 24 GHz radar. Next, we confirmed the process using velocity estimation instead of ground truth and assessed the impact on the imagery. Afterwards, the approach was successfully extended to both 24 GHz and 77 GHz sensors on a 2D planar trajectory with ground-truth positioning. We saw that using a sensor with a higher dynamic allows us to perform higher resolution images. We observed different impacts of the environment on the imagery such as constrained spaces or vegetation. Finally, we have demonstrated the ability to synthesise SAR images using radar-only odometry and seen the consequences on the mapping. The influence of the back-projection aperture has been discussed. Overall, the reconstructions are consistent with the shape of the buildings and the different scatterers. We assessed the characteristics of SAR based mapping by comparing it to a lidar product. From this, we can say that the SAR imagery, if built with a decent quality position estimation, can be a great asset for a robot cartography. The SAR images using 77 GHz recorded data have been done using the localisation and mapping library developed during this thesis shown in Appendix C.

To further the presented work, we could perform SAR imagery with diverse sensor placements and orientations, whether using a Front Looking configuration as it has been detailed in FL-SAR works [Franceschetti 2014, Farhadi 2019, Gishkori 2019, Albaba 2022b, Albaba 2022a, Reinecke 2024] or oriented toward the ground for example. Also, it could be interesting to leverage 3D information to work on traversability aspects to achieve truly autonomous navigation as it has been done with other sensors [Goldberg 2002]. This could be done via whether Interferometric SAR (InSAR) [Pieraccini 2001, Noferini 2006, Frey 2013, Mukaide 2021, Kabuli 2025], 3D SAR [Noegel 2024] or Tomographic SAR [Li 2022, Almutiry 2024, Guo 2024]. This could also improve the quality of the 2D imagery since for now we do not account for the elevation of the mapped scatterers while an elevation phase rotation applies azimuth phase rotation which imply errors of phase reconstruction, increasing mainlobes, etc.. Moreover, several

works exist on radar re-localisation on lidar maps [Yin 2020, Ma 2023, Ma 2024] and radar re-localisation on radar point cloud map [Cheng 2023b]. Could we extend this to target-based OGM or SAR AGM re-localisation on lidar maps with the presented lidar product in section 4.3.4 or directly on SAR maps ?

After presenting the work related to radar based mapping, the next chapter will be focused on radar target tracking.

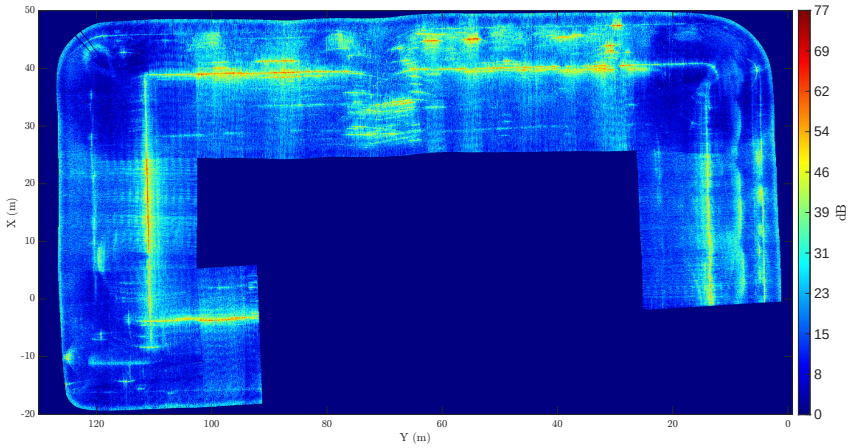

(a)

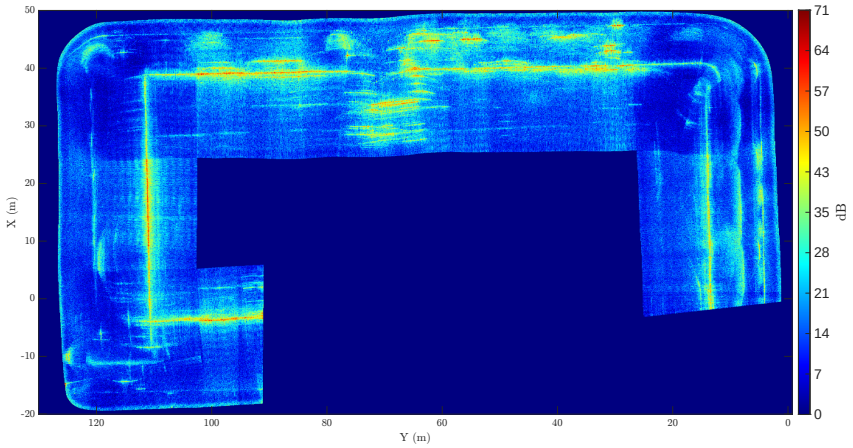

(b)

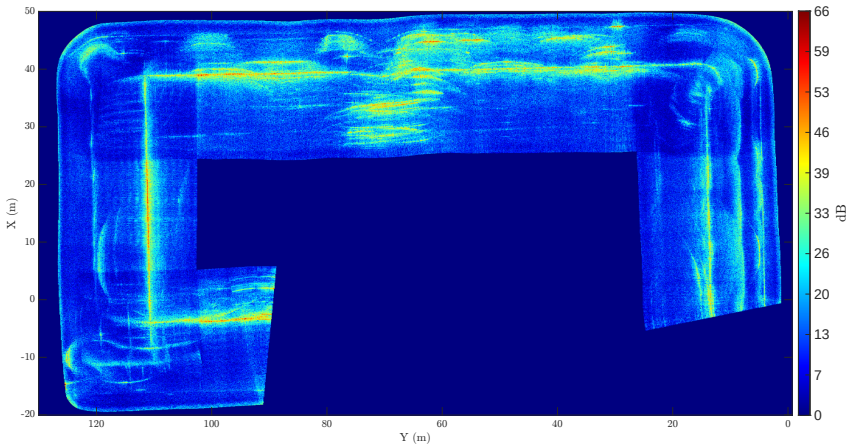

(c)

Figure 4.28: SAR images with $\theta_{a,proc}$ = a) 5°, b) 10° and c) 20°



Figure 4.29: SAR image ($\theta_{a,proc} = 2.5°$) super-imposed at a fixed altitude on Google Earth 3D map

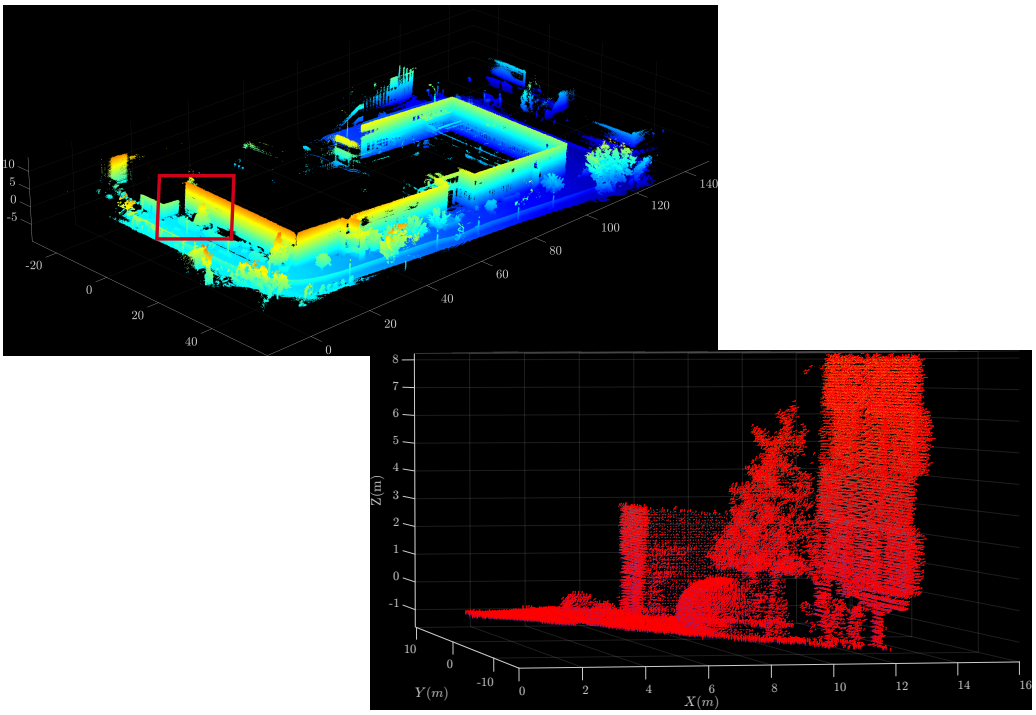

Figure 4.30: Accumulated pointcloud of the imaged scene and computed normals from points falling in radar FOV. Red square correspond to neighbourhood of the used radar FOV

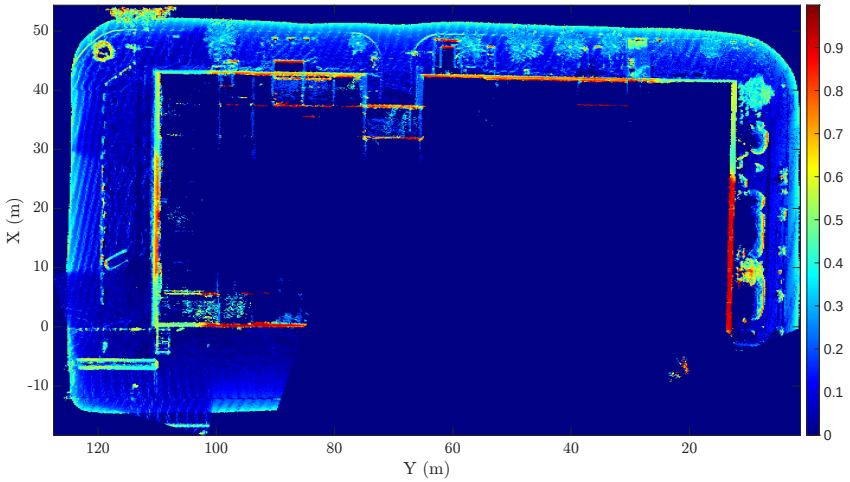

Figure 4.31: Lidar product corresponding to Orientation Amplitude Grid Map. Color corresponds to mean value of dot product between radar orientation and oriented surfaces

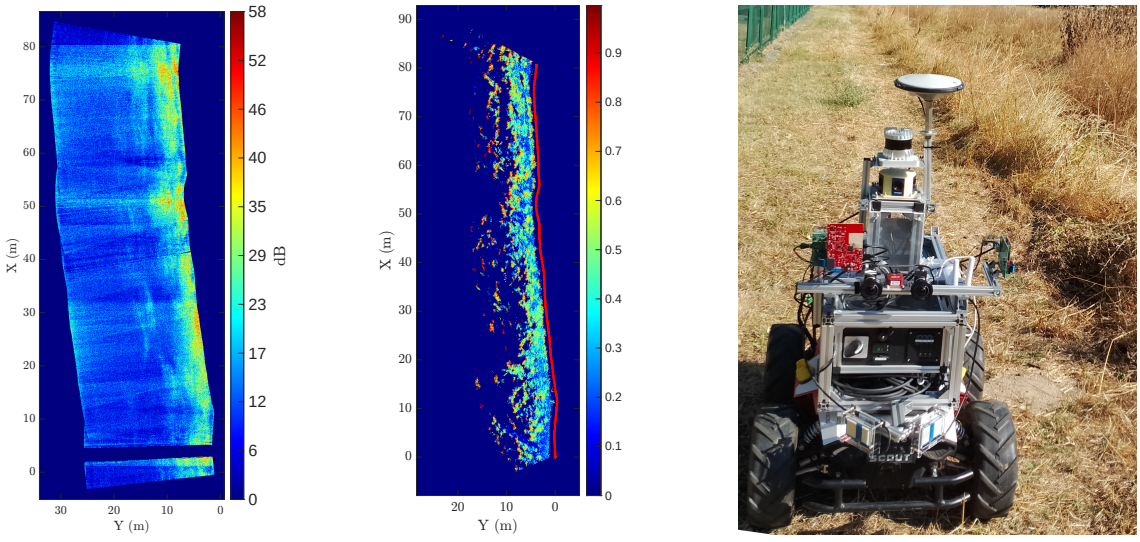

(a) (b) (c)

Figure 4.32: SAR and Lidar image in Field scenario $N°1$.
a) SAR image b) Normalized Lidar product. c) Used rover with mounted sensors

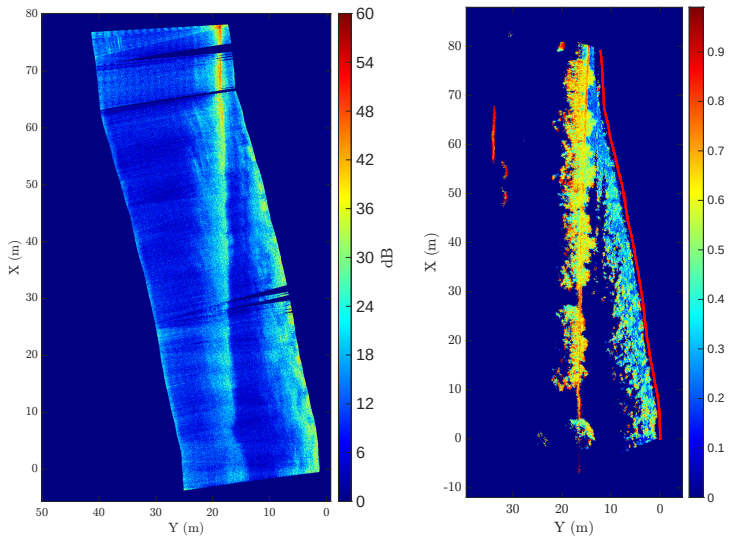

(a) (b)

Figure 4.33: SAR and Lidar image in Field scenario $N°2$.
a) SAR image b) Normalized Lidar product

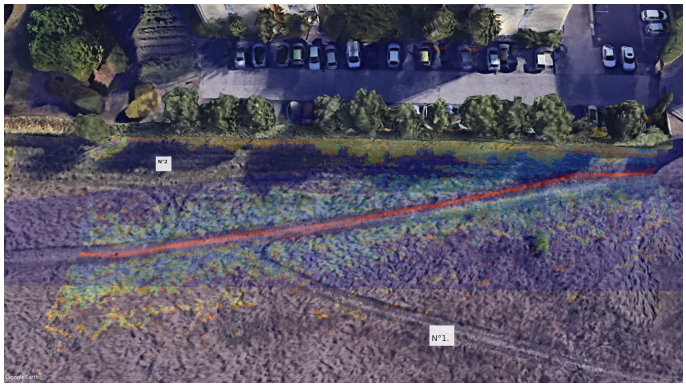

(a)



(b)

Figure 4.34: a) Superposition of Lidar product on optical satellite image for context.
b) Picture from the field, in the middle, the traversed path.

Chapter 5

Tracker

Contents

5.1 Radar ambiguity 87

5.2 State of the Art 89

5.3 Tracking approach 90

5.4 Validation of the Multi-Object Tracker 92

5.4.1 Validation via Simulation 93

5.4.2 Validation via Experiments 94

5.5 Conclusion And Perspectives 96

The radar sensor natively provides range, angle of arrival, and Doppler measurements which are interesting information for target detection and tracking. While the displacement estimation method presented in chapter 3 discards moving targets using RANSAC, this chapter also leverages the radar's inherent ability to detect mobile objects. We propose a fixed sensor tracking approach that resolves ambiguities of range-Doppler based detections, enhancing the robustness of target localization and motion analysis.

5.1 Radar ambiguity

As detailed in chapter 2 and as illustrated in figure 5.1, a radar sensor admits an ambiguity which, if not resolved, imply that every measurement is obtained modulo a certain multiplicity. Then, a radar measurement, to be correct, need to be associated with its correct current estimation domain. In our field, when using a radar, it is common to make the assumption that all measurements come from the principal estimation domain (where multiplicity of measurement is null). In this chapter, a method will be detailed to perform multiple object tracking of objects that are leaving the principal estimation, resolving their associated multiplicity of measurement in range, Doppler and angle.

Considering a radar signal $s(f, t, \theta, \phi) = Ae^{j\varphi}$, by sampling it, we then obtain $s(m, n, p, q)$. We can describe the variations of φ as a function of m, n, p or q by

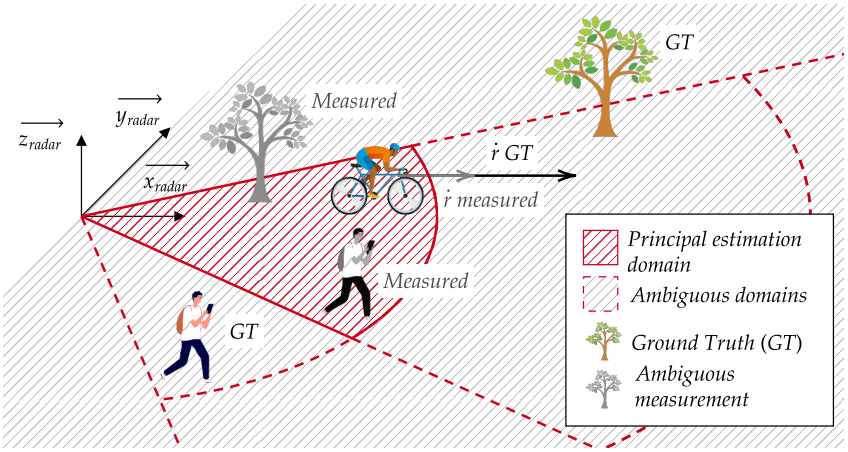

Figure 5.1: Radar measurement and its actual state in a classic scenario

fixing the other parameters, in the case of only one detection, such as:

$$\begin{cases} \varphi_r(m) & = & \varphi_0 + 2\pi m \frac{2B}{f_s T_{PRI} c} r \\ \varphi_{\dot{r}}(n) & = & \varphi_0 + 2\pi n f_c \frac{2T_{PRI}}{c} \dot{r} \\ \varphi_{sin(\theta)}(p) & = & \varphi_0 + 2\pi p f_c \frac{d_{az}}{c} sin(\theta) \\ \varphi_{sin(\phi)}(q) & = & \varphi_0 + 2\pi q f_c \frac{d_{el}}{c} sin(\phi) \end{cases}, \tag{5.1}$$

Where r, $\dot{r}$, θ, ϕ, φ_0, d_{az} and d_{el} are respectively the range, radial velocity, angle in azimuth and elevation associated to the object, the constant phase term and the inter-element spacing in azimuth and elevation. We can then write that for whether $x = r, \dot{r}, sin(\theta), sin(\phi)$, we have:

$$\varphi_x(u) = \varphi_0 + 2\pi u \alpha x. \tag{5.2}$$

Given the Nyquist-Shannon sampling theorem, it is clear that the phase variation associated with a variable must follow $\alpha x < 1$. We can thus define $\Delta x_{amb} = \frac{1}{\alpha}$ as the scope of the current estimation domain. The actual state x can then be estimated from the measured state x_A (using the subscript A for ambiguous), and a relative integer m_x, called the ambiguity multiplicity in state x, such that:

$$x = x_A + m_x \Delta x_{amb}. \tag{5.3}$$

where $m_x \in \mathbb{Z}$.

By describing radar ambiguities in this way, using the offset x_{ref}, we can define a centered estimation measurement domain such that:

$$-\frac{\Delta x_{amb}}{2} \leqslant x - x_{ref} \leqslant \frac{\Delta x_{amb}}{2}. \tag{5.4}$$

Then it appears that $\frac{\Delta x_{amb}}{2}$ is the frontier of the current estimation domain. Then the scope of the domains in range, radial velocity and angles is given in equation

5.5

$$\begin{cases} \Delta r_{amb} & = & \frac{f_s c}{2BPRF} \\ \Delta \dot{r}_{amb} & = & \frac{\lambda PRF}{2} \\ \Delta sin(\theta)_{amb} & = & \frac{\lambda}{d_{az}} \\ \Delta sin(\phi)_{amb} & = & \frac{\lambda}{d_{el}} \end{cases} . \tag{5.5}$$

5.2 State of the Art

Radar ambiguity resolution is a common topic and can be divided into two types, the use of specific signals or the use of specific algorithms. With regard to the former, there are works based on the use of different PRFs to resolve the ambiguity in range, Doppler and angle. Numerous studies [Gonzalez 2019] [Cao 2020] [Kronauge 2010] are based on the use of the Chinese Remainder Theorem with particular PRFs to achieve ambiguity resolution. Ferrari *et al.* [Ferrari 1997] present a different way to solve Doppler ambiguity relying on the folded frequency estimates for each PRF and a quasi-maximization of a likelihood criterion for ambiguity order estimation. To use a low cost off-the-shelf radar, we won't be able to rely on methods using specific signals. We will therefore deal with algorithm-based methods only. Zhou *et al.* [Zhou 2007] proposed a method using amplitude information to remove the ambiguity of range and Doppler measurements. Li *et al.* [Li 2013] have developed a multiple-target tracking system using an Unscented Kalman Filter (UKF) combined with a Multi-Hypothesis Tracker (MHT) and a Probabilistic Association (PDA) that removes ambiguity of the radial velocity estimate. The UKF admits a modified unscented transform and a maximum likelihood estimator for calculating the measurement prediction. In the probabilistic association algorithm, a Bayesian process is used to evaluate the probability of measurement ambiguity, so that several measurement ambiguities can be tested. Finally, in the MHT, a 3D assignment is implemented to realize the association between measurement, tracks and ambiguity. Shin *et al.* [Shin 2023] presented a method using interacting multiple models (IMMs) each testing a multiplicity so as to remove ambiguity in radial velocity, particularly at low SNR. These last two works can be gathered in the category of ambiguity resolution by track-before-resolving which, as its name indicates, will first initialise and update tracks and then estimate the measurement ambiguity as it goes along. This allows measurement ambiguity to be resolved for targets that have been observed for the first time outside the radar's unambiguous field of view.

The work presented in this chapter explains the multi-object 3D tracking approach implemented and the ambiguity resolution in the case of targets initially seen in the radar's principal domain of estimation. Our main contributions are the resolution of ambiguity using Extended Kalman Filter using a Constant Velocity, Constant Heading (CVCH) 3D model, the management of multiple tracks by a Bayesian process, as well as the detection using a combination of a foreground detector and a modified Constant False Alarm Rate (CFAR) Detector.

5.3 Tracking approach

This section deals with our proposed tracking algorithm and ambiguity resolution method. We propose an Extended Kalman Filter (EKF) based tracking approach taking into account the ambiguities directly in the association step with innovation monitoring. For that purpose, we propose to use a Maximum Likelihood Estimation (MLE) to select the most credible data association for each track based on unambiguous innovation ranking. In the following experiments, the radar is supposed to be static.

Each track will be represented by an equivalent state vector $\mathbf{x}_k = [x_k, y_k, z_k, \beta_k, \alpha_k, V_{l,k}]$ composed of the object 3D position (x_k, y_k, z_k), its yaw and pitch (α_k, β_k) and its linear velocity $V_{l,k}$. The complete state vector to be estimated can be composed of M multiple mobile targets such as: $X = [\mathbf{x}^1, \ldots, \mathbf{x}^M]$.

Motion Model Since we can't estimate any acceleration or the angular velocity of an object, the chosen motion model is a 3D constant velocity, constant heading (CVCH) given by equation 5.6.

$$\hat{\mathbf{x}}_{\mathbf{k|k-1}} = \hat{\mathbf{x}}_{\mathbf{k-1|k-1}} + \begin{pmatrix} \cos(\beta_{k-1})\cos(\alpha_{k-1})V_{l,k-1}dt \\ \cos(\beta_{k-1})\sin(\alpha_{k-1})V_{l,k-1}dt \\ \sin(\beta_{k-1})V_{l,k-1}dt \\ 0 \\ 0 \\ 0 \end{pmatrix}. \tag{5.6}$$

Measurement Model A classic spherical to Cartesian measurement model is used with the specificity of radial velocity prediction. We then obtain the expected measurement $\hat{\mathbf{z}}_\mathbf{k}$ at time k from the predicted state $\hat{\mathbf{x}}_{\mathbf{k|k-1}}$ with following equation 5.7

$$\hat{\mathbf{z}}_\mathbf{k} = \begin{pmatrix} r \\ \theta \\ \phi \\ \dot{r} \end{pmatrix} = \begin{pmatrix} \sqrt{x^2+y^2+z^2} \\ \text{atan2}(y,x) \\ \arcsin\frac{z}{r} \\ V_l(\cos\theta\cos\beta\cos(\alpha-\theta)+\sin\phi\sin\beta) \end{pmatrix}. \tag{5.7}$$

Data association with Ambiguity resolution It is common to carry out the track-measurement association to use Munkres algorithm The association cost matrix used is then calculated using the Mahalanobis distance d_{mah} between the measurement and its prediction. Upstream, a gating operation is performed to discard track-measure associations with a distance that do not pass a chi-square test. Nevertheless, in the case of ambiguous measurements, such a test can fail due to the ambiguity of measurement.

The ambiguity resolution is based on the comparison of each measurement with the prediction of each track. To calculate each Mahalanobis distance of the innova-

tions, we use the multiplicities of the estimated state in range, radial velocity and angles corresponding to the maximum likelihood between a measurement and the predictions of each track. This operation is described in equation 5.8.

$$\begin{array}{lcl} \mathbf{y}_u & = & \arg\min_{\mathbf{m}} \left[\left(\mathbf{z_k} - \mathcal{T}_{\mathbf{m}}\left(\mathbf{h}(\hat{\mathbf{x}}_{\mathbf{k|k-1}})\right)\right)\right] \\ d_{mah,u} & = & \mathbf{y}_u^\top S^{-1}\, \mathbf{y}_u. \end{array} \tag{5.8}$$

with $\mathcal{T}_{\mathbf{m}}(\hat{\alpha}) = \hat{\alpha} + m_\alpha \Delta\alpha_{amb}$ comes from equation 5.3.

Such modification of the Mahalanobis distance ensures that the association will always be performed in the valid estimation domain. The result of such processing is that all the tracks will be first initialized in this principal domain even if the first detection is issue from an object outside the principal estimation domain. The resulting assumption is that each new track start from the non ambiguous domain.

Multi-target management When dealing with multiple tracks, the classical Munkres approach could fail making wrong associations and so lose or confuse the tracks. To solve such problems, JPDAF- [Fortmann 1983] and MHT-type [Blackman 2004] algorithms can be considered as optimal solutions for track management. Nevertheless, they are computationally expensive and burdensome to implement.

To simplify the approach, we propose a simple Bayesian process for track management. This method makes use of the Bayes' rules for updating the probability of existence of each track. It can be summarized as follows: first, a track is created for each unassigned observation with an initial probability of existence. Then, if a track is assigned to a given observation, its probability of existence will tend to increase. If a track is not matched to an observation, its probability of existence will decrease. If a track has too low probability of existence, it will no longer be able to have an assigned observation and will die. The update rules for the probabilities of existence are given in equation 5.9:

$$p(t \mid d) = \frac{p(t)p(d \mid t)}{p(d \mid t)p(t) + p(d \mid \bar{t}))(1 - p(t))}. \tag{5.9}$$

where $p(t \mid d)$ is the updated probability of existence of track t given an associated detection d, and $p(t \mid \bar{d})$ is the updated probability in case there is no associated detection. $p(t)$ is the a priori probability of existence of the track. Finally, $p(d \mid t)$, $p(d \mid \bar{t})$ and $p(\bar{d} \mid t)$ are linked to the radar observation model and represent respectively the true positive (TP), false positive (FP), false negative (FN) rates of the detector. Note that such rates have to be estimated depending on the radar used. With such an approach, even if a wrong association occurs at a given step, the corrupted track will die and a new one representing the real object will be created. Post-processing could then be launched to recover the global real track.

Custom range-Doppler detector To detect the targets of interest in the radar's scene, a combination of two classic algorithms was used: a foreground detector

[Stauffer 1999] and a Constant False Alarm Rate (CFAR) [Richards 2010a](see section 2.6.1) detector. Each detector are used on a range-Doppler map. The final detections used correspond to the multiplication of the two detector's masks.

The foreground detector models each cell of the scene background with a mixture of several Gaussian distributions. The objective of this detector is to keep only moving targets while removing static ones. This first step has been done to remove the anomalies observed on the range-Doppler map (targets with a constant radial velocity, range and SNR over the radar frames).

The Cell Averaging-CFAR (CA-CFAR) detector is then used to refine the detections of the foreground detector. We implemented the CA-CFAR with a convolution operation to reduce its computational cost. Note that with the CA-CFAR mask, the larger the kernel, the more of the range-Doppler map border will not be analysed. To alleviate these problems, we apply convolution to a replicated range-Doppler map as shown in figure 5.2. This method makes even more sense in the presence of ambiguous range targets: their impact is taken into account to the right and left of the map when the latter is at the edge. The results of these two algorithms are illustrated in figure 5.3.

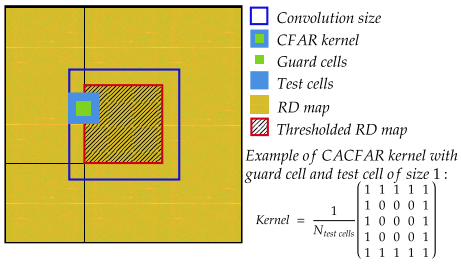

Figure 5.2: CA-CFAR on replicated range-Doppler maps

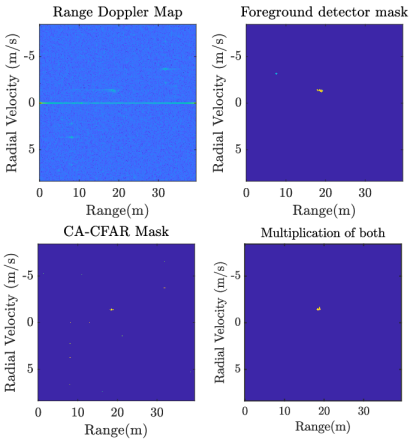

Figure 5.3: Detection results. Input is the upper left map

5.4 Validation of the Multi-Object Tracker

To prove the efficiency of our solution, we propose two experimental setups for testing the algorithms with both simulated and real data. The first setup is a simulation that allows us to experiment the tracker with several mobile objects having different ambiguous configurations. This simulation is performed with several targets moving at different velocities with different trajectories starting and evolving inside and outside of the principal estimation domain. Then, experiments has been performed with a real radar observing different rovers.

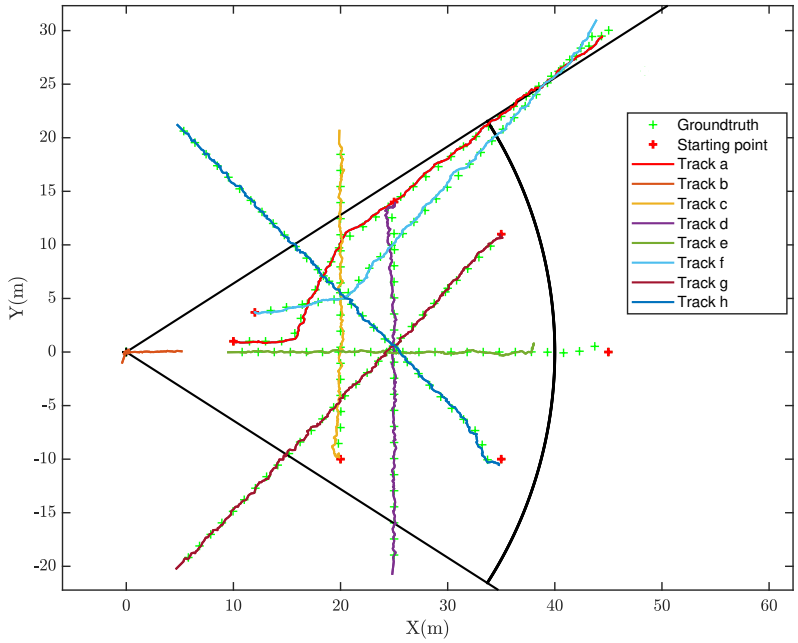

Figure 5.4: Simulated scenario with the ground-truth and estimated trajectories

5.4.1 Validation via Simulation

Simulated data The trajectories of different targets have been simulated to get observations $\mathbf{z} = [r, \theta, \phi, \dot{r}]$. Gaussian noise exceeding the sensor's theoretical resolution has been added to the observations. In addition, the measurements were sampled according to the radar used and limited to values corresponding to the principal estimation domain. This was done to simulate the sensor's behaviour as closely as possible and to evaluate the ambiguity resolution. The following standard deviations for the noise applied to measurements were used : $\sigma_r = 0.2$ m; $\sigma_{\hat{r}} = 0.2$ m.s^{-1}; $\sigma_\theta = 0.7$ deg; $\sigma_\phi = 0.7$ deg.

We simulated 7 moving targets in the scene with their respective trajectories and velocities profiles. This scenario can be seen in Figure 5.4

Simulation results As shown in figure 5.4, the simulation validated the tracker's operating principle and confirmed the removal of ambiguity in range and azimuth for tracks starting in the unambiguous field of view. Furthermore, the tracker was shown to be robust to the crossing of multiple trajectories. Indeed, tracks d, g and h were found to cross around the point $(25, 0)$ within the same time interval, without the tracker misinterpreting this crossing. Also, tracks b and e correspond to the measurements of the trajectory starting at point $(45, 0)$, i.e. ambiguous at the start. Track b (the only one passing by the origin) is no longer updated, notably because the multiplicity tests required to assign observations to this track would be outside the radar's field of view (negative x). So a new track is created, consistent with the ground truth.

5.4.2 Validation via Experiments

Real data recording was carried out using the K-MD2 24GHz FMCW radar, it is a 3D capable 1Tx-3Rx radar, shown in figure B.1d. Position accuracy using our reference system (GNSS/inertia/wheel odometry fusion) is ~ 40 cm. The radar was static and the considered mobile targets were rovers shown in figure 5.5, moving at a maximal speed of 1.5 m.s^{-1}. In the used configuration, the radial velocity resolution of the sensor is $V_{r,res} = 6$ m.s^{-1} and the range resolution is $r_{res} = 15$ cm.



Figure 5.5: Tracked targets - 2 Agilex Scout from ONERA/DTIS Toulouse

Range and Azimuth Ambiguity To test the range and azimuth ambiguity resolution, a first experiment with a single moving object has been done. The robot executed two different paths, the first one is a straight line, the second one a loop. On both results, the trajectory estimated by the EKF is the red line and the measurements obtained by the radar are in blue for inside and outside principal estimation domain measurements. Figure 5.6 shows the results for the line experiment. In this case the robot starts at the position $(15, 0)$ and moves to $(60, 0)$. We can observe that the measurements admit a non-null range multiplicity after 40 m but the robot is still well tracked.

The second experiment has been designed to check the robustness to azimuth ambiguity. Figure 5.7 shows the ambiguity resolution in azimuth, with a clear angular jump in the radar data once the robot exits the principal estimation domain at coordinates $(17, 4)$. Nevertheless the trajectory estimated remains valid.

Multiple target tracking To deal with multiple tracks, we performed another experiment with two robots following each-other on a straight trajectory. The EKF based tracker estimates their positions, pitch, yaw and linear velocity using the algorithm described above. The robot estimated trajectories are displayed in green and yellow. The ground truth trajectory of both robots obtained thanks to GNSS/IMU/wheel odometry fusion are provided in red. The trajectories obtained

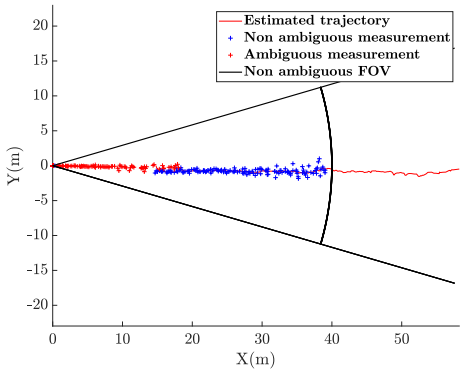

Figure 5.6: Range ambiguity resolution

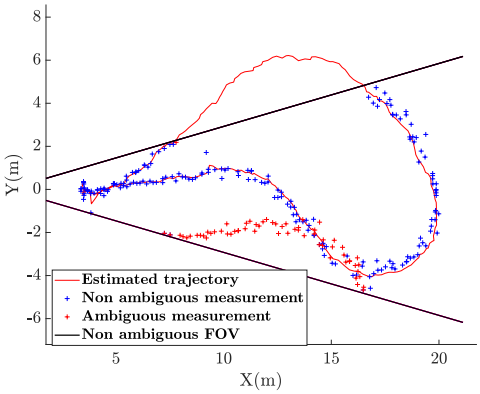

Figure 5.7: Azimuth ambiguity resolution

for the detected tracks with an existence probability of at least 0.90 are presented in Figure 5.8. During this experiment, we also monitored the probability of existence of each track. These results are presented in Figure 5.9. We can see that during the experiment, multiple wrong detections were made. Each new detection created a new track in case it was not associated with an existing track. Nevertheless, thanks to our Bayesian approach, only the two tracks corresponding to the trajectory of the two rovers maintain a high level of probability of existence.

We can notice two wrong tracks in blue and purple at the beginning of the second robot trace. The probability of existence of the two tracks can also be observed on figure 5.9. These tracks are due to missed detections occurring at the beginning of the experiment. Nevertheless these tracks are quickly managed by the Bayesian process.

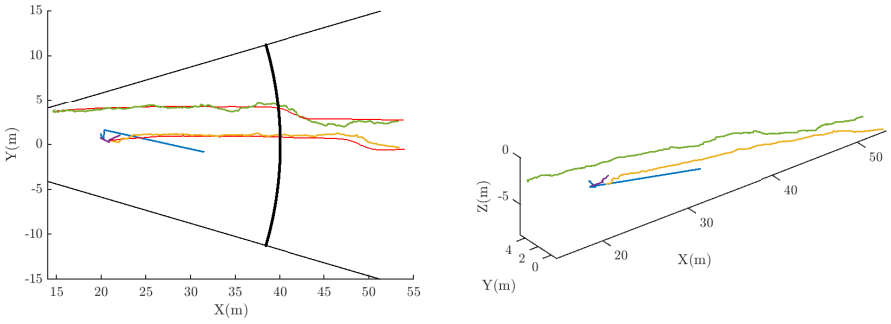

Figure 5.8: Estimated 2D and 3D trajectories of tracks having at least exceeded a probability of existence of 0.90. Red tracks in the XY plane are the ground truth. Other tracks match their colors with the one in Fig. 5.9.

The root mean square errors (RMSE) in x, y and z direction between radar estimation and GNSS/inertia/wheel odometry fusion are respectively: $\epsilon_x = 0.99m$, $\epsilon_y = 0.32m$ and $\epsilon_z = 0.12m$. The global positioning error is $\epsilon = 0.605m$.

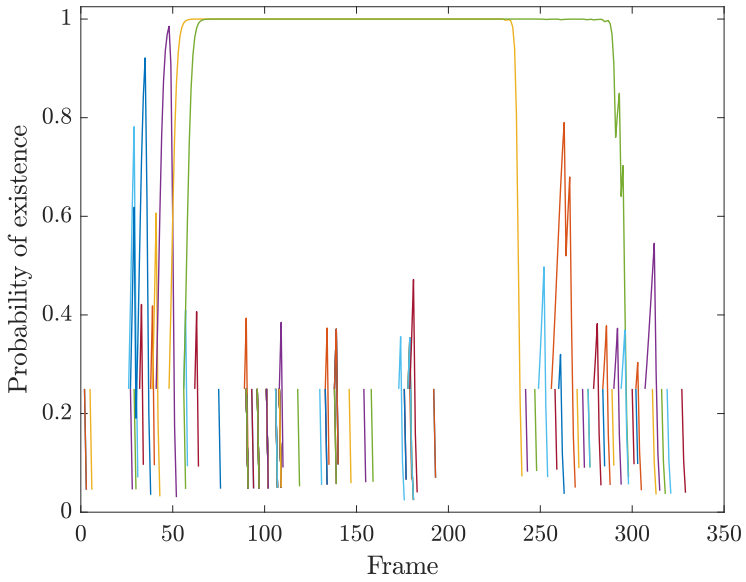

Figure 5.9: Probability of existence of each track at each iteration. Tracks that are not crossing a probability level of 0.5 are generally due to false detections. Only two tracks, the ones corresponding to the rovers, maintain a high level of probability of existence.

5.5 Conclusion And Perspectives

In this chapter, we presented a multi-object 3D radar-based tracking approach in the presence of range, Doppler, and angle of arrival ambiguous measurements. We demonstrated the tracker's ability to estimate the 3D position, heading and linear velocity of multiple targets even in the case of crossing trajectories. We explained the ability to solve the problem of measurement ambiguity during the data association phase by using a new step in the innovation process. A comprehensive study on simulated and real data was carried out to demonstrate the performance and limitations of our method with different radar scenes. We showed good 3D tracking performance with an RMSE of 0.6m when tracking two moving targets travelling a total of more than 70m. Using simulated data, we have demonstrated the behaviour of the tracker when a target is first detected outside the principal estimation domain. This work has been published and presented at IRS 2024 [Tyack 2024]. These results open several potential paths for improving and further developing the method. A comparative study could be conducted to evaluate the trade-offs between computation time and state estimation accuracy for our Bayesian track management versus Multi-Hypothesis Tracking and Interacting Multiple Model methods. The method could be extended to resolve ambiguities not only within the principal estimation domain. It could be achieved, for example, by combining the measured range with the SNR, or by using a track-before-resolve approach that assigns a probability of existence across a finite set of estimation domains. Finally, one of the most promising directions would be to integrate this type of algorithm into a SLAM

framework, enabling Simultaneous Localization and Mapping with Multiple Object Tracking. This would extend the studies conducted in this thesis to scenarios in the context of a non-static environments.

Chapter 6

Conclusion And Perspectives

6.1 Conclusion

In this thesis, the goal was to outline the purpose and stakes of both coherent and non-coherent radar processing in the context of mobile robotics especially for self-localisation, object tracking and mapping. We detailed strategies combining raw data and pre-processed pointcloud to obtain a radar-only navigation solution.

We started by introducing the radar as an exteroceptive sensor having distinctive features that motivates its use in navigation. Indeed, this sensor is almost insensitive to working conditions limiting traditional sensors and can measure object's 3D position, reflectivity and relative radial velocity. Unfortunately, its spatial measurement is quite sparse and noisy in particular when considering non-coherent pointcloud processing leading to the use of coherent methods such as SAR imagery for mapping purpose.

To do so, we had to propose a localisation solution. We have first detailed a pointcloud based single-scan 2D odometry relying on Doppler-Angle Regression embedded in an Implicit Extended Kalman Filter. We have shown that for localisation purpose it is interesting to use a front-facing radar while for SAR mapping, a side-looking one is preferred. Therefore, we used a multi-radar setup and proposed a study on radar-vehicle calibration also relying on the IEKF. We presented an observability analysis for optimal sensor placement taking into account both velocimetry and calibrability. The results associated to these contributions have been given and outline a strong translation estimation, interesting calibration performances but a poor rotation estimation. Then, we proposed a raw data based scan matching strategy dedicated to rotation estimation. It is driven by AKAZE feature detection and association for range-azimuth map matching and on RANSAC-Kabsch algorithm for the rotation matrix computation. It has been tested on recorded data and admits potential for SLAM applications. Finally, we proposed to rely, solely on pre-processed pointcloud using Doppler-Angle Regression for translation estimation and KISS-ICP for rotation estimation. This strategy yields to a localisation that can be used for SAR imagery. This solution and the work done on range-azimuth map feature matching are part of the localisation and mapping library developed during this thesis shown in Appendix C. These studies are all gathered within the Chapter 3.

Afterwards, we have seen the works done on mapping, especially using SAR methods. We started by detailing the main motivation: obtaining a high-resolution grid mapping obtained by synthesising a wide virtual array along the trajectory.

From the state-of-the-art we have seen that the peculiarity of our contribution lies on the use of on-the-shelf, low-end radar-only sensor suite. We detailed the results of our TDBP-based SAR mapping on linear, then, non-linear trajectories, using 24 GHz and 77 Ghz sensors, relying on ground-truth and odometry localisation. We discussed the differences obtained under these different conditions but also considering some parameters. In addition, we proposed a lidar product based on backprojection algorithm resulting in an orientation amplitude grid map. Such product allows to compare coherent radar- and lidar-based grid mapping to not only visualise their similarities and differences but also enables, in some cases, to better understand SAR based mapping. The SAR imagery algorithm is part of the developed localisation and mapping library developed during this thesis shown in Appendix C. These contributions are detailed in Chapter 4.

Finally, in Chapter 5 a multi-object radar tracker in the context of measurement ambiguities have been proposed. The EKF-based tracker estimates position, heading, and velocity of multiple targets, including crossing trajectories, by resolving measurement ambiguity within the data association phase. Real and simulated experiments validated the approach and showed correct the behavior when targets first appear inside or outside the principal estimation domain.

6.2 Perspectives

There are numerous possible avenues for further research, which can be grouped into different categories.

Simulation To properly improve and prototype new imaging algorithms it would be useful to dive first in the creation of simulated data. This not only allows for complete control over the type of case to be studied, radar parameters, environment, and noise, but also provides access to the ground truth of the trajectory, the imaged scene, and the states to be estimated. A 3D simulator would be particularly interesting to evaluate imaging algorithms based on interferometry and tomography. Conventional open-source robotics simulator such as Gazebo, Carla and AirSim [Koenig 2004, Dosovitskiy 2017, Shah 2017, Giovagnola 2023] propose 3D and velocity radar pointcloud but do not support raw FMCW radar data generation. One potential candidate for our application could be RadarSimX [RadarSimX 2019], it admits a good modularity, and simulates raw FMCW MIMO radar data from point targets and 3D models. Would it be possible to combine this simulator for radar data generation with one of the conventional robotic simulators to carry out realistic multi-sensor simulations ? Finally, as a first step in the sim-to-real process, it would be interesting to study the creation of a semi-synthetic dataset based on lidar data. The lidar point cloud provides high-resolution spatial information, but also the reflectivity of each point, potentially enabling a detailed simulation of radar measurement with a certain degree of control over added noise. This type of dataset could enable the prototyping of algorithms on data that are more realistic

than that obtained from simpler simulations, while still providing access to pseudo ground truth for evaluation.

Localisation Future work could explore in what extent the addition of radar information such as range and RCS information may improve calibration and localization accuracy and enable extension to 3D estimation. Also, fusion with complementary sensors like IMU or monocular camera represents another promising direction. Thanks to the integration of a gyroscope or a visual factor, the angular estimation deficit we observed could be resolved. On the SLAM side, several enhancements are worth investigating: autofocus [Balducci 2023] and feature matching for raw radar data, and loop closure [Zhuang 2023, Lubanco 2024], Doppler- and RCS-weighted, or segmented ICP within point cloud processing pipelines [Herraez 2024, Kim 2024b, Herraez 2025]. Then, a systematic benchmark comparing these localization approaches, in the same way as Kubelka *et al.* [Kubelka 2023], that questioned the usefulness of former state-of-the-art scan-matching techniques in radar pointcloud based odometry via testing several coherent and non-coherent techniques using different radars on diverse environments. It would be helpful to not only rely metrics such as absolute and relative trajectory errors but also on computational cost, and observability for different radar types and scenarios. Finally, in the continuity of the existing radar-based re-localisation studies [Yin 2020, Ma 2024], several new approaches could be investigated, among them, we can cite SAR based re-localisation on lidar grid maps and pointcloud OGM on SAR based map.

Mapping Extending the current mapping work to 3D through interferometry [Kabuli 2025] or tomography is a promising direction. If open source datasets and SAR codes become available, it would be relevant to propose benchmarks. Whether based on global metrics such as entropy, whether via local pixel-wise RMSE. Also, it would be interesting to examine if the lidar products presented could serve as a practical ground truth for SAR imagery evaluation. Following Grebner *et al.* [Grebner 2022b], who compare detection based OGM and SAR grid map, it would be valuable to broaden this comparison to other construction methods such as range-azimuth based maps, and to establish quantitative benchmarks for evaluating these approaches. The question of the extent to which radar occupancy grid and SAR grid maps can be considered equivalent for localisation purposes to those used by traditional exteroceptive sensors also remains open and warrants further investigation. Finally, we have demonstrated that 2D SAR imagery is suitable within a lightweight odometry and mapping framework, although the feasibility of performing autofocus-based SLAM and 3D interferometric or tomographic mapping in real-time still remains an open question.

Appendix A

Radar Processing Details

A.1 Compensation of Phase Errors in TDM MIMO Radar

The Time Division Multiplexing is a chirp emission method, probably the most obvious one since it relies on using one emitting element at a time so that they don't interfere. Compared to other existing methods, Frequency Division Multiplexing (FDM) and Code Division Multiplexing (CDM), the drawbacks are that it requires to sample more data and that it increases repetition period. Also, we will see in this section that we need to take into account this emitting scheme in the angle of arrival estimation since it creates phase errors between each sub-arrays when dealing with moving targets (equivalently moving radar).

In section 2.4, we have seen that the mixed signal, when taking into account the Doppler effect, can be written as:

$$S_{re}(t) = \sum_k a_k e^{-j\omega_k} e^{j2\pi f_{d_k} t}. \tag{A.1}$$

As illustrated in figure A.1, by re-writing for two sub-arrays and accounting for the delay of emission, for one scatterer we have:

$$\begin{aligned} S_{re,\mathrm{T}_0}(t) &= a_0 e^{-j\omega_0} e^{2\pi f_d t}. \\ S_{re,\mathrm{T}_1}(t) &= a_0 e^{-j\omega_0} e^{2\pi f_d t + \delta} \\ &= a_0 e^{-j\omega_0} e^{2\pi f_d t - 2\pi f_d \frac{T_{PRI}}{3}}. \\ S_{re,\mathrm{T}_2}(t) &= a_0 e^{-j\omega_0} e^{2\pi f_d t + 2\delta} \\ &= a_0 e^{-j\omega_0} e^{2\pi f_d t - 2\pi f_d \frac{2T_{PRI}}{3}}, \end{aligned} \tag{A.2}$$

with S_{re,Tx_0} and S_{re,Tx_1} the common part of the signal received by the elements of sub-array related to Tx_0 and Tx_1 respectively. Generalizing for n_T emitting elements, we have:

$$S_{re,n_T}(t) = a_0 e^{-j\omega_0} e^{2\pi f_d t - 2\pi f_d \frac{n_T T_{PRI}}{N_T}}, \tag{A.3}$$

with N_T the number of sub-arrays (fixed sample). In figure A.2a is illustrated the classic radar cube formation acquired with a 3TX-3RX full-array. Then, the varying phase of the signal on a chirp-antenna slice of a cube with N_T sub-arrays

(fixed sample) can be written as :

$$\begin{array}{c} \\ \text{Sub-array T}_0 \\ \\ \text{Sub-array T}_{n_T} \\ \\ \text{Sub-array T}_{N_T-1} \end{array} \begin{array}{c} \begin{array}{ccc} \text{Chirp}_0 & & \text{Chirp}_{N_c-1} \end{array} \\ \begin{bmatrix} \phi_d & \dots & \phi_d(N_c-1) \\ \vdots & \vdots & \vdots \\ \phi_d - \omega_d \frac{T_{PRI}}{N_T} n_T & \dots & \phi_d(N_c-1) - \omega_d \frac{T_{n_T PRI}}{N_T} \\ \vdots & \vdots & \vdots \\ \phi_d - \omega_d \frac{T_{PRI}}{n_T}(N_T-1) & \dots & \phi_d(N_c-1) - \omega_d \frac{(N_T-1)T_{PRI}}{N_T} \end{bmatrix} \end{array}, \tag{A.4}$$

with $\phi_d = 2\pi f_d T_{PRI}$. When we will perform an angle DFT (column-wise), we can clearly see the sub-array to sub-array shift on the estimated angle. In [Bechter 2017], Bechter *et al.* propose to perform an interlaced zero-padding in the Doppler dimension to tackle this issue. The resulting data cube is illustrated in figure A.2b and the varying phase on a chirp-antenna slice gives:

$$\begin{array}{c} \\ \text{Sub-array T}_0 \\ \\ \text{Sub-array T}_{n_T} \\ \\ \text{Sub-array T}_{N_T-1} \end{array} \begin{array}{c} \begin{array}{cccc} \overbrace{\qquad\qquad\qquad\qquad\qquad\qquad}^{\text{Chirp}_0} & & & \overbrace{\qquad}^{\text{Chirp}_1} \end{array} \\ \begin{bmatrix} \phi_d & 0 & \dots & 0 & 2\phi_d & \dots \\ 0 & \phi_d - \omega_d \frac{T_{PRI}}{n_T} & \dots & 0 & 0 & \dots \\ \vdots & \dots & \ddots & \vdots & \vdots & \dots \\ 0 & 0 & \dots & \phi_d - \omega_d (N_T-1)\frac{T_{PRI}}{n_T} & 0 & \dots \end{bmatrix} \end{array}. \tag{A.5}$$

In figure A.3 is illustrated the result of this technique on Capon beamformed Range Azimuth maps.

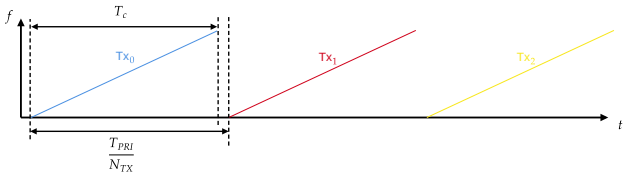

Figure A.1: TDM MIMO emitting scheme with 3 Tx

From this, we can conclude that in the case of whether non-static environment or a moving radar, it is important to take into account motion induced phase errors due to Time Domain Multiplexing emitting scheme. The processing involved are not heavy and crucial for decent state estimation and mapping.

A.2 Data Acquisition

When dealing with raw data, it is important to have in mind the type of data recorded, whether real or complex. In figure A.4 is illustrated the real and complex acquisition architecture. The real one rely on a single mixer and ADC implying

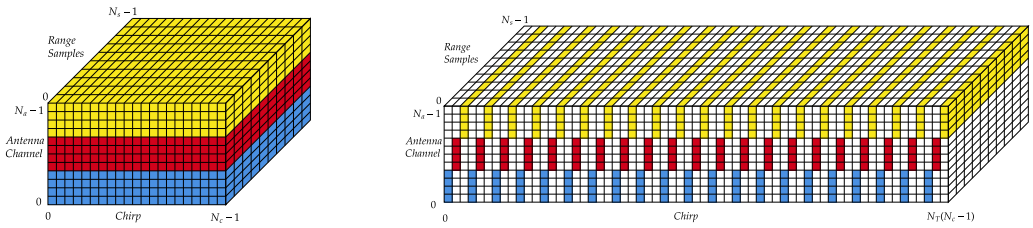

(a) (b)

Figure A.2: Raw Data Cube a) with and b) without interlaced zero-padding in chirp dimension for TDM motion compensation . The colours denotes the signals associated to different sub-arrays

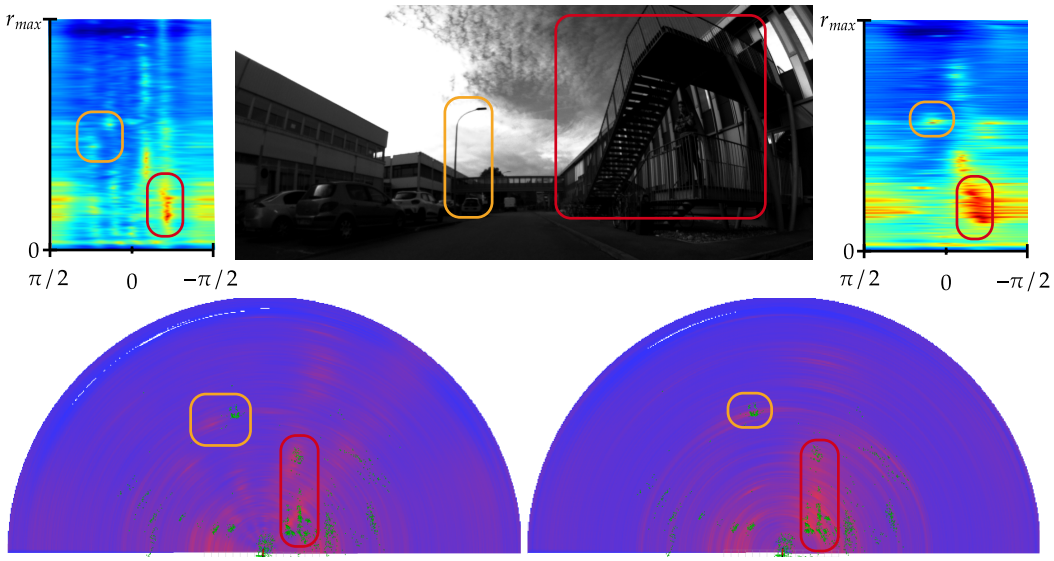

Figure A.3: Polar and Cartesian Range Azimuth Maps without (left) and with (right) TDM phase errors compensation. The green dots on the Cartesian maps are CFAR detections from phases compensated signal. Boxes are showing some salient features in the radar FOV like metallic stairs and pole

on the acquisition of only the In-phase (I) signal while the complex architecture thanks to a phase shift and a second ADC and mixer can record both In-phase and Quadrature signal (IQ). From this, we can list these differences between the two architectures and the consequences associated:

- Physically, the main difference rely on the noise level of the recorded IF signal. The receiver admits a certain frequency band centered at the local oscillator frequency and is composed of the in-band signal (containing the signal of interest) and the image band (containing only thermal noise). Using a real architecture, the IF signal sampled will give us a spectrum that is composed of both negative and positive frequencies, we need to decimate half of the samples to keep one replica of the interesting part of the signal. Unfortunately,

as can be seen in figure A.5a, the kept signal has been impacted by the image-band of the whether negative or positive part RX spectrum (depending on the side of the IF spectrum kept). On the other hand, in the complex architecture, the I and Q outputs are combined to reconstruct the full complex IF spectrum, where positive and negative frequencies remain distinct. The in-band will fall in the positive frequencies, and the image-band in the negative frequencies. Then, theoretically, the real acquired signal can admit a noise level up to $+3dB$ higher than the complex one but in reality the difference is less important due to signal power loss because of splitting the received signal in the complex architecture.

- Software wise, with IQ data pulse compression, the processing will correspond to the one written previously with a N_s point complex Fourier transform. Using real data, it is necessary to perform a real-to-complex Fourier transform which consist of classic Fourier transform where half of the output is discarded since it corresponds to the complex conjugate of the other half. One important thing is that to perform an in-place DFT, which correspond to write the output of the DFT at the same memory location as the input one, it is necessary to perform a padding of the input so that there is sufficient memory for the complex output.
- The complex architecture is more expensive than a real one since it is more... complex. Obviously, there are more components: a quadrature mixer plus an ADC, a splitter but also the I and Q channel have to be recorded with a precise synchronisation.
- Often, as can be seen in figure A.5b, the recorded signal is shifted to record only the in-band part of the signal. By doing this, the quantity of data record by a complex and a real architecture for the same configuration (range resolution and ambiguous range) is the same. Notice that it is also possible on a complex architecture to record the full mixed signal for thermal noise level estimation and/or jamming detection.

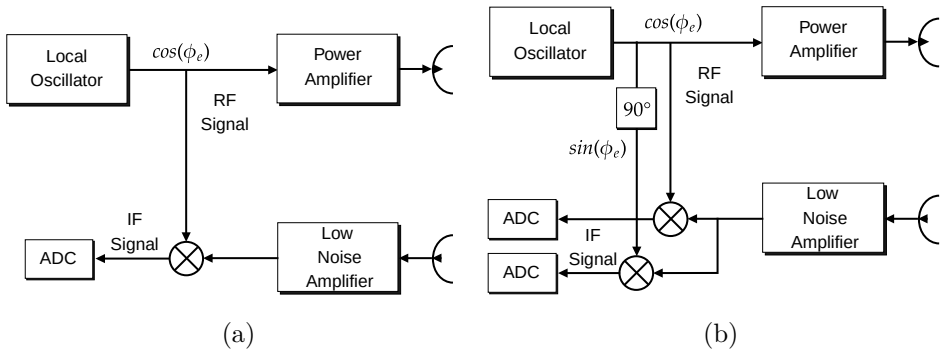

Figure A.4: Real and Complex Radar Acquisition Architecture

From this, we can state that when looking to buy or build a radar, its ability to perform real or complex data acquisition is important. The advertised sampling

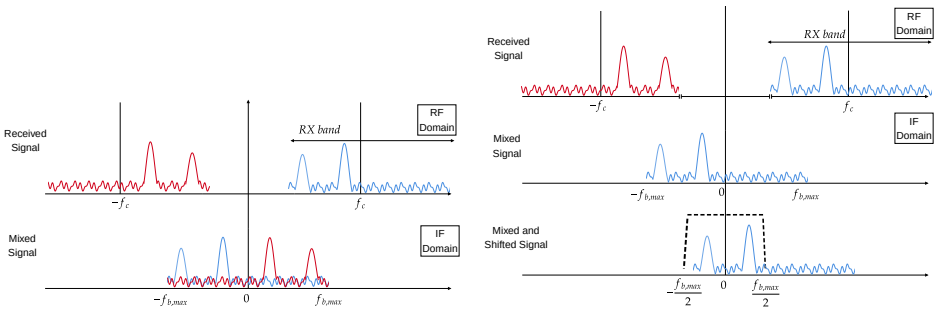

(a) (b)

Figure A.5: Signal spectrums associated to real and complex acquisition architecture

frequency must be put into context of acquisition type. Complex data acquisition may be easier and more straightforward to use especially when considering low-level programming, it also benefits theoretically from a slight gain in SNR.

Appendix B

Radar Platforms

This appendix presents the radar evaluation modules (EVMs) used during the experimental campaigns. They are illustrated in Figure B.1. Table B.1 summarizes the technical specifications of the radar platforms used in this thesis.

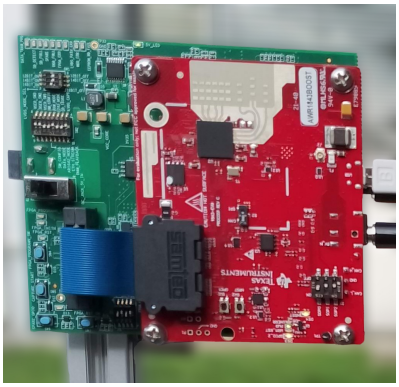

(a) AWR1843

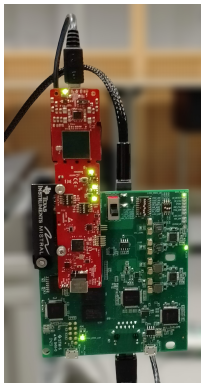

(b) AWR1843AOP

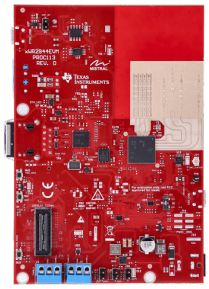

(c) AWR2944

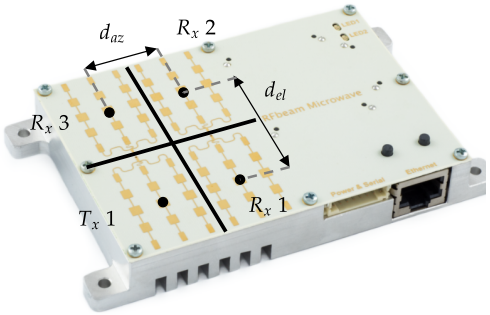

(d) RFBEAM KMD2

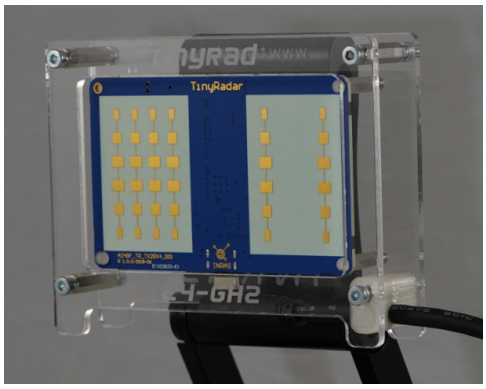

(e) Tinyrad

Figure B.1: Radar used during this thesis

Table B.1: Specifications of radar platforms used in this thesis

Parameter	K-MD2	Tinyrad	AWR1843	AWR1843AOP	AWR2944
Manufacturer	RFBEAM GmbH	Analog Devices	Texas Instruments	Texas Instruments	Texas Instruments
Frequency (GHz)	24	24	77	77	77
Max. RF Bandwidth (GHz)	1	0.25	4	4	5
Nb. TX	1	2	3	3	3
Nb. RX	3	4	4	4	4
Velocity Resolution (m/s)	0.05–0.3	0.2–0.5	0.05–0.1	0.05–0.1	0.03–0.08
Output Power (dBm)	+19	∼10	∼12	∼12	∼12
Data Output	Raw	Raw	Raw + PCL	Raw + PCL	Raw + PCL
Data Acquisition Type	Complex	Real	Real Complex	Real Complex	Real
Sampling Frequency Max. (MSPS)	1.91	10	25/12.5	25/12.5	40
Angle Measurement	Azimuth Elevation (2 az., 2 el.)	Azimuth (8 az.)	Azimuth + Elevation (8 az., 2 el.)	Azimuth + Elevation (4 az., 3 el.)	Azimuth + Elevation (12 az., 2 el.)

Appendix C

Open Source Code

A library has been done to perform localisation and mapping using coherent radar pre-processed pointcloud and raw data as inputs. It is written in C++ and supports ROS2. Its aim is to promote open-source development in the field of radar raw data-based navigation, and more specifically synthetic aperture radar for mobile robotics. The available functionalities are:

- Pointcloud based odometry from Doppler-Velocity Regression for translation and ICP for heading estimation.
- Raw data odometry from Range-Azimuth Maps feature based matching. Possibility to use only heading estimation from that functionality and to use pointcloud based odometry from Doppler-Velocity Regression for translation estimation.
- Synthetic Aperture Radar imagery for mapping. Visualisation of the imagery is possible whether via RQT or within RViz thanks to the GridMap library [Fankhauser 2016].
- Mono or Multi-dimensional DFT on the radar data cube are performed efficiently on the data cube thanks to FFTW library [Frigo 2005].

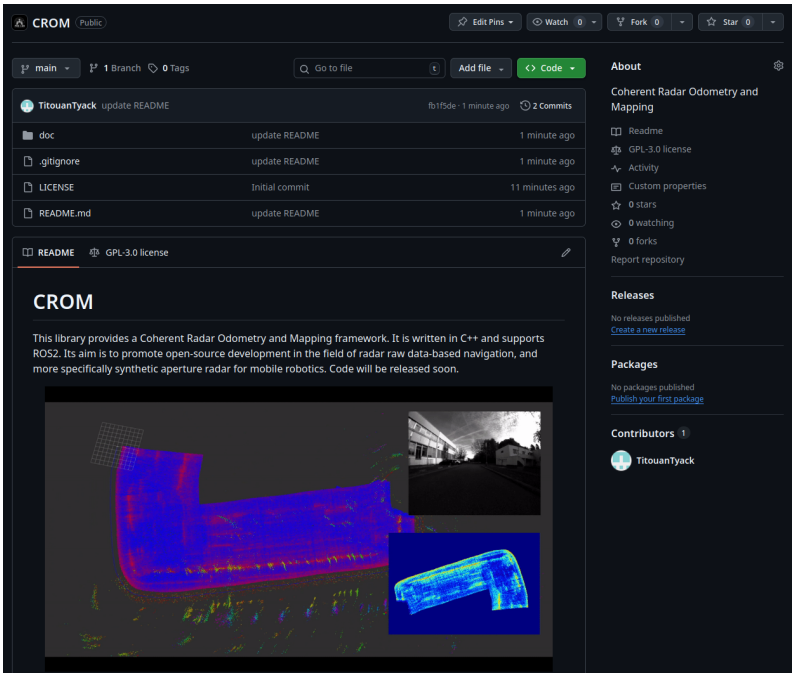

Figure C.1: Github repository of the library.

Bibliography

[Adams 2012] Adams, M., Jose, E. and Vo, B.-N. Robotic navigation and mapping with radar. Artech, 2012. (Cited in pages 6 and 26.)

[Adolfsson 2021] Adolfsson, D., Magnusson, M., Alhashimi, A., Lilienthal, A. J. and Andreasson, H. *CFEAR Radarodometry – Conservative Filtering for Efficient and Accurate Radar Odometry.* 2021. [Online]. Available: `https://arxiv.org/abs/2105.01457`. (Cited in page 45.)

[Adolfsson 2022] Adolfsson, D., Castellano-Quero, M., Magnusson, M., Lilienthal, A. J. and Andreasson, H. *CorAl: Introspection for Robust Radar and Lidar Perception in Diverse Environments Using Differential Entropy.* Robotics and Autonomous Systems, vol. 155, page 104136, September 2022. [Online]. Available: `http://arxiv.org/abs/2205.05975`. arXiv:2205.05975 [cs]. (Cited in page 45.)

[Adolfsson 2023a] Adolfsson, D., Karlsson, M., Kubelka, V., Magnusson, M. and Andreasson, H. *TBV Radar SLAM – trust but verify loop candidates.* April 2023. [Online]. Available: `http://arxiv.org/abs/2301.04397`. arXiv:2301.04397 [cs]. (Cited in page 26.)

[Adolfsson 2023b] Adolfsson, D., Magnusson, M., Alhashimi, A., Lilienthal, A. J. and Andreasson, H. *Lidar-level localization with radar? The CFEAR approach to accurate, fast and robust large-scale radar odometry in diverse environments.* IEEE Transactions on Robotics, vol. 39, no. 2, pages 1476–1495, April 2023. [Online]. Available: `http://arxiv.org/abs/2211.02445`. arXiv:2211.02445 [cs]. (Cited in page 26.)

[Albaba 2022a] Albaba, A., Pollin, S., Wambacq, P., Sahli, H. and Bourdoux, A. *Theoretical Angular Resolution of Forward-Looking MIMO-SAR Systems.* In 2022 19th European Radar Conference (EuRAD), pages 53–56, September 2022. (Cited in page 81.)

[Albaba 2022b] Albaba, A., Sakhnini, A., Sahli, H. and Bourdoux, A. *Forward-Looking MIMO-SAR for Enhanced Angular Resolution.* In 2022 IEEE Radar Conference (RadarConf22), pages 1–6, New York City, NY, USA, March 2022. IEEE. (Cited in page 81.)

[Alcantarilla 2012] Alcantarilla, P. F., Bartoli, A. and Davison, A. J. *KAZE Features.* In Fitzgibbon, A., Lazebnik, S., Perona, P., Sato, Y. and Schmid, C., editors, Computer Vision – ECCV 2012, pages 214–227, Berlin, Heidelberg, 2012. Springer. (Cited in page 45.)

[Alcantarilla 2013] Alcantarilla, P., Nuevo, J. and Bartoli, A. *Fast Explicit Diffusion for Accelerated Features in Nonlinear Scale Spaces.* In Procedings of the British Machine Vision Conference 2013, pages 13.1–13.11, Bristol, 2013. British Machine Vision Association. (Cited in page 45.)

[Almalioglu 2021] Almalioglu, Y., Turan, M., Lu, C. X., Trigoni, N. and Markham, A. *Milli-RIO: Ego-Motion Estimation With Low-Cost Millimetre-Wave Radar.* IEEE Sensors Journal, vol. 21, no. 3, pages 3314–3323, 2021. [Online]. Available: http://dx.doi.org/10.1109/JSEN.2020.3023243. (Cited in page 28.)

[Almutiry 2024] Almutiry, M. *Enhancing Automotive Safety with Low-Cost, High-Resolution MIMO Tomographic SAR: A Multi-Frequency Approach.* In 2024 Integrated Communications, Navigation and Surveillance Conference (ICNS), pages 1–6, April 2024. ISSN: 2155-4951. (Cited in page 81.)

[Balducci 2023] Balducci, G., Manzoni, M., Tebaldini, S., Monti-Guarnieri, A., Prati, C. M. and Russo, I. *An Improved Autofocus Algorithm With Bayesian Tracking of Residual Motion For Automotive MIMO-SAR Imaging.* In 2023 IEEE International Conference on Acoustics, Speech, and Signal Processing Workshops (ICASSPW), pages 1–5, June 2023. (Cited in pages 29, 61, and 101.)

[Barnes 2020] Barnes, D., Weston, R. and Posner, I. *Masking by Moving: Learning Distraction-Free Radar Odometry from Pose Information.* 2020. [Online]. Available: `https://arxiv.org/abs/1909.03752`. (Cited in page 45.)

[Bechter 2017] Bechter, J., Roos, F. and Waldschmidt, C. *Compensation of Motion-Induced Phase Errors in TDM MIMO Radars.* IEEE Microwave and Wireless Components Letters, vol. 27, no. 12, pages 1164–1166, 2017. [Online]. Available: http://dx.doi.org/10.1109/LMWC.2017.2751301. (Cited in page 104.)

[Blackman 2004] Blackman, S. *Multiple hypothesis tracking for multiple target tracking.* IEEE Aerospace and Electronic Systems Magazine, vol. 19, no. 1, pages 5–18, 2004. [Online]. Available: http://dx.doi.org/10.1109/MAES.2004.1263228. (Cited in page 91.)

[Brooker 2001] Brooker, G., Bishop, M. and Scheding, S. *Millimetre Waves for Robotics.* Australian Robotics and Automation Association, 2001. (Cited in pages v, 2, 9, and 26.)

[Brooker 2007] Brooker, G., Hennessey, R., Lobsey, C., Bishop, M. and Widzyk-Capehart, E. *Seeing through dust and water vapor: Millimeter wave radar sensors for mining applications.* Journal of field robotics., vol. 24, no. 7, pages 527–557, 2007. (Cited in pages 23 and 26.)

[Burnett 2021] Burnett, K., Yoon, D. J., Schoellig, A. P. and Barfoot, T. D. *Radar Odometry Combining Probabilistic Estimation and Unsupervised Feature Learning.* June 2021. [Online]. Available: `http://arxiv.org/abs/2105.14152`. arXiv:2105.14152 [cs]. (Cited in pages 26 and 45.)

[Bähnemann 2022] Bähnemann, R., Lawrance, N., Streichenberg, L., Chung, J. J., Pantic, M., Grathwohl, A., Waldschmidt, C. and Siegwart, R. *Under the Sand: Navigation and Localization of a Micro Aerial Vehicle for Landmine Detection with Ground Penetrating Synthetic Aperture Radar.* Field Robotics, vol. 2, no. 1, pages 1028–1067, March 2022. [Online]. Available: `http://arxiv.org/abs/2106.10108`. arXiv:2106.10108 [cs, eess]. (Cited in page 23.)

[Cadena 2016] Cadena, C., Carlone, L., Carrillo, H., Latif, Y., Scaramuzza, D., Neira, J., Reid, I. and Leonard, J. J. *Past, Present, and Future of Simultaneous Localization and Mapping: Toward the Robust-Perception Age.* IEEE Transactions on Robotics, vol. 32, no. 6, pages 1309–1332, December 2016. [Online]. Available: `https://ieeexplore.ieee.org/document/7747236`. (Cited in page 25.)

[Campos 2021] Campos, C., Elvira, R., Rodríguez, J. J. G., M. Montiel, J. M. and D. Tardós, J. *ORB-SLAM3: An Accurate Open-Source Library for Visual, Visual–Inertial, and Multimap SLAM.* IEEE Transactions on Robotics, vol. 37, no. 6, pages 1874–1890, 2021. [Online]. Available: http://dx.doi.org/10.1109/TRO.2021.3075644. (Cited in pages 2 and 50.)

[Cao 2020] Cao, C., Zhao, Y., Pang, X., Chen, S. and Hu, Y. *Novel DOAs estimation method based on Doppler aided Chinese remainder theorem with all phase DFT for multiple targets in sparse array.* IET Radar, Sonar & Navigation, vol. 14, no. 10, pages 1512–1520, 2020. [Online]. Available: `https://ietresearch.onlinelibrary.wiley.com/doi/abs/10.1049/iet-rsn.2019.0464`. (Cited in page 89.)

[Capon 1969] Capon, J. *High-resolution frequency-wavenumber spectrum analysis.* Proceedings of the IEEE, vol. 57, no. 8, pages 1408–1418, August 1969. [Online]. Available: `https://ieeexplore.ieee.org/document/1449208`. (Cited in page 44.)

[Chatzitheodoridi 2023] Chatzitheodoridi, M.-E. *Processing Optimization for Continuous Phase Modulation-based Joint Radar-Communication System : Application on Imaging Radar.* PhD thesis, 2023. Thèse de doctorat dirigée par Oriot, HélèneTaylor, Abigael et Rabaste, Olivier Sciences du traitement du signal et des images université Paris-Saclay 2023. (Cited in page 72.)

[Checchin 2010] Checchin, P., Gérossier, F., Blanc, C., Chapuis, R. and Trassoudaine, L. *Radar Scan Matching SLAM Using the Fourier-Mellin*

Transform. In Siciliano, B., Khatib, O., Groen, F., Howard, A., Iagnemma, K. and Kelly, A., editors, Field and Service Robotics, volume 62, pages 151–161. Springer Berlin Heidelberg, Berlin, Heidelberg, 2010. Series Title: Springer Tracts in Advanced Robotics. (Cited in page 26.)

[Chen 2023] Chen, H., Liu, Y. and Cheng, Y. *DRIO: Robust Radar-Inertial Odometry in Dynamic Environments*. IEEE Robotics and Automation Letters, vol. 8, no. 9, pages 5918–5925, 2023. [Online]. Available: `https://ieeexplore.ieee.org/abstract/document/10207713`. Conference Name: IEEE Robotics and Automation Letters. (Cited in page 27.)

[Chen 2024a] Chen, S., Li, X., Li, S., Zhou, Y. and Wang, S. *RIs-Calib: An Open-Source Spatiotemporal Calibrator for Multiple 3D Radars and IMUs Based on Continuous-Time Estimation*, 2024. (Cited in page 34.)

[Chen 2024b] Chen, S., Li, X., Li, S., Zhou, Y. and Wang, S. *RIs-Calib: An Open-Source Spatiotemporal Calibrator for Multiple 3D Radars and IMUs Based on Continuous-Time Estimation*, 2024. (Cited in page 49.)

[Chen 2024c] Chen, S., Li, X., Li, S., Zhou, Y. and Wang, S. *River: A Tightly-Coupled Radar-Inertial Velocity Estimator Based on Continuous-Time Optimization*. IEEE Robotics and Automation Letters, vol. 9, no. 7, pages 6107–6114, July 2024. [Online]. Available: `https://ieeexplore.ieee.org/document/10529532/?arnumber=10529532`. Conference Name: IEEE Robotics and Automation Letters. (Cited in page 27.)

[Chen 2024d] Chen, S., Li, X., Li, S., Zhou, Y. and Yang, X. *iKalibr: Unified Targetless Spatiotemporal Calibration for Resilient Integrated Inertial Systems*, 2024. (Cited in pages 34 and 49.)

[Cheng 2023a] Cheng, Q., Wise, E. and Kelly, J. *Extrinsic Calibration of 2D Millimetre-Wavelength Radar Pairs Using Ego-Velocity Estimates*. In 2023 IEEE/ASME International Conference on Advanced Intelligent Mechatronics (AIM), pages 559–565, 2023. (Cited in page 34.)

[Cheng 2023b] Cheng, Y., Pang, C., Jiang, M. and Liu, Y. *Relocalization based on millimeter wave radar point cloud for visually degraded environments*. Journal of Field Robotics, vol. 40, no. 4, pages 901–918, 2023. [Online]. Available: `https://onlinelibrary.wiley.com/doi/abs/10.1002/rob.22162`. (Cited in page 82.)

[Cho 2006] Cho, B.-L., Kong, Y.-K., Park, H.-G. and Kim, Y.-S. *Automobile-based SAR/InSAR system for ground experiments*. IEEE Geoscience and Remote Sensing Letters, vol. 3, no. 3, pages 401–405, July 2006. [Online]. Available: `https://ieeexplore.ieee.org/document/1658014`. (Cited in page 60.)

[Corominas-Murtra 2016] Corominas-Murtra, A., Vallvé, J., Solà, J., Flores, I. and Andrade-Cetto, J. *Observability analysis and optimal sensor placement in*

stereo radar odometry. In 2016 IEEE International Conference on Robotics and Automation (ICRA), pages 3161–3166, 2016. (Cited in pages 26, 31, and 36.)

[Debeunne 2024] Debeunne, C., Torres, A. and Vivet, D. *SaDVIO: Sparsify and Densify VIO for UGV Traversability Estimation*. IEEE Robotics and Automation Letters, vol. 9, no. 10, pages 8842–8849, October 2024. [Online]. Available: `https://ieeexplore.ieee.org/document/10616232`. (Cited in pages 2 and 47.)

[Dell 1963] Dell, H. A. *Introduction to Radar Systems. Merrill I. Skolnik. McGraw-Hill Book Co., London and New York. 1962.* The Journal of the Royal Aeronautical Society, vol. 67, pages 313 – 313, 1963. (Cited in page 40.)

[Demchev 2017] Demchev, D., Volkov, V., Kazakov, E., Alcantarilla, P. F., Sandven, S. and Khmeleva, V. *Sea Ice Drift Tracking From Sequential SAR Images Using Accelerated-KAZE Features*. IEEE Transactions on Geoscience and Remote Sensing, vol. 55, no. 9, pages 5174–5184, September 2017. [Online]. Available: `https://ieeexplore.ieee.org/document/7938663/`. (Cited in page 45.)

[Diao 2024] Diao, P. S., Alves, T., Poussot, B. and Azarian, S. *A Review of Radar Detection Fundamentals*. IEEE Aerospace and Electronic Systems Magazine, vol. 39, no. 9, pages 4–24, 2024. [Online]. Available: http://dx.doi.org/10.1109/MAES.2022.3177395. (Cited in page 20.)

[Dissanayake 2001] Dissanayake, M., Newman, P., Clark, S., Durrant-Whyte, H. and Csorba, M. *A solution to the simultaneous localization and map building (SLAM) problem*. IEEE Transactions on Robotics and Automation, vol. 17, no. 3, pages 229–241, 2001. [Online]. Available: http://dx.doi.org/10.1109/70.938381. (Cited in pages 2 and 26.)

[Do 2024] Do, H. V., Kim, Y. H., Lee, J. H., Lee, M. H. and Song, J. W. *DeRO: Dead Reckoning Based on Radar Odometry With Accelerometers Aided for Robot Localization*. November 2024. [Online]. Available: `http://arxiv.org/abs/2403.05136`. arXiv:2403.05136 [cs]. (Cited in page 27.)

[Doer 2020a] Doer, C. and Trommer, G. F. *An EKF Based Approach to Radar Inertial Odometry*. In 2020 IEEE International Conference on Multisensor Fusion and Integration for Intelligent Systems (MFI), 2020. (Cited in page 26.)

[Doer 2020b] Doer, C. and Trommer, G. F. *Radar Inertial Odometry With Online Calibration*. In 2020 European Navigation Conference (ENC), pages 1–10, 2020. (Cited in pages 26 and 34.)

[Dosovitskiy 2017] Dosovitskiy, A., Ros, G., Codevilla, F., Lopez, A. and Koltun, V. *CARLA: An Open Urban Driving Simulator.* 2017. [Online]. Available: `https://arxiv.org/abs/1711.03938`. (Cited in page 100.)

[Dubé 2019] Dubé, R., Cramariuc, A., Dugas, D., Sommer, H., Dymczyk, M., Nieto, J., Siegwart, R. and Cadena, C. *SegMap: Segment-based mapping and localization using data-driven descriptors.* The International Journal of Robotics Research, vol. 39, no. 2–3, page 339–355, July 2019. [Online]. Available: `http://dx.doi.org/10.1177/0278364919863090`. (Cited in page 50.)

[Duersch 2004] Duersch, M. *BYU micro-SAR: A very small, low-power LFM-CW Synthetic Aperture Radar.* Theses and Dissertations, December 2004. [Online]. Available: `https://scholarsarchive.byu.edu/etd/728`. (Cited in page 60.)

[Eichel 1989] Eichel, P. H. and Jakowatz, C. V. *Phase-gradient algorithm as an optimal estimator of the phase derivative.* Optics letters, vol. 14 20, pages 1101–3, 1989. [Online]. Available: `https://api.semanticscholar.org/CorpusID:1584589`. (Cited in page 63.)

[Fankhauser 2016] Fankhauser, P. and Hutter, M. *A Universal Grid Map Library: Implementation and Use Case for Rough Terrain Navigation.* In Koubaa, A., editor, Robot Operating System (ROS) – The Complete Reference (Volume 1), chapter 5. Springer, 2016. (Cited in page 111.)

[Farhadi 2019] Farhadi, M., Feger, R., Fink, J., Gonser, M., Hasch, J. and Stelzer, A. *Adaption of Fast Factorized Back-Projection to Automotive SAR Applications.* In 2019 16th European Radar Conference (EuRAD), pages 261–264, October 2019. (Cited in page 81.)

[Feger 2017] Feger, R., Haderer, A. and Stelzer, A. *Experimental verification of a 77-GHz synthetic aperture radar system for automotive applications.* In 2017 IEEE MTT-S International Conference on Microwaves for Intelligent Mobility (ICMIM), pages 111–114, March 2017. (Cited in page 61.)

[Feriol 2020] Feriol, F., Vivet, D. and Watanabe, Y. *A Review of Environmental Context Detection for Navigation Based on Multiple Sensors.* Sensors, 2020. [Online]. Available: http://dx.doi.org/10.3390/s20164532. (Cited in page 2.)

[Ferrari 1997] Ferrari, A., Berenguer, C. and Alengrin, G. *Doppler ambiguity resolution using multiple PRF.* IEEE Transactions on Aerospace and Electronic Systems, vol. 33, no. 3, pages 738–751, 1997. [Online]. Available: http://dx.doi.org/10.1109/7.599236. (Cited in page 89.)

[FERRO-FAMIL 2013] FERRO-FAMIL, L. *Principes de l'imagerie Radar à synthèse d'ouverture (RSO).* Techniques de l'ingénieur Le traitement du signal

et ses applications, vol. base documentaire : TIP383WEB., no. ref. article : te6702, 2013. [Online]. Available: https://www.techniques-ingenieur.fr/base-documentaire/technologies-de-l-information-th9/radiolocalisation-42297210/principes-de-l-imagerie-radar-a-synthese-d-ouverture-rso-te6702/. fre. (Cited in pages 58 and 76.)

[Fortmann 1983] Fortmann, T., Bar-Shalom, Y. and Scheffe, M. *Sonar tracking of multiple targets using joint probabilistic data association.* IEEE Journal of Oceanic Engineering, vol. 8, no. 3, pages 173–184, 1983. [Online]. Available: http://dx.doi.org/10.1109/JOE.1983.1145560. (Cited in page 91.)

[Franceschetti 2014] Franceschetti, G., Iodice, A. and Riccio, D. *Forward-Looking Synthetic Aperture Radar (FLoSAR): The Array Approach.* IEEE Geoscience and Remote Sensing Letters, vol. 11, no. 1, pages 303–307, January 2014. [Online]. Available: https://ieeexplore.ieee.org/document/6547984/. (Cited in page 81.)

[Frey 2013] Frey, O., Werner, C. L., Wegmuller, U., Wiesmann, A., Henke, D. and Magnard, C. *A car-borne SAR and InSAR experiment.* In 2013 IEEE International Geoscience and Remote Sensing Symposium - IGARSS, pages 93–96, Melbourne, Australia, July 2013. IEEE. (Cited in page 81.)

[Frigo 2005] Frigo, M. and Johnson, S. G. *The Design and Implementation of FFTW3.* Proceedings of the IEEE, vol. 93, no. 2, pages 216–231, 2005. Special issue on "Program Generation, Optimization, and Platform Adaptation". (Cited in page 111.)

[Frosi 2024] Frosi, M., Usuelli, M. and Matteucci, M. *Advancements in Radar Odometry.* April 2024. [Online]. Available: http://arxiv.org/abs/2310.12729. arXiv:2310.12729 [cs]. (Cited in page 26.)

[Galeote-Luque 2023] Galeote-Luque, A., Kubelka, V., Magnusson, M., Ruiz-Sarmiento, J.-R. and Gonzalez-Jimenez, J. *Doppler-only Single-scan 3D Vehicle Odometry*, 2023. (Cited in page 27.)

[Gálvez-López 2012] Gálvez-López, D. and Tardós, J. D. *Bags of Binary Words for Fast Place Recognition in Image Sequences.* IEEE Transactions on Robotics, vol. 28, no. 5, pages 1188–1197, October 2012. [Online]. Available: http://dx.doi.org/10.1109/TRO.2012.2197158. (Cited in page 50.)

[Gao 2021] Gao, X., Roy, S. and Xing, G. *MIMO-SAR: A Hierarchical High-Resolution Imaging Algorithm for mmWave FMCW Radar in Autonomous Driving.* IEEE Transactions on Vehicular Technology, vol. 70, no. 8, pages 7322–7334, August 2021. [Online]. Available: http://dx.doi.org/10.1109/TVT.2021.3092355. Conference Name: IEEE Transactions on Vehicular Technology. (Cited in pages 28 and 62.)

[Geneva 2020] Geneva, P., Eckenhoff, K., Lee, W., Yang, Y. and Huang, G. *Open-VINS: A Research Platform for Visual-Inertial Estimation.* In 2020 IEEE International Conference on Robotics and Automation (ICRA), pages 4666–4672, May 2020. ISSN: 2577-087X. (Cited in pages 2 and 50.)

[Gentil 2025] Gentil, C. L., Brizi, L., Lisus, D., Qiao, X., Grisetti, G. and Barfoot, T. D. *DRO: Doppler-Aware Direct Radar Odometry.* April 2025. [Online]. Available: `http://arxiv.org/abs/2504.20339`. arXiv:2504.20339 [cs]. (Cited in page 26.)

[Gerossier 2009] Gerossier, F., Checchin, P., Blanc, C., Chapuis, R. and Trassoudaine, L. *Trajectory-oriented EKF-SLAM using the Fourier-Mellin Transform applied to Microwave Radar Images.* In 2009 IEEE/RSJ International Conference on Intelligent Robots and Systems, pages 4925–4930, St. Louis, MO, October 2009. IEEE. (Cited in page 26.)

[Giovagnola 2023] Giovagnola, J., Moro Megías, J. B., Fernández, M. M., Cuéllar, M. P. and Morales Santos, D. P. *AirLoop: A Simulation Framework for Testing of UAV Services.* IEEE Access, vol. 11, pages 23309–23325, 2023. [Online]. Available: http://dx.doi.org/10.1109/ACCESS.2023.3253788. (Cited in page 100.)

[Girod 2024] Girod, R., Hauswirth, M., Pfreundschuh, P., Biasio, M. and Siegwart, R. *A robust baro-radar-inertial odometry m-estimator for multicopter navigation in cities and forests.* August 2024. [Online]. Available: `http://arxiv.org/abs/2408.05764`. arXiv:2408.05764 [cs]. (Cited in page 27.)

[Gisder 2018] Gisder, T., Harrer, F. and Biebl, E. *Application Of A Stream-Based SAR-Backprojection Approach For Automotive Environment Perception.* In 2018 19th International Radar Symposium (IRS), pages 1–10, June 2018. ISSN: 2155-5753. (Cited in page 61.)

[Gishkori 2019] Gishkori, S., Daniel, L., Gashinova, M. and Mulgrew, B. *Imaging for a Forward Scanning Automotive Synthetic Aperture Radar.* IEEE Transactions on Aerospace and Electronic Systems, vol. 55, no. 3, pages 1420–1434, June 2019. [Online]. Available: `https://ieeexplore.ieee.org/document/8469095`. (Cited in page 81.)

[Goldberg 2002] Goldberg, S., Maimone, M. and Matthies, L. *Stereo vision and rover navigation software for planetary exploration.* In Proceedings, IEEE Aerospace Conference, volume 5, pages 5–2025–5–2036, Big Sky, MT, USA, 2002. IEEE. (Cited in page 81.)

[Gonzalez 2019] Gonzalez, H. A., Liu, C., Vogginger, B. and Mayr, C. G. *Doppler Ambiguity Resolution for Binary-Phase-Modulated MIMO FMCW Radars.*

In 2019 International Radar Conference (RADAR), pages 1–6, 2019. (Cited in page 89.)

[Goodman 2011] Goodman, J. L. *History of Space Shuttle Rendezvous*. October 2011. [Online]. Available: `https://ntrs.nasa.gov/citations/20110023479`. NTRS Author Affiliations: United Space Alliance NTRS Report/Patent Number: JSC-CN-24483 NTRS Document ID: 20110023479 NTRS Research Center: Johnson Space Center (JSC). (Cited in page 6.)

[Grebner 2022a] Grebner, T., Linder, M., Kern, N., Schoeder, P. and Waldschmidt, C. *6D Self-Calibration of the Position and Orientation of Radar Sensors in a Radar Network*. In 2022 19th European Radar Conference (EuRAD), pages 157–160, September 2022. (Cited in page 34.)

[Grebner 2022b] Grebner, T., Schoeder, P., Janoudi, V. and Waldschmidt, C. *Radar-Based Mapping of the Environment: Occupancy Grid-Map Versus SAR*. IEEE Microwave and Wireless Components Letters, vol. 32, no. 3, pages 253–256, March 2022. [Online]. Available: `https://ieeexplore.ieee.org/document/9703257`. (Cited in pages 61 and 101.)

[Grebner 2024] Grebner, T., Riekenbrauck, R. and Waldschmidt, C. *Simultaneous Localization and Mapping (SLAM) for Synthetic Aperture Radar (SAR) Processing in the Field of Autonomous Driving*. IEEE Transactions on Radar Systems, vol. 2, pages 47–66, 2024. [Online]. Available: http://dx.doi.org/10.1109/TRS.2023.3347734. (Cited in pages 28 and 45.)

[Guo 2024] Guo, R., Gao, Y., Ren, Z., Zhang, Z., Xie, J. and Yang, B. *Urban SAR Tomography With Z-Structure Constraint of Buildings*. IEEE Journal of Selected Topics in Applied Earth Observations and Remote Sensing, vol. 17, pages 9945–9960, 2024. [Online]. Available: `https://ieeexplore.ieee.org/document/10528800/`. (Cited in page 81.)

[Harrer 2017] Harrer, F., Pfeiffer, F., Löffler, A., Gisder, T. and Biebl, E. *Synthetic aperture radar algorithm for a global amplitude map*. In 2017 14th Workshop on Positioning, Navigation and Communications (WPNC), pages 1–6, October 2017. (Cited in page 61.)

[Herraez 2024] Herraez, D. C., Zeller, M., Chang, L., Vizzo, I., Heidingsfeld, M. and Stachniss, C. *Radar-Only Odometry and Mapping for Autonomous Vehicles*. In 2024 IEEE International Conference on Robotics and Automation (ICRA), pages 10275–10282, May 2024. (Cited in pages 28, 49, and 101.)

[Herraez 2025] Herraez, D. C., Kaschner, F., Zeller, M., Muhle, D., Behley, J., Heidingsfeld, M., Cremers, D. and Stachniss, C. *Ground-Aware Automotive Radar Odometry*. 2025 IEEE International Conference on Robotics and Automation (ICRA), 2025. (Cited in pages 28, 49, and 101.)

[Hexsel 2022] Hexsel, B., Vhavle, H. and Chen, Y. *DICP: Doppler Iterative Closest Point Algorithm*. May 2022. [Online]. Available: `http://arxiv.org/abs/2201.11944`. arXiv:2201.11944 [cs]. (Cited in page 28.)

[Hoffmann 2023] Hoffmann, M., Noegel, T., Schüßler, C., Schwenger, L., Gulden, P., Fey, D. and Vossiek, M. *Implementation of Real-Time Automotive SAR Imaging*. In 2023 20th European Radar Conference (EuRAD), pages 327–330, September 2023. (Cited in page 62.)

[Holder 2019] Holder, M., Hellwig, S. and Winner, H. *Real-Time Pose Graph SLAM based on Radar*. In 2019 IEEE Intelligent Vehicles Symposium (IV), pages 1145–1151, June 2019. ISSN: 2642-7214. (Cited in pages 28 and 45.)

[Hong 2020] Hong, Z., Petillot, Y. and Wang, S. *RadarSLAM: Radar based Large-Scale SLAM in All Weathers*. In 2020 IEEE/RSJ International Conference on Intelligent Robots and Systems (IROS), pages 5164–5170, October 2020. ISSN: 2153-0866. (Cited in pages 26 and 45.)

[Hoppe 1992] Hoppe, H., DeRose, T., Duchamp, T., McDonald, J. and Stuetzle, W. *Surface reconstruction from unorganized points*. SIGGRAPH Comput. Graph., vol. 26, no. 2, pages 71–78, 1992. [Online]. Available: `https://dl.acm.org/doi/10.1145/142920.134011`. (Cited in page 80.)

[Huang 2021] Huang, Y., Zhang, Q. and Ferro-Famil, L. *Forest Height Estimation Using a Single-Pass Airborne L-Band Polarimetric and Interferometric SAR System and Tomographic Techniques*. Remote Sensing, vol. 13, no. 3, 2021. [Online]. Available: `https://www.mdpi.com/2072-4292/13/3/487`. (Cited in page 80.)

[Huang 2024] Huang, J.-T., Xu, R., Hinduja, A. and Kaess, M. *Multi-Radar Inertial Odometry for 3D State Estimation using mmWave Imaging Radar*, 2024. (Cited in page 27.)

[Iovescu 2017] Iovescu, C. *The fundamentals of millimeter wave sensors*. In The fundamentals of millimeter wave sensors, 2017. (Cited in pages v and 12.)

[Iqbal 2021] Iqbal, H., Löffler, A., Mejdoub, M. N., Zimmermann, D. and Gruson, F. *Imaging radar for automated driving functions*. International Journal of Microwave and Wireless Technologies, vol. 13, no. 7, pages 682–690, September 2021. [Online]. Available: `https://www.cambridge.org/core/journals/international-journal-of-microwave-and-wireless-technologies/article/imaging-radar-for-automated-driving-functions/81B92D1CCF86309E8A354783A343861E`. Publisher: Cambridge University Press. (Cited in page 28.)

[Jiang 2022] Jiang, P., Osteen, P., Wigness, M. and Saripalli, S. *RELLIS-3D Dataset: Data, Benchmarks and Analysis*. May 2022. [Online]. Available:

http://arxiv.org/abs/2011.12954. arXiv:2011.12954 [cs]. (Cited in page 81.)

[Kabsch 1976] Kabsch, W. *A solution for the best rotation to relate two sets of vectors.* Acta Crystallographica Section A, vol. 32, no. 5, pages 922–923, Sep 1976. [Online]. Available: https://doi.org/10.1107/S0567739476001873. (Cited in pages 29 and 46.)

[Kabuli 2025] Kabuli, L. A. and Foster, G. *Automotive Elevation Mapping with Interferometric Synthetic Aperture Radar.* January 2025. [Online]. Available: http://arxiv.org/abs/2501.08495. arXiv:2501.08495 [eess]. (Cited in pages 81 and 101.)

[Kellner 2013] Kellner, D., Barjenbruch, M., Klappstein, J., Dickmann, J. and Dietmayer, K. *Instantaneous ego-motion estimation using Doppler radar.* In 16th International IEEE Conference on Intelligent Transportation Systems (ITSC 2013), pages 869–874, 2013. (Cited in page 26.)

[Kellner 2014] Kellner, D., Barjenbruch, M., Klappstein, J., Dickmann, J. and Dietmayer, K. *Instantaneous ego-motion estimation using multiple Doppler radars.* In 2014 IEEE International Conference on Robotics and Automation (ICRA), pages 1592–1597, 2014. (Cited in page 26.)

[Kim 2018] Kim, G. and Kim, A. *Scan Context: Egocentric Spatial Descriptor for Place Recognition Within 3D Point Cloud Map.* In 2018 IEEE/RSJ International Conference on Intelligent Robots and Systems (IROS), pages 4802–4809, October 2018. ISSN: 2153-0866. (Cited in pages 28 and 50.)

[Kim 2024a] Kim, H., Jang, H. and Kim, A. *2D Ego-Motion with Yaw Estimation using Only mmWave Radars via Two-Way weighted ICP*, 2024. (Cited in page 27.)

[Kim 2024b] Kim, S., Seok, J., Lee, J. and Jo, K. *Radar4Motion: IMU-Free 4D Radar Odometry with Robust Dynamic Filtering and RCS-Weighted Matching.* IEEE Transactions on Intelligent Vehicles, pages 1–11, 2024. [Online]. Available: https://ieeexplore.ieee.org/document/10715681. Conference Name: IEEE Transactions on Intelligent Vehicles. (Cited in pages 28, 49, and 101.)

[Koenig 2004] Koenig, N. and Howard, A. *Design and Use Paradigms for Gazebo, An Open-Source Multi-Robot Simulator.* In IEEE/RSJ International Conference on Intelligent Robots and Systems, pages 2149–2154, Sendai, Japan, Sep 2004. (Cited in page 100.)

[Krim 1996] Krim, H. and Viberg, M. *Two decades of array signal processing research: the parametric approach.* IEEE Signal Process. Mag., vol. 13, pages 67–94, 1996. [Online]. Available: https://api.semanticscholar.org/CorpusID:86714323. (Cited in page 43.)

[Kronauge 2010] Kronauge, M., Schroeder, C. and Rohling, H. *Radar target detection and Doppler ambiguity resolution.* In 11-th INTERNATIONAL RADAR SYMPOSIUM, pages 1–4, 2010. (Cited in page 89.)

[Kubelka 2023] Kubelka, V., Fritz, E. and Magnusson, M. *Do we need scan-matching in radar odometry?*, 2023. (Cited in pages 27, 49, and 101.)

[Lee 2020] Lee, C.-L., Hsueh, Y.-H., Wang, C.-C. and Lin, W.-C. *Extrinsic and Temporal Calibration of Automotive Radar and 3D LiDAR.* In 2020 IEEE/RSJ International Conference on Intelligent Robots and Systems (IROS), pages 9976–9983, October 2020. (Cited in page 49.)

[Li 2013] Li, K., Habtemariam, B., Tharmarasa, R., Pelletier, M. and Kirubarjan, T. *Multitarget Tracking with Doppler Ambiguity.* IEEE Transactions on Aerospace and Electronic Systems, vol. 49, no. 4, pages 2640–2656, 2013. [Online]. Available: http://dx.doi.org/10.1109/TAES.2013.6621842. (Cited in page 89.)

[Li 2015] Li, Y., Wang, S., Tian, Q. and Ding, X. *A survey of recent advances in visual feature detection.* Neurocomputing, vol. 149, pages 736–751, February 2015. [Online]. Available: `https://www.sciencedirect.com/science/article/pii/S0925231214010121`. (Cited in page 45.)

[Li 2021] Li, X., Wang, X., Yang, Q. and Fu, S. *Signal Processing for TDM MIMO FMCW Millimeter-Wave Radar Sensors.* IEEE Access, vol. 9, pages 167959–167971, 2021. [Online]. Available: http://dx.doi.org/10.1109/ACCESS.2021.3137387. (Cited in page 11.)

[Li 2022] Li, L., Ding, Z., Wang, Y., Gao, W., Liu, M., Zhang, T., Tian, W. and Zeng, T. *Linear-Array-MIMO SAR Tomography: An Autofocus Approach for Time-Variant and 3-D Space-Variant Motion Errors.* IEEE Transactions on Geoscience and Remote Sensing, vol. 60, pages 1–17, 2022. [Online]. Available: `https://ieeexplore.ieee.org/document/9512016/`. (Cited in page 81.)

[Li 2023] Li, X., Zhang, H. and Chen, W. *4D Radar-Based Pose Graph SLAM With Ego-Velocity Pre-Integration Factor.* IEEE Robotics and Automation Letters, vol. 8, no. 8, pages 5124–5131, August 2023. [Online]. Available: `https://ieeexplore.ieee.org/document/10173499/?arnumber=10173499`. Conference Name: IEEE Robotics and Automation Letters. (Cited in page 28.)

[Liu 2019] Liu, P., Dai, X., Li, D. and Sun, M. *Overview of Semantic Information Applications for Robots.* In 2019 11th International Conference on Measuring Technology and Mechatronics Automation (ICMTMA), pages 370–374, 2019. (Cited in page 8.)

[Lubanco 2024] Lubanco, D. L. S., Hashem, A., Pichler-Scheder, M., Schlechter, T., Feger, R. and Stelzer, A. *MS-SLAM: Multiple Input Multiple Output Synthetic Aperture Radar Simultaneous Localization and Mapping.* IEEE Transactions on Intelligent Vehicles, pages 1–20, 2024. [Online]. Available: `https://ieeexplore.ieee.org/document/10803095/?arnumber=10803095`. Conference Name: IEEE Transactions on Intelligent Vehicles. (Cited in pages 29, 62, and 101.)

[Lucas 1981] Lucas, B. D. and Kanade, T. *An Iterative Image Registration Technique with an Application to Stereo Vision.* 1981. (Cited in page 47.)

[Ma 2023] Ma, Y., Zhao, X., Li, H., Gu, Y., Lang, X. and Liu, Y. *RoLM: Radar on LiDAR Map Localization.* In 2023 IEEE International Conference on Robotics and Automation (ICRA), pages 3976–3982, May 2023. (Cited in page 82.)

[Ma 2024] Ma, Y., Li, H., Zhao, X., Gu, Y., Lang, X., Li, L. and Liu, Y. *FMCW Radar on LiDAR map localization in structural urban environments.* Journal of Field Robotics, vol. 41, no. 3, pages 699–717, 2024. [Online]. Available: `https://onlinelibrary.wiley.com/doi/abs/10.1002/rob.22291`. (Cited in pages 82 and 101.)

[Manzoni 2023a] Manzoni, M., Tagliaferri, D., Rizzi, M., Tebaldini, S., Guarnieri, A. V. M., Prati, C. M., Nicoli, M., Russo, I., Duque, S., Mazzucco, C. and Spagnolini, U. *Motion Estimation and Compensation in Automotive MIMO SAR.* IEEE Transactions on Intelligent Transportation Systems, vol. 24, no. 2, pages 1756–1772, February 2023. [Online]. Available: http://dx.doi.org/10.1109/TITS.2022.3219542. Conference Name: IEEE Transactions on Intelligent Transportation Systems. (Cited in pages 29 and 61.)

[Manzoni 2023b] Manzoni, M., Tebaldini, S., Monti-Guarnieri, A. V. and Prati, C. M. *Analysis of multipath effects in automotive MIMO-SAR.* In 2023 IEEE Radar Conference (RadarConf23), pages 1–6, May 2023. (Cited in page 62.)

[Manzoni 2023c] Manzoni, M., Tebaldini, S., Monti-Guarnieri, A. V. and Prati, C. M. *Multipath in Automotive MIMO SAR Imaging.* IEEE Transactions on Geoscience and Remote Sensing, vol. 61, pages 1–12, 2023. [Online]. Available: http://dx.doi.org/10.1109/TGRS.2023.3240705. Conference Name: IEEE Transactions on Geoscience and Remote Sensing. (Cited in page 62.)

[Michalczyk 2022] Michalczyk, J., Jung, R. and Weiss, S. *Tightly-Coupled EKF-Based Radar-Inertial Odometry.* In 2022 IEEE/RSJ International Conference on Intelligent Robots and Systems (IROS), pages 12336–12343, 2022. (Cited in page 27.)

[Moravec 1985] Moravec, H. and Elfes, A. *High resolution maps from wide angle sonar.* In Proceedings. 1985 IEEE International Conference on Robotics and Automation, volume 2, pages 116–121, 1985. (Cited in page 53.)

[Moreira 2013] Moreira, A., Prats-Iraola, P., Younis, M., Krieger, G., Hajnsek, I. and Papathanassiou, K. P. *A tutorial on synthetic aperture radar.* IEEE Geoscience and Remote Sensing Magazine, vol. 1, no. 1, pages 6–43, 2013. [Online]. Available: http://dx.doi.org/10.1109/MGRS.2013.2248301. (Cited in page 60.)

[Mukaide 2021] Mukaide, Y. and Yamada, H. *Experimental Study on Resolution Enhancement in Height for Automotive MW-3D-SAR.* In 2020 International Symposium on Antennas and Propagation (ISAP), pages 609–610, January 2021. (Cited in page 81.)

[Ng 2021] Ng, Y. Z., Choi, B., Tan, R. and Heng, L. *Continuous-time Radar-inertial Odometry for Automotive Radars.* In 2021 IEEE/RSJ International Conference on Intelligent Robots and Systems (IROS), pages 323–330, September 2021. ISSN: 2153-0866. (Cited in page 26.)

[Noegel 2024] Noegel, T., Reinecke, M., Schwenger, L., Heidbrink, M., Hoffmann, M. and Vossiek, M. *Implementation of 3D Automotive SAR Imaging.* In 2024 21st European Radar Conference (EuRAD), pages 352–355, September 2024. (Cited in page 81.)

[Noferini 2006] Noferini, L., Pieraccini, M., Luzi, G., Mecatti, D., Macaluso, G. and Atzeni, C. *Ground-based Radar Interferometry for Terrain Mapping.* In 2006 IEEE International Symposium on Geoscience and Remote Sensing, pages 2569–2572, July 2006. ISSN: 2153-7003. (Cited in page 81.)

[Park 2021] Park, Y. S., Shin, Y.-S., Kim, J. and Kim, A. *3D ego-Motion Estimation Using low-Cost mmWave Radars via Radar Velocity Factor for Pose-Graph SLAM.* IEEE Robotics and Automation Letters, vol. 6, no. 4, pages 7691–7698, October 2021. [Online]. Available: `https://ieeexplore.ieee.org/document/9495184/?arnumber=9495184`. Conference Name: IEEE Robotics and Automation Letters. (Cited in page 27.)

[Petracek 2024] Petracek, P., Kratky, V., Baca, T., Petrlik, M. and Saska, M. *New Era in Cultural Heritage Preservation: Cooperative Aerial Autonomy for Fast Digitalization of Difficult-to-Access Interiors of Historical Monuments.* IEEE Robotics and Automation Magazine, vol. 31, no. 2, pages 8–25, June 2024. [Online]. Available: http://dx.doi.org/10.1109/MRA.2023.3244423. (Cited in page 51.)

[Pieraccini 2001] Pieraccini, M., Luzi, G. and Atzeni, C. *Terrain mapping by ground-based interferometric radar.* IEEE Transactions on Geoscience and Remote Sensing, vol. 39, no. 10, pages 2176–2181, October 2001. [Online].

Available: https://ieeexplore.ieee.org/document/957280. (Cited in page 81.)

[Pourfard 2022] Pourfard, M., Hosseinian, T., Saeidi, R., Motamedi, S. A., Abdollahifard, M. J., Mansoori, R. and Safabakhsh, R. *KAZE-SAR: SAR Image Registration Using KAZE Detector and Modified SURF Descriptor for Tackling Speckle Noise.* IEEE Transactions on Geoscience and Remote Sensing, vol. 60, pages 1–12, 2022. [Online]. Available: https://ieeexplore.ieee.org/document/9460783/. (Cited in page 45.)

[RadarSimX 2019] RadarSimX. *RadarSimX: Radar Simulation Tools*, 2019. (Cited in page 100.)

[Rapp 2015] Rapp, M., Barjenbruch, M., Dietmayer, K., Hahn, M. and Dickmann, J. *A fast probabilistic ego-motion estimation framework for radar.* In 2015 European Conference on Mobile Robots (ECMR), pages 1–6, 2015. (Cited in page 27.)

[Reinecke 2024] Reinecke, M., Noegel, T., Heidbrink, M., Sura, O., Hoffmann, M., Gulden, P. and Vossiek, M. *A Method for the Accumulation of Forward-Looking SAR Images in Automotive Applications.* In 2024 21st European Radar Conference (EuRAD), pages 280–283, September 2024. (Cited in page 81.)

[Richards 2010a] Richards, M., Scheer, J. and Holm, W. Principles of modern radar. Number vol. 3 in Principles of Modern Radar. SciTech Pub., 2010. (Cited in page 92.)

[Richards 2010b] Richards, M. A. Digital signal processing fundamentals for radar, chapter Chapter 14, pages 495–546. IET, 2010. (Cited in pages v, 11, and 14.)

[Rizzi 2021] Rizzi, M., Tagliaferri, D., Tebaldini, S., Nicoli, M., Russo, I., Mazzucco, C., Monti-Guarnieri, A., Prati, C. and Spagnolini, U. *Navigation-Aided Automotive SAR Imaging in Urban Environments.* In 2021 IEEE International Geoscience and Remote Sensing Symposium IGARSS, pages 2979–2982, July 2021. ISSN: 2153-7003. (Cited in page 61.)

[Rizzi 2022] Rizzi, M., Manzoni, M., Tebaldini, S., Monti–Guarnieri, A. V., Prati, C. M., Tagliaferri, D., Nicoli, M., Russo, I., Mazzucco, C., Alfageme, S. T. and Spagnolini, U. *Multi-Beam Automotive SAR Imaging in Urban Scenarios.* In 2022 IEEE Radar Conference (RadarConf22), pages 01–06, March 2022. (Cited in page 62.)

[Rozas 1972] Rozas, P. and Cunningham, A. R. *Apollo experience report: Lunar module landing radar and rendezvous radar.* In NASA Technical Note (TN), 1972. (Cited in page 6.)

[Shah 2017] Shah, S., Dey, D., Lovett, C. and Kapoor, A. *AirSim: High-Fidelity Visual and Physical Simulation for Autonomous Vehicles.* 2017. [Online]. Available: `https://arxiv.org/abs/1705.05065`. (Cited in page 100.)

[Shan 2020] Shan, T., Englot, B., Meyers, D., Wang, W., Ratti, C. and Rus, D. *LIO-SAM: Tightly-coupled Lidar Inertial Odometry via Smoothing and Mapping.* In 2020 IEEE/RSJ International Conference on Intelligent Robots and Systems (IROS), pages 5135–5142, 2020. (Cited in page 2.)

[Shin 2023] Shin, S. and Kim, E. *Track-Before-Resolving: Doppler ambiguity resolution at low SNR.* IET Radar, Sonar and Navigation, vol. 17, no. 1, pages 117–127, January 2023. [Online]. Available: http://dx.doi.org/10.1049/rsn2.12328. Publisher Copyright: © 2022 The Authors. IET Radar, Sonar Navigation published by John Wiley Sons Ltd on behalf of The Institution of Engineering and Technology. (Cited in page 89.)

[Siegwart 2004] Siegwart, R. and Nourbakhsh, I. R. Introduction to Autonomous Mobile Robots. Bradford Company, USA, March 2004. (Cited in pages v and 2.)

[Soumekh 1999] Soumekh, M. *Synthetic Aperture Radar Signal Processing with MATLAB Algorithms.* 1999. (Cited in page 64.)

[Stanko 2016] Stanko, S., Palm, S., Sommer, R., Klöppel, F., Caris, M. and Pohl, N. *Millimeter resolution SAR imaging of infrastructure in the lower THz region using MIRANDA-300.* In 2016 European Radar Conference (EuRAD), pages 358–361, October 2016. (Cited in pages vii, 60, and 61.)

[Stauffer 1999] Stauffer, C. and Grimson, W. *Adaptive background mixture models for real-time tracking.* In Proceedings. 1999 IEEE Computer Society Conference on Computer Vision and Pattern Recognition (Cat. No PR00149), volume 2, pages 246–252 Vol. 2, 1999. (Cited in page 92.)

[Steiner 2020] Steiner, M., Grebner, T. and Waldschmidt, C. *Millimeter-Wave SAR-Imaging With Radar Networks Based on Radar Self-Localization.* IEEE Transactions on Microwave Theory and Techniques, vol. 68, no. 11, pages 4652–4661, November 2020. [Online]. Available: `https://ieeexplore.ieee.org/document/9115272`. Conference Name: IEEE Transactions on Microwave Theory and Techniques. (Cited in pages 28 and 61.)

[Tebaldini 2022] Tebaldini, S., Rizzi, M., Manzoni, M., Guarnieri, A. M., Prati, C., Tagliaferri, D., Nicoli, M., Spagnolini, U., Russo, I. and Mazzucco, C. *SAR imaging in automotive scenarios.* In 2022 Microwave Mediterranean Symposium (MMS), pages 1–5, May 2022. ISSN: 2157-9830. (Cited in pages 55 and 61.)

[Tebaldini 2023] Tebaldini, S., d'Alessandro, M. M., Ulander, L. M., Bennet, P., Gustavsson, A., Coccia, A., Macedo, K., Disney, M., Wilkes, P., Spors, H.-J., Schumacher, N., Hanuš, J., Novotný, J., Brede, B., Bartholomeus, H., Lau, A., van der Zee, J., Herold, M., Schuettemeyer, D. and Scipal, K. *TomoSense: A unique 3D dataset over temperate forest combining multi-frequency mono- and bi-static tomographic SAR with terrestrial, UAV and airborne lidar, and in-situ forest census.* Remote Sensing of Environment, vol. 290, page 113532, 2023. [Online]. Available: `https://www.sciencedirect.com/science/article/pii/S0034425723000834`. (Cited in page 80.)

[Tyack 2024] Tyack, T., Ferro-Famil, L. and Vivet, D. *Enhanced 3D Radar Target Detection and Tracking Using Extended Kalman Filtering for Ambiguity Resolution.* In 2024 International Radar Symposium (IRS), pages 341–346, 2024. (Cited in page 96.)

[Tyack 2025] Tyack, T., Vivet, D. and Ferro-Famil, L. *Implicit Extended Kalman Filter for Radar-Only 2D Odometry and Sensor-Vehicle Calibration.* In 2025 IEEE/SICE International Symposium on System Integration (SII), pages 1280–1285, 2025. (Cited in page 42.)

[Ubezio 2023] Ubezio, B., Zangl, H. and Hofbaur, M. *Extrinsic Calibration of a Multiple Radar System for Proximity Perception in Robotics.* In 2023 IEEE International Instrumentation and Measurement Technology Conference (I2MTC), pages 1–6, May 2023. ISSN: 2642-2077. (Cited in page 34.)

[Vivet 2013] Vivet, D., Checchin, P. and Chapuis, R. *Localization and Mapping Using Only a Rotating FMCW Radar Sensor.* Sensors, vol. 13, no. 4, pages 4527–4552, 2013. [Online]. Available: `https://www.mdpi.com/1424-8220/13/4/4527`. (Cited in page 26.)

[Vizzo 2023] Vizzo, I., Guadagnino, T., Mersch, B., Wiesmann, L., Behley, J. and Stachniss, C. *KISS-ICP: In Defense of Point-to-Point ICP – Simple, Accurate, and Robust Registration If Done the Right Way.* IEEE Robotics and Automation Letters, vol. 8, no. 2, pages 1029–1036, February 2023. [Online]. Available: `http://arxiv.org/abs/2209.15397`. arXiv:2209.15397 [cs]. (Cited in pages 2, 28, and 47.)

[von Arnim 2025] von Arnim, M., Vivet, D. and Watanabe, Y. *Context-adaptive GNSS/INS estimation strategies based on prior statistical multipath knowledge.* In 2025 IEEE/ION Position, Location and Navigation Symposium (PLANS), pages 821–830, April 2025. ISSN: 2153-3598. (Cited in page 2.)

[Wahl 1994] Wahl, D., Eichel, P., Ghiglia, D. and Jakowatz, C. *Phase gradient autofocus-a robust tool for high resolution SAR phase correction.* IEEE Transactions on Aerospace and Electronic Systems, vol. 30, no. 3, pages 827–835, July 1994. [Online]. Available: `https://ieeexplore.ieee.org/document/303752`. (Cited in page 60.)

[Waldschmidt 2025] Waldschmidt, C., Bonfert, C. and Grebner, T. Millimeter Wave Radar: Hardware and Signal Processing. Springer Nature, July 2025. Google-Books-ID: S1FyEQAAQBAJ. (Cited in page 61.)

[Wang 2025] Wang, J., Liu, Y., Deng, Q., Guo, S. and Mao, X. *High-resolution forward-looking MIMO-SAR imaging approach for automotive mmwave radar.* In Sixteenth International Conference on Graphics and Image Processing (ICGIP 2024), volume 13539, pages 592–598. SPIE, February 2025. (Cited in page 62.)

[Weiss 1982] Weiss, M. *Analysis of Some Modified Cell-Averaging CFAR Processors in Multiple-Target Situations.* IEEE Transactions on Aerospace and Electronic Systems, vol. AES-18, no. 1, pages 102–114, 1982. [Online]. Available: http://dx.doi.org/10.1109/TAES.1982.309210. (Cited in page 20.)

[Werber 2015] Werber, K., Rapp, M., Klappstein, J., Hahn, M., Dickmann, J., Dietmayer, K. and Waldschmidt, C. *Automotive radar gridmap representations.* In 2015 IEEE MTT-S International Conference on Microwaves for Intelligent Mobility (ICMIM), pages 1–4, 2015. (Cited in page 23.)

[Weston 2022] Weston, R., Gadd, M., De Martini, D., Newman, P. and Posner, I. *Fast-MbyM: Leveraging Translational Invariance of the Fourier Transform for Efficient and Accurate Radar Odometry.* March 2022. [Online]. Available: `http://arxiv.org/abs/2203.00459`. arXiv:2203.00459 [cs]. (Cited in page 26.)

[Wise 2023] Wise, E., Cheng, Q. and Kelly, J. *Spatiotemporal Calibration of 3-D Millimetre-Wavelength Radar-Camera Pairs.* IEEE Transactions on Robotics, vol. 39, no. 6, pages 4552–4566, 2023. [Online]. Available: http://dx.doi.org/10.1109/TRO.2023.3311680. (Cited in pages 34 and 49.)

[Wu 2009] Wu, H. and Zwick, T. *Automotive SAR for Parking Lot Detection.* In 2009 German Microwave Conference, pages 1–8, March 2009. ISSN: 2167-8030. (Cited in page 60.)

[Wu 2011] Wu, H., Zwirello, L., Li, X., Reichardt, L. and Zwick, T. *Motion compensation with one-axis gyroscope and two-axis accelerometer for automotive SAR.* In 2011 German Microwave Conference, pages 1–4, March 2011. ISSN: 2167-8022. (Cited in page 60.)

[Xi 1999] Xi, L., Guosui, L. and Ni, J. *Autofocusing of ISAR images based on entropy minimization.* IEEE Transactions on Aerospace and Electronic Systems, vol. 35, no. 4, pages 1240–1252, October 1999. [Online]. Available: `https://ieeexplore.ieee.org/document/805442`. (Cited in page 63.)

[Yin 2020] Yin, H., Wang, Y., Tang, L. and Xiong, R. *Radar-on-Lidar: metric radar localization on prior lidar maps.* In 2020 IEEE International Confer-

ence on Real-time Computing and Robotics (RCAR), pages 1–7, September 2020. (Cited in pages 82 and 101.)

[Yuan 2023a] Yuan, C., Lin, J., Zou, Z., Hong, X. and Zhang, F. *STD: Stable Triangle Descriptor for 3D place recognition.* 2023. [Online]. Available: `https://arxiv.org/abs/2209.12435`. (Cited in page 50.)

[Yuan 2023b] Yuan, S., Zhu, S., Fioranelli, F. and Yarovoy, A. G. *3-D Ego-Motion Estimation Using Multi-Channel FMCW Radar.* IEEE Transactions on Radar Systems, vol. 1, pages 368–381, 2023. [Online]. Available: `https://ieeexplore.ieee.org/document/10194956/`. (Cited in page 28.)

[Zhang 2024] Zhang, J., Zhuge, H., Wu, Z., Peng, G., Wen, M., Liu, Y. and Wang, D. *4DRadarSLAM: A 4D Imaging Radar SLAM System for Large-scale Environments based on Pose Graph Optimization.* In 2023 IEEE International Conference on Robotics and Automation (ICRA), 2024. (Cited in pages vi, 27, 28, and 54.)

[Zhou 2007] Zhou, H., Wen, B., Ma, Z. and Wu, S. *Range/Doppler ambiguity elimination in high-frequency chirp radars.* Radar, Sonar and Navigation, IEE Proceedings -, vol. 153, pages 467 – 472, 01 2007. [Online]. Available: http://dx.doi.org/10.1049/ip-rsn:20050115. (Cited in page 89.)

[Zhou 2022] Zhou, Y., Liu, L., Zhao, H., López-Benítez, M., Yu, L. and Yue, Y. *Towards Deep Radar Perception for Autonomous Driving: Datasets, Methods, and Challenges.* Sensors, vol. 22, no. 11, 2022. [Online]. Available: http://dx.doi.org/10.3390/s22114208. (Cited in page 2.)

[Zhuang 2023] Zhuang, Y., Wang, B., Huai, J. and Li, M. *4D iRIOM: 4D Imaging Radar Inertial Odometry and Mapping.* IEEE Robotics and Automation Letters, vol. 8, no. 6, pages 3246–3253, 2023. [Online]. Available: http://dx.doi.org/10.1109/LRA.2023.3266669. (Cited in pages 28 and 101.)

Abstract: Autonomous Mobile Robots tend to be used in increasingly diverse scenarios requiring a robust and precise localisation and accurate modelling of its environment. To address these aspects, it is important to rely on several different sensors. The most traditional ones, such as Global Navigation Satellite System (GNSS) receivers, Inertial Measurement Unit (IMU), LiDAR or cameras, are commonly used individually or combined to overcome their respective weaknesses. Nevertheless, GNSS can be affected by challenging navigation contexts involving an important number of non-line of sight satellites. Also, both cameras and LiDARs are impacted by harsh weather conditions, such as heavy rain, snow or fog and smoke. To avoid such inconvenience the use of millimeter wave radar sensors is becoming increasingly significant. Indeed radar perception is almost insensitive to the aforementioned conditions. Moreover, this sensor admits one of the widest diversity of information since it can not only estimate objects' 3D position via range and angle measurement but also its relative radial velocity and reflectivity. For these reasons, radar-based odometry and mapping are more and more studied. The scope of the thesis is to study the contribution of coherent radar in exteroceptive sensors based navigation. In particular, SAR imaging mapping is of interest for enabling dense, high-resolution mapping.

To balance the computational load, we propose to use pre-processed point clouds for odometry. First, a calibration solution is presented since we use a multi-radar setup with front- and side-looking sensors. Beforehand, an optimal sensor placement study has been done taking into account both calibrability and localisability. After that, several localisation approaches have been presented relying on Doppler-Angle velocimetry, range-azimuth map matching, radar pointcloud Iterative Closest Point (ICP). The latter has been chosen as the localisation solution due to its accuracy and low computational cost. Then, we introduced the SAR imagery, detailed the stakes and geometry involved. We have presented all the recorded data experiments of SAR-based mapping using 24GHz- and 77GHz-sensors following straight and non-linear trajectories using ground-truth positioning or our localisation solution. We proposed a lidar-based amplitude grid mapping product used as a ground-truth to put into perspective qualitatively our SAR imagery. Finally, we proposed a multi-object radar tracker in the context of measurement ambiguities.

Keywords: Mobile Robotics, Radar, Navigation, Mapping, Odometry, Synthetic Aperture Radar

Résumé : Les robots mobiles autonomes (AMR) sont de plus en plus utilisés dans des contextes variés qui exigent une localisation robuste et précise ainsi qu'une modélisation fidèle de leur environnement. Pour répondre à ces exigences, il est important de s'appuyer sur plusieurs capteurs différents. Les plus courants, tels que les récepteurs du Système de positionnement par satellites (GNSS), les unités de mesure inertielle (IMU), les LiDAR ou les caméras, sont généralement utilisés individuellement ou combinés afin de pallier leurs faiblesses respectives. Néanmoins, le GNSS peut être affecté par des contextes de navigation difficiles impliquant un nombre important de satellites hors de la ligne de visée. De plus, les caméras et les LiDAR sont tous deux affectés par des conditions météorologiques difficiles, telles que la pluie, la neige, le brouillard ou la fumée. Pour éviter ces inconvénients, l'utilisation de capteurs radar à ondes millimétriques prend de plus en plus d'importance. En effet, la perception radar est pratiquement insensible aux conditions susmentionnées. De plus, ce capteur offre l'une des plus grandes diversités d'informations, car il permet non seulement d'estimer la position 3D des objets via la mesure de la distance et de l'angle, mais aussi leur vitesse radiale relative et leur réflectivité. Pour ces raisons, l'odométrie et la cartographie basées radar font l'objet d'études de plus en plus nombreuses. L'objectif de cette thèse est d'étudier la contribution du radar cohérent à la navigation basée sur des capteurs extéroceptifs. En particulier, la cartographie par imagerie SAR présente un intérêt pour permettre une cartographie dense et à haute résolution.

Afin d'équilibrer la charge de calcul, nous proposons d'utiliser des nuages de points prétraités pour l'odométrie. Tout d'abord, nous présentons une solution de calibration, car nous utilisons une configuration multi-radars comprenant des capteurs orientés vers l'avant et sur le côté. Au préalable, une étude sur le placement optimal des capteurs a été menée en tenant compte à la fois de la calibrabilité et de la localisabilité. Ensuite, plusieurs approches de localisation ont été présentées, s'appuyant sur la vélocimétrie par régression Doppler-Angle, la correspondance de cartes de distance-azimut et l'algorithme ICP (Iterative Closest Point) pour les nuages de points radar. Cette dernière approche a été choisie comme solution de localisation en raison de sa précision et de son faible coût de calcul. Nous avons ensuite présenté l'imagerie SAR, en détaillant les enjeux et la géométrie impliqués. Nous avons présenté toutes les expériences de données enregistrées de cartographie par SAR utilisant des capteurs de 24 GHz et 77 GHz suivant des trajectoires droites et non linéaires, en utilisant soit une vérité-terrain de positionnement, soit notre solution de localisation. Afin de mettre en perspective qualitativement nos images SAR, nous avons proposé un produit de cartographie par grille d'amplitude basé sur données lidar, utilisé comme vérité terrain. Enfin, nous avons proposé un système de suivi radar multi-objets dans le contexte des ambiguïtés de mesure.

Mots clés : Robotique Mobile, Radar, Navigation, Cartographie, Odometrie, Radar à Synthèse d'Ouverture